POLITECNICO DI MILANO

SCHOOL OF INDUSTRIAL AND INFORMATION ENGINEERING

DEPARTMENT OF AEROSPACE SCIENCE AND TECHNOLOGY

MASTER OF SCIENCE IN SPACE ENGINEERING

Coupled Dynamics around Irregularly-Shaped Bodies with Enhanced Gravity Field Modelling

Advisor:
Prof. Michèle Lavagna

Co-Advisors:
Prof. Kathleen C. Howell
Prof. Lorenzo Casalino

Graduation Thesis of:
Andrea Colagrossi
796514

ACADEMIC YEAR 2013-2014

"Earth is the cradle of humanity,
but one cannot live in a cradle forever."

— Konstantin E. Tsiolkovsky

Abstract

One of the most important aspects when dealing with the dynamics close to an irregularly-shaped body is the accurate description of the force field in its surrounding. In particular, the determination of gravitational field and three-dimensional rotation motion is important to propagate accurately a trajectory in the vicinity of this kind of celestial bodies. This thesis discusses the analysis and the study of the dynamical environment around irregular small Solar System's objects, with particular attention to the representation of their gravitational influence and the characterization of their complex non-principal axis rotational dynamics. All the relevant perturbations are taken into account, including the third body gravitational effect, the Solar Radiation Pressure, the YORP effect and the internal dissipation of energy. Different characteristic shapes for typical celestial bodies are considered: from the simple, almost spherical, to shapes that are more complex. The irregularities in the geometry represent one of the most important sources of disturbances for what concern the dynamics of a particle in these surroundings, and therefore, the techniques to accurately model uneven gravitational fields are carefully analysed. The enhanced model must be valid up to the surface of the body and the fidelity of the results should be compatible with a reasonable computational effort. The perturbed evolution of the rotation state of these irregularly-shaped bodies is investigated, and the developed model is coupled with the equations of motion describing the orbital dynamics of a particle in their vicinity. All the relevant quantities are numerically evaluated exploiting the same input data, in order to maintain a uniform level of accuracy in the model. The simulations highlight some insightful features of the resulting dynamical environment, and despite they are applied on selected celestial objects, the presented approach applies to any irregular small Solar System's body.

Keywords: Irregularly-Shaped Celestial Body, Gravity Field Modelling, Rotational Dynamics, Coupled Dynamics, Perturbations, Trajectory Design.

Sommario

La dinamica attorno a un corpo celeste dalla forma irregolare può essere descritta attraverso una descrizione accurata del campo di forze nelle sue vicinanze. In particolare, la rappresentazione del campo gravitazionale e del moto rotatorio nelle tre dimensioni è importante per propagare accuratamente un'orbita intorno a questi oggetti del Sistema Solare. Con questa tesi si vuole analizzare l'evoluzione dinamica nello spazio circostante ai corpi celesti irregolari, dedicando un'attenzione particolare al modello dell'attrazione gravitazionale e alle caratteristiche della dinamica rotazionale attorno ad assi differenti da quelli principali d'inerzia. Sono state considerate tutte le perturbazioni di principale rilievo, come l'influenza gravitazionale esercitata da un terzo corpo, la pressione di radiazione solare, l'effetto YORP e la dissipazione di energia interna. Sono state utilizzate differenti geometrie caratteristiche di alcuni corpi celesti: dalla più semplice, quasi sferica, a quelle più complesse. Le irregolarità nella forma dell'attrattore principale generano i disturbi più importanti per la corrispondente dinamica orbitale; pertanto, le tecniche per rappresentare accuratamente i campi gravitazionali irregolari sono studiate attentamente. Il modello ottenuto deve essere valido fino alla superficie del corpo e la precisione dei risultati deve essere ottenuta con un ragionevole sforzo di calcolo. È stata studiata l'evoluzione dello stato di moto rotatorio, sotto l'effetto delle perturbazioni, per questi corpi dalla geometria irregolare, e inoltre, sono state sviluppate le equazioni del moto orbitale in prossimità degli stessi. La dinamica complessiva considera l'accoppiamento tra la meccanica orbitale e quella rotazionale. Tutte le quantità d'interesse sono state calcolate numericamente, usando gli stessi dati iniziali, per avere uniformità tra i risultati. Le simulazioni che sono state eseguite evidenziano delle caratteristiche interessanti per il problema considerato, e nonostante siano stati analizzati degli scenari specifici, questa ricerca si può applicare a qualsiasi corpo celeste irregolare.

Parole Chiave: Corpo Celeste dalla Geometria Irregolare, Modellazione del Campo Gravitazionale, Dinamica Rotazionale, Dinamica Accoppiata, Perturbazioni, Progettazione di Traiettorie.

Estratto in Lingua Italiana

I corpi celesti dalla forma irregolare sono sempre più studiati da parte della comunità scientifica. Questi oggetti sono estremamente numerosi e anche se determinano solamente una piccola frazione della massa orbitante attorno al Sole, il loro studio è fondamentale per capire la formazione e l'evoluzione del Sistema Solare, nonché l'origine degli oggetti celesti più massivi. Infatti, asteroidi e comete rappresentano i frammenti rimanenti del processo che ha formato i pianeti interni, compresa la Terra. Inoltre, le molecole a base di carbonio e i composti volatili, che sono stati fondamentali per la creazione della vita, potrebbero essere arrivati sulla Terra, durante le prime fasi evolutive del Sistema Solare, attraverso l'impatto di questi corpi celesti minori. Per di più, alcuni di questi piccoli corpi del sistema solare sono catalogati come *oggetti potenzialmente pericolosi*, il che significa che la loro orbita potrebbe fare incontri ravvicinati con la Terra, e gli stessi hanno una massa sufficientemente elevata da provocare una grave devastazione in caso di urto. Di conseguenza, essi devono essere analizzati attentamente per capire la loro composizione, struttura interna, dimensione e prevedere correttamente le loro traiettorie future. In questo modo si hanno le informazioni per elaborare una possibile strategia per proteggere la Terra dal rischio di un'eventuale collisione cosmica.

Per tutte queste ragioni, negli ultimi anni, alcuni piccoli oggetti celesti sono diventati l'obiettivo di diverse missioni spaziali. Questo perché le classiche osservazioni terrestri hanno delle potenzialità limitate e un'ottima comprensione di questi elementi è possibile solo attraverso accurate analisi, effettuate con una sonda spaziale nelle loro vicinanze. Tuttavia, la progettazione di una missione in prossimità di un asteroide o una cometa crea ancora molte difficoltà per gli esperti di dinamica del volo, a causa delle problematiche esistenti nel predire la traiettoria di un corpo in queste circostanze.

I modelli gravitazionali classici, che sono correntemente usati in meccanica orbitale, non sono sufficientemente accurati nel predire il moto di una particella attorno ad un corpo irregolare in moto rotatorio. In questi casi, le traiettorie sono molto differenti da quelle Kepleriane e la dinamica risultante è molto perturbata. Infatti, le perturbazioni principali che agiscono in questo contesto sono generate dalla forma irregolare dell'oggetto, dal suo complesso moto di rotazione, dalla radiazione solare e dall'attrazione gravitazionale del Sole. L'effetto combinato di questi aspetti caratterizza l'evoluzione orbitale in prossimità di un asteroide

o una cometa, la quale deve essere attentamente studiata durante la pianificazione della missione e le fasi precedenti il volo.

Il Progetto di Tesi

Questa ricerca ha un triplice obiettivo che può essere raggiunto sviluppando tre temi separati. Il primo riguarda un ampio studio delle diverse tecniche per rappresentare il campo gravitazionale di un oggetto dalla geometria irregolare. Il secondo include un'attenta descrizione della sua dinamica rotazionale, sotto l'effetto delle perturbazioni. Il terzo interessa una completa caratterizzazione delle traiettorie nello spazio vicino alla superficie del corpo irregolare.

Sono stati sviluppati diversi strumenti per condurre questa ricerca, e i risultati ottenuti sono serviti allo scopo di avere una visione globale di questo problema affascinante e attuale. Le conclusioni di questo studio dovrebbero facilitare la comprensione delle dinamiche complesse e non lineari di una particella in queste circostanze. In particolare, sono stati ampiamente studiati i differenti modelli gravitazionali per descrivere il campo di accelerazione generato da un corpo dalla forma arbitraria. La precisione del modello è essenziale, e i risultati devono essere validi fino alla superficie del corpo, senza limitazioni per le regioni in cui l'analisi può essere applicata correttamente. Questo è particolarmente importante per supportare alcune delle esigenze dell'attuale ricerca nel campo dell'ingegneria spaziale. Inoltre, l'esame della dinamica rotazionale di asteroidi e comete può anche essere considerata come una parte separata di questo lavoro. Poiché, questo aspetto non è solo utile per propagare precisamente il moto intorno a uno di questi corpi celesti, ma è utile anche per comprendere la naturale evoluzione del loro stato di moto rotatorio, e l'effetto delle perturbazioni sulla loro dinamica. Le conclusioni ottenute possono essere applicate per aiutare la comprensione di alcune delle attuali domande che le scienze planetarie si pongono.

Pertanto, lo scopo di questa tesi è quello di fornire utili strumenti di analisi per ottenere dei risultati interessanti, che possono essere utilizzati per progettare una missione spaziale attorno a questa tipologia di corpi celesti, o per comprendere le dinamiche naturali degli stessi.

Modelli per il Campo Gravitazionale

Il campo gravitazionale generato da un corpo dalla forma irregolare è stato modellato con due tecniche diverse, che derivano da una solida formulazione analitica, ma richiedono uno sviluppo numerico per essere praticamente implementate. Entrambe derivano da un principio semplice ma efficace: conoscendo il potenziale gravitazionale generato da un corpo geometricamente semplice, è possibile ottenere il potenziale di qualsiasi oggetto che può essere rappresentato da un insieme di questi componenti elementari. Vale a dire, ogni corpo continuo può essere discretizzato da queste unità fondamentali, che sono la massa puntiforme per l'approccio *mascons*, e il tetraedro con densità costante per la tecnica a *poliedro*.

Le due tecniche per modellare il potenziale e l'attrazione gravitazionale sono state ampiamente analizzate e confrontate. La finalità principale di questa sezione è quella di determinare il livello di accuratezza dei diversi metodi di modellazione. Per eseguire questa analisi sono state impiegate alcune geometrie di riferimento, reali e ideali. Il carico computazionale è sempre stato monitorato in modo da individuare un compromesso tra precisione e tempo di calcolo necessario per valutare le quantità desiderate. È stata anche sviluppata la versione ottimizzata dell'approccio mascons, e i risultati ottenuti sono stati confrontati in seguito con quelli relativi alla versione standard della stessa tecnica di modellazione.

Infine, le diverse tecniche sono state testate contemporaneamente sulle diverse forme di riferimento, al fine di trovare il modello che combina in maniera ottimale un buon livello di precisione con una velocità computazionale ragionevole.

Dinamica Rotazionale

La dinamica rotazionale di un corpo dalla forma irregolare è stata analizzata con molta cura. Le più importanti coppie di perturbazione sono state incluse nell'analisi, dopo un'accurata validazione degli algoritmi usati per calcolare il loro contributo, che include l'influenza gravitazionale esercitata da un terzo corpo, la pressione di radiazione solare, l'effetto YORP e la dissipazione di energia interna.

È stata eseguita e discussa anche un'analisi di sensitività per valutare la robustezza del modello alle incertezze nella descrizione delle proprietà fisiche e dinamiche del corpo. L'intento è quello di capire se un modello ad alta fedeltà può essere impiegato con profitto anche

nello studio di corpi che sono stati osservati e descritti solo in maniera preliminare. Questo può essere importante nelle fasi preliminari di progettazione di una missione spaziale, quando l'obiettivo finale non è stato ancora individuato definitivamente e la conoscenza dei dettagli è solo approssimativa.

Lo studio è stato arricchito con l'applicazione dell'algoritmo sviluppato in alcuni casi di particolare interesse scientifico. Le simulazioni ottenute sono state impiegate per evidenziare alcune caratteristiche interessanti di questo problema. Lo scopo principale è quello di trovare andamenti tipici per la naturale evoluzione dello stato di rotazione degli oggetti selezionati.

Dinamica Complessiva Accoppiata

In questo lavoro sono state studiate anche le dinamiche esistenti nello spazio attorno ad un corpo irregolare; analizzando come queste sono influenzate dalla forma e dallo stato di rotazione dell'attrattore principale. I risultati possono essere utilizzati per effettuare un'analisi dei moti possibili attorno a un asteroide o una cometa. A tal fine, è stato sviluppato un modello per simulare la dinamica complessiva e accoppiata di una particella attorno a un oggetto celeste irregolare in moto rotatorio e perturbato.

I risultati sono stati costantemente monitorati mediante l'uso di quantità fisiche di riferimento, e lo studio di alcune semplici condizioni iniziali è stato portato avanti per verificare ed esaminare l'esistenza dei punti di equilibrio e l'evoluzione delle superfici a velocità nulla (ZVS).

Il modello che include le perturbazioni è stato anche confrontato con un modello più semplice, il quale tiene conto solamente del moto rotatorio senza i disturbi esterni. In questo modo è stato possibile quantificare la validità dei modelli più semplici, utili per portare avanti delle analisi meno sofisticate, che possono essere utili per avere una veloce comprensione preliminare del problema.

Lo scopo finale di tutta la ricerca è quello di avere uno strumento di progettazione accurata che possa essere applicato per simulare i possibili scenari di missione intorno a questi affascinanti corpi del Sistema Solare.

Conclusioni

La rappresentazione di questi scenari deve essere effettuata con un equilibrio tra fedeltà dei risultati e tempo di calcolo necessario. Questo

problema non ha un'unica soluzione, e la decisione finale dipende dalla particolare applicazione. Per esempio, le fasi avanzate del progetto di missione sono notevolmente esigenti in termini di precisione, ma le operazioni in tempo reale, che devono essere gestite dal computer di bordo di una sonda spaziale, richiedono solamente degli algoritmi veloci e affidabili. Pertanto, in molti casi pratici, il modello che trova questo compromesso ottimale, per come è stato definito e impiegato in questo lavoro di ricerca, è estremamente utile. Gli algoritmi che sono stati sviluppati fanno largo uso di tecniche di calcolo parallelo. Tuttavia, il codice può essere ottimizzato ulteriormente, e infatti un grande aiuto per la velocità computazionale arriva sfruttando un codice scritto in maniera più semplice e leggera rispetto a Matlab; C e Fortran potrebbero essere delle valide soluzioni.

Le tecniche di modellazione che sono state utilizzate per descrivere il campo gravitazionale di un oggetto celeste irregolare hanno ovviamente dei vantaggi e degli svantaggi. Permettono di avere una buona rappresentazione del campo gravitazionale in tutto le regioni d'interesse, compresa la superficie del corpo, non avendo problemi di convergenza. Il livello di precisione ottenibile può essere facilmente regolato variando il numero di elementi nella rappresentazione della forma, e di conseguenza, sono estremamente flessibili. Tuttavia, richiedono uno sforzo di calcolo maggiore rispetto ad altri metodi.

Il moto rotatorio è estremamente influenzato dalla presenza delle perturbazioni. L'effetto delle stesse è differente per ogni singolo caso, ma, in generale, le perturbazioni dovute alla radiazione solare e l'influenza gravitazionale del Sole sono i disturbi più rilevanti. L'effetto secolare delle perturbazioni è abbastanza limitato, e le variazioni non periodiche evolvono su una lunghissima scala temporale. Invece, le oscillazioni periodiche del moto sono collegate con le dinamiche orbitali in prossimità di questi corpi celesti, e il loro studio contribuisce ad aumentare l'accuratezza del modello dinamico complessivo.

Le caratteristiche di queste dinamiche accoppiate sono subordinate allo stato di moto rotatorio dell'attrattore principale. Un integrale del moto esiste solo se la rotazione è uniforme attorno a un asse principale d'inerzia; in questo caso le equazioni del moto sono tempo-invarianti, nel sistema di riferimento rotante. La stabilità del moto deve essere verificata per ciascun insieme di condizioni iniziali, anche se, in generale, le orbite retrograde e le orbite risonanti sono particolarmente stabili. Le traiettorie ottenute sono fortemente influenzate dallo stato di rotazione del primario, e di conseguenza, l'incertezza nella determinazione dell'asse di rotazione deve essere la più piccola possibile.

Questo settore di ricerca è molto attivo, e la comunità scientifica è desiderosa di accrescere la comprensione di questi argomenti. Grazie ai recenti progressi nel campo dell'ingegneria spaziale, le missioni interplanetarie attuali stanno svolgendo compiti incredibili e coinvolgenti. Tuttavia, le missioni di domani saranno ancora più impegnative e complesse. Questo non deve essere visto come un limite, dato che l'essere umano non può rimanere confinato nella sua zona di comfort, ma deve continuamente sfidare se stesso, esplorando e scoprendo nuovi mondi, i quali includono anche asteroidi, comete, pianeti del Sistema Solare e molto altro.

Acknowledgments

Outside it is still cold, despite the spring has already begun, and I am nearly finished checking my thesis now. Therefore, it is time to take a break, collect my feelings and acknowledge those people who are always in my mind and continuously support and motivate me.

First, I desire to express my endless gratitude to my family, especially to my parents, Pierangelo and Maria Elena, and to my sister, Valentina; you always believed in me, supported all my choices, make me feel loved and valued. I am so lucky to have you all, and even if sometimes my temper is harsh, I hope you can feel my love and appreciation to you. Thank you for the questions about my work, for the continuous motivation, for the moral support and for the inspiration that you gave me. I am still following my dream and everything was only possible because of you.

I also wish to dedicate a special thought to all my grandparents: *questa è anche per voi, Nonni.*

I would like to declare my gratitude to the best group of persons in the World: my friends. It is difficult to find the right words to reveal my feelings, but I can clearly say that it is hard to think my life without you, and for this reason, thanks to you all.

In particular, I want to thank Flavia; you were my support across the ocean and you will have your "pat-pat" as soon as I will be back in town. There, I will find also those persons who shared with me the best moments of my life and who will be always in my heart. Thank you *Groove Street*, and thank you very much *Sette Capocce.*

I would love to thank the wonderful friends were always with me during the exciting years of university, both in Turin and in Milan. Thank you Francesco, *Tavolo Pesante* and *Tre dell'Ave Maria*. I will always keep the last few years in my memories and in my heart, thanks to you.

I owe special thanks to my awesome American friends: Ben, Boomer, Dana, Emily, Jordan, Kelsie, Ryan, Tori, Zak and all the other great guys I met in this country. I hope that I can see you again in Italy, or in the U.S.

I am eager to thank Davide, Fabio, Loïc and the entire research group at Purdue University for the extremely valuable support throughout my first research work. I knock on wood, it will not be the last.

I am immensely grateful to Professor Michèle Lavagna for the opportunity she offered me, together with the trust she makes me feel. She was an extraordinarily powerful source of motivation for me, and I am very

thankful for all the support she gave me during my academic growth. I hope to be able to return her trust.

I also would like to thank Professor Kathleen C. Howell, she allowed me to join her research group and she welcomed me in this experience, providing me an incredibly stimulating environment to carry out my research.

Special thanks to Professor Lorenzo Casalino for the support he gave me in the development of my bachelor's thesis. With him I discovered my passion for spaceflight dynamics and I am greatly honoured he accepted to be my co-advisor for the double degree in Turin.

In this regard, I must thank Alta Scuola Politecnica, Politecnico di Milano and Politecnico di Torino for providing funding opportunities and support all over my academic path.

These last few months have been among the best of my life. The American experience taught me a lot; there have been ups and downs, but I enjoyed every single moments of this adventure, which changed my life. I already acknowledged all the persons who made this possible, but I want to dedicate a last thought to a special one. Together we enjoyed a relevant part of our life, we had amazing experiences and we shared every little thing. Then, life goes on and everyone makes his own decisions. I do not know what the future has in store for both of us; I will do always my best and I am sure you too. In the meanwhile, thank you for just being the wonderful person that you are.

Andrea

West Lafayette, Indiana
March 29th, 2015

Contents

List of Figures

List of Tables

Chapter 1

Introduction

Celestial bodies with irregular shapes are exposed to increasing interest in the scientific community. They are extremely numerous in the Solar System, and even if they comprise a tiny fraction of the mass orbiting around the Sun, their study is fundamental to understand the formation and the evolution of the Solar System, as well as the origin of the more massive celestial objects. In fact, *asteroids* and *comets* represent fragments and tiny pieces left over from the process that formed the inner planets, including Earth. Moreover, carbon-based molecules and volatile materials, which were fundamental to establish life, may have been carried to Earth during the early life of the Solar System, through the impacts of these minor celestial bodies.

In addition, some of these small Solar System's bodies are catalogued as *potentially hazardous objects* (PHO), meaning that their orbit could make close approaches to the Earth and they are massive enough to provoke a serious devastation in the event of impact. Consequently, they have to be carefully analysed to understand their composition, structure, size and future trajectories, in order to be able to devise an intelligent strategy to protect the Earth from the risk of an eventual cosmic collision.

For all these reasons, in recent years, small irregular celestial objects have become the target of current and forthcoming space missions. Indeed, the classic ground-based observations have restricted capacities and an excellent comprehension of these bodies is only possible by means of close observations conducted with a space probe in their vicinity. However, the design of a mission in close proximity of an asteroid or a comet is still challenging for the flight dynamicists, because of the existing difficulties in predicting the trajectory of a spacecraft in these dynamical environments.

Classic gravity models used in orbital mechanics are not accurate enough to predict the motion of a particle around a rotating irregular body. There, existing trajectories are remarkably non-Keplerian and the dynamics of a spacecraft is affected by different perturbing components. In fact, the primary perturbations acting in these circumstances are due to the uneven shape of the object, its complex rotational motion, the solar radiation and the gravitational influence of the Sun. The combined effect of these aspects characterizes the orbital evolution about an asteroid or a comet, and they must be carefully studied during pre-flight navigation and mission planning.

1.1 Problem Definition

In this research work, the threefold focus is to extensively study the different enhanced techniques to model the gravitational field of an irregularly-shaped object; describe its perturbed rotational dynamics, and characterize the dynamical environment close to its surface. Several tools are developed and different analyses are carried out with the goal to have a global and comprehensive perspective of this intriguing and ongoing problem.

The outcomes of this study are supposed to allow a further step towards the understanding of the dynamics of a particle in these complicated and nonlinear environments. In particular, different gravity models to describe the irregular acceleration field generated by an arbitrarily-shaped body are widely studied. The accuracy of the result is essential and the model must be valid up to the surface of the body, without limitations on the regions where the analysis can be correctly applied. This is particularly appealing to support part of the present space engineering needs.

Moreover, the investigation of the rotational motion of asteroids and comets can be also considered as a separate part of the research. In fact, this aspect is not only important to accurately propagate the motion around a rotating irregular object, but it is also useful to understand the natural evolution of the rotation state of these minor celestial bodies, and the effect of the perturbations on their dynamics. The obtained conclusions might be applied to help the solutions of some current planetary science questions.

Therefore, the purpose of this thesis it to provide helpful analysis tools and insightful results that can be used to design a space mission around an irregularly-shaped body, or to comprehend and propagate the

natural dynamics of these celestial objects. In particular, the objectives of this work are:

- Study and compare the different techniques to model the gravitational potential and attraction generated by an irregular body. The main goal of this part is to determine the level of accuracy of different enhanced modelling approaches, considering that also the region in the proximity of the surface must be included in the computational domain. The present analysis uses some reference shapes, real and ideal, to perform this task. The computational burden is always monitored in order to be able to find a trade-off between precision and required time to evaluate the desired quantities.

- Develop the optimized version of one of the most common techniques to compute the gravitational attraction of a body with an arbitrary shape. The obtained results are then compared with those related to the standard version of the same modelling approach. The objective of this work is to increase the efficiency of this method, which is very attractive in term of necessary computational speed.

- Investigate the rotational dynamics of an irregularly-shaped body. Different perturbing torques are included in the analysis after an accurate validation of the algorithms to evaluate their contributions. The aim is to find typical trends in the natural evolution of the rotation state of selected objects. The robustness of the model is assessed through a sensitivity analysis of the inevitable uncertainties in the available data.

- Analyse the dynamical environment around an irregular body, as it is characterized by the shape and the rotation state of the main attractor. The outcomes can be used to perform a preliminary estimation of the possible dynamics around an asteroid or a comet.

- Implement the model to simulate the coupled dynamics of a particle around a rotating and perturbed irregular celestial object. The ultimate scope is to have an accurate design tool that can be applied to simulate possible mission scenarios around these fascinating Solar System's bodies.

1.2 Historical Overview

Modern work on gravitational theories began with Galileo Galilei at the end of the 16th century. In 1609, the German mathematician and astronomer Johannes Kepler postulated that the motion of celestial bodies evolves on conic orbits, as described in his laws of planetary motion. However, the observations of Kepler were mathematically confirmed only in 1687, when the English scientist Sir Isaac Newton published the *Principia Mathematica* [35]. In this work, it is contained the first mathematical model describing the interaction between two massive objects in space.

After the formulation of Newton's theory of gravitation, the scientific community was interested in finding the complete description of motion under the influence of more than two bodies. Nevertheless, if more complex problems are considered, the general analytical description of the motion is not available anymore.

Particular equilibrium solutions in the Three-Body problem were found at the end of the 18th century by the Italian mathematician Giuseppe Lodovico Lagrangia and the Swiss physicist Leonhard Euler. The former proved the existence of constrained analytical equilibrium solutions in the general three-body Problem, while the latter introduced for the first time the idea of a synodic, or rotating, coordinate frame to formulate the Restricted Three Body problem.

In the following years, several mathematicians, physicists and astronomers continued to develop analytical theories to study problems of increasing complexity. Different techniques were developed to analyse some peculiarities of the motion in an arbitrarily complicated gravitational field, but a global analytical solution was never found.

In recent years, the advent of numerical computing techniques determined a great improvement in the investigation of almost any dynamical system. As a consequence, also the study of the behaviour of an object in the vicinity of an irregularly-shaped body is now possible. The description of this complex dynamical environment has many similarities with the characterization of a n-body problem, because a generic irregular body can be always visualized as an ensemble of individual point masses. Hence, the tools and the ideas developed in the study of the n-body problems, such as the existence of equilibrium solutions, Zero Velocity Surfaces and Poincarè maps, are useful also to analyse problems involving an asteroid or a comet.

The complete investigation of the dynamics in the vicinity of an arbitrarily-shaped celestial body requires models for the gravitational

potential function associated with such a shape. Different techniques emerged in the 1900's with the remarkable development of the observation technologies, able to provide more accurate shape determinations of real Solar System's objects.

These modelling approaches are now available and they are supported by the increasing availability of computational resources. As a matter of fact, real space missions to irregular bodies are becoming more common, and the necessity to improve the knowledge of these complex dynamical environments is still present.

1.3 Present Work

This thesis deals with the analysis of the orbital motion of a particle around an irregularly-shaped body, coupled with the perturbed rotational dynamics of the primary attractor. The resulting dynamical environment is extremely complex and the complete investigation can be carried out only exploiting modern numerical methods.

The gravitational field of the irregular body is modelled with two different techniques, which emerge from a solid analytical formulation, but they require a numerical development to be practically implemented. The coupled dynamical model of the orbital dynamics around the rotating irregular body is derived in a primary-fixed reference frame to facilitate the numerical investigation. The complete dynamics is described by a system of first order scalar differential equations, which are then numerically integrated.

The model is implemented maintaining a high fidelity of the results, as requested to accurately propagate the dynamical state of an irregular celestial body or to design a real space mission. Therefore, the general validity of the study is reduced and all the conclusions refer to the particular selected environment. However, in order to mitigate this issue, the presented simulations are tuned to highlight some insightful global features of the dynamics of a particle in the vicinity of an arbitrarily-shaped body.

After this introductory chapter, the outline of the thesis continues presenting the necessary general background to understand the concepts that are described in this work. So, in *chapter 2*, the gravity models are presented together with their theoretical formulation. Then, the coupled dynamical model is defined and some useful features of the problem are presented. In addition, the reference celestial bodies that are employed in this research work are introduced in this chapter. Finally,

the perturbative effects that influence the rotational dynamics of the main attractor are illustrated.

Chapter 3 is focused on the enhanced gravity field models, computed for all the reference celestial objects. Moreover, the comparison between the different modelling techniques is entirely presented in this section, together with the development of the optimized version of one of the available methods. In the last part of the chapter, all the distinct techniques are accurately tested on the reference shapes, in order to find the model that combines a decent level of accuracy with a reasonable computational speed.

Chapter 4 deals with the rotational dynamics of irregularly-shaped bodies. The implementation of the model is described and the validation of the algorithm is presented. Then, a sensitivity analysis is shown and discussed evaluating the robustness of the model to the uncertainties in the description of the physical and dynamical properties of the body. The study is concluded with the application of the developed algorithm to particular environments. The obtained simulations are illustrated and exploited to highlight some interesting characteristics of this problem.

Chapter 5 analyses the dynamical environment in the vicinity of the selected reference celestial objects. First of all, the implementation of the whole coupled dynamical model is described. Then, an extended discussion about some particular solutions is carried out, with the purpose to delineate the features of the dynamical environments in the surroundings of these celestial bodies. Finally, the complete model is applied to the selected environments, and the practical effect of the perturbations on the dynamics of the particle is quantified.

The thesis comes to an end with a *conclusions* chapter, where all the obtained results are summarized along with recommendations for future research works.

Chapter 2

Background

In this chapter, the background knowledge needed to approach the present research work is recalled. The dynamical environment existing in the vicinity of an irregularly-shaped celestial body is considered, and in particular, the different techniques used to represent the generated gravitational field are described.

The equations of motion and the dynamics connected to this particular context are here presented and discussed. Moreover, some important particular solutions are then shown to characterize the generic results that can be obtained dealing with this topic.

Finally, some perturbative effects that could influence the overall dynamical environment are defined.

2.1 Gravitational Field

The gravitational field represents the influence that a massive body extends into the surrounding space, producing a force on another massive particle. The work done by this force upon the particle, which is in motion between two points, is the same for any physically possible path between these two points, thus the gravitational field is said to be *conservative*.

From vector analysis, a necessary and sufficient condition that this work be independent from the physical path taken by the particle is that the force per unit mass, $\mathbf{f}$, be the gradient of a scalar function of position:

$$\mathbf{f} = \nabla U(\mathbf{p}), \tag{2.1}$$

where U is called the *gravitational potential* [17]. ∇ represents the three-dimensional gradient operator whose Cartesian form is $\hat{\mathbf{i}}\frac{\partial}{\partial x} + \hat{\mathbf{j}}\frac{\partial}{\partial y} + \hat{\mathbf{k}}\frac{\partial}{\partial z}$.

The Newton's law is the generally used gravitational model to describe the force field due to arbitrarily shaped bodies. It states that any pair of particles attracts each other with a force that is directly proportional to the product of their masses and inversely proportional to the square of the distance between them. So, according to this law, the gravitational potential due to a point mass m is:

$$U = G\frac{m}{r}, \tag{2.2}$$

where G is the gravitational constant and r is the distance of the test particle from the mass m.

The gravitational potential in free space satisfies Laplace's equation:

$$\nabla^2 U = 0, \tag{2.3}$$

where $\nabla^2 = \frac{\partial^2}{\partial x^2} + \frac{\partial^2}{\partial y^2} + \frac{\partial^2}{\partial z^2}$ is the Laplace's operator with its Cartesian form. Laplace's equation can be easily proved [50]: Gauss's theorem of divergence states that the integral of the divergence of a vector field over a region of space is equivalent to the integral of the outward normal component of the field over the surface enclosing that region. In any free space volume there is no attracting matter, hence the Gauss's theorem is identically null and the divergence of the field is equal to zero, $\nabla \cdot \mathbf{f} = 0$. Using equation (2.1) and remembering the definition of the Laplace's operator, $\nabla^2 = \nabla \cdot \nabla$, equation (2.3) is verified.

It is important to stress the fact that Newton's law is valid for any massive body, even though it is easier to be applied if the bodies can be reduced to point masses. In common orbital mechanics applications, this assumption is generally true, since spacecraft size and mass are usually noticeably smaller than those of the other bodies in the model, and therefore the point mass assumption can be easily justified. Moreover, to a first approximation, the mass distribution of larger celestial bodies is usually spherically symmetric, and thus, they exert the same gravitational attraction as if all their mass were concentrated at a point at their centre [35]. For these reasons, they can be defined as *centrobaric* bodies.

According to what has been said, the dynamics of an ordinary spacecraft and planet system is reasonably described exploiting the classical Newton's model, which also allows an analytical expression for the gravity potential, equation (2.2). Nevertheless, in the Solar System, there are plenty of bodies that cannot be defined as centrobaric and in this work they are the focus of the analysis. In fact, when the dynamical system involves one of these bodies, the point mass assumption is no

longer valid and the Newton's law must be extended in order to include non-spherical shapes as well. In principle this operation is straightforward: any arbitrary body can be considered as a collection of differential mass elements, and for that reason, the net force on an external point mass is obtained integrating the inverse square law between any pair of particles over the mass distribution representing the body.

In the same way, the gravitational potential could theoretically be evaluated with an integral over the body mass:

$$U = G \iiint_{body} \frac{1}{r}\, dm. \tag{2.4}$$

However, this operation is not practical for applications: the real mass distribution within the body is often not well known, poorly modelled, or too complex to evaluate correctly equation (2.4). Therefore, other gravitational modelling techniques are needed.

2.2 Gravity Models for Irregularly-Shaped Bodies

Gravity models for irregularly-shaped bodies were developed in the past to increase the model accuracy around the main bodies of the Solar System, because none of the actual celestial bodies is exactly spherical, and some of them can be defined at most as quasi-spherical. So, the classical manner of representing arbitrary gravitational fields is by expanding the gravitational potential into a *harmonic series*, represented in a system of spherical coordinates. This technique perturbs the potential of a sphere with an infinite sequence of terms converging to the correct gravity field.

As will be clarified in the following, harmonic expansions have several drawbacks when dealing with irregularly-shaped bodies, especially when their shape departs substantially from the sphere. In these situations two other techniques are available and they both arise from a simple but effective principle: knowing the gravity potential generated by a simply-shaped elemental body it is possible to know the potential of any body that can be represented by an ensemble of these smaller components. Namely, these elementary units are the point mass for the mass concentration, *mascons*, approach and the constant-density polyhedron for the *polyhedral* approach.

In all these cases, exact analytical gravity information for a single whole body are not available and all these modelling techniques rely on some assumptions. Furthermore, they usually generate an approximation of the actual gravity field, and their accuracy depends on the particular application, as will be discussed afterwards. In this work, the gravitational models are developed for irregularly-shaped Solar System's smaller bodies, such as comets and asteroids.

2.2.1 Harmonic Series Expansion Approach

The harmonic expansion approach allows the evaluation of an arbitrary gravitational field exploiting a specific set of spherical harmonics that forms an orthogonal system, first introduced by Pierre Simon de Laplace [23]. This is possible because the gravitational potential is a harmonic function, being a solution of equation (2.3), and it can be expressed as:

$$U(r,\theta,\lambda) = \frac{Gm}{r}\left[1 + \sum_{n=2}^{\infty}\sum_{m=0}^{n}\left(\frac{R_e}{r}\right)^n P_{nm}\sin\theta\left(C_{nm}\cos m\lambda + S_{nm}\sin m\lambda\right)\right], \quad (2.5)$$

where r, θ and λ are, respectively, the distance, latitude and longitude in a coordinate system whose origin is at the centre of mass of the body. R_e is the largest equatorial radius of the body, P_{nm} are the associate Legendre's polynomials, and C_{nm} and S_{nm} are the coefficients of the potential determined by the mass distribution within the body. These coefficients can be obtained as integrals over the volume of the body, or alternatively and practically, they can be estimated from radio tracking data of space probes during a fly-by of the body.

The harmonic series expansion is guaranteed to converge to the correct gravity field outside of a circumscribing sphere, and as a series, it can be truncated at any finite order according to the needed accuracy. Moreover, the computational resources to evaluate the series to an acceptable order are not large and the computational time is short enough.

Nevertheless, particularly when dealing with irregularly-shaped bodies, the spherical harmonics approach has several drawbacks. First, the field is always an approximation of the exact one due to the finite truncation of the series expansion. In addition, the series is no longer guaranteed to converge inside the circumscribing sphere, and actually often diverges. Hence, this method is not applicable for analysis of particle dynamics close to the surface, unless burdensome procedures that recompute the series at each radius of the body are applied. Obviously,

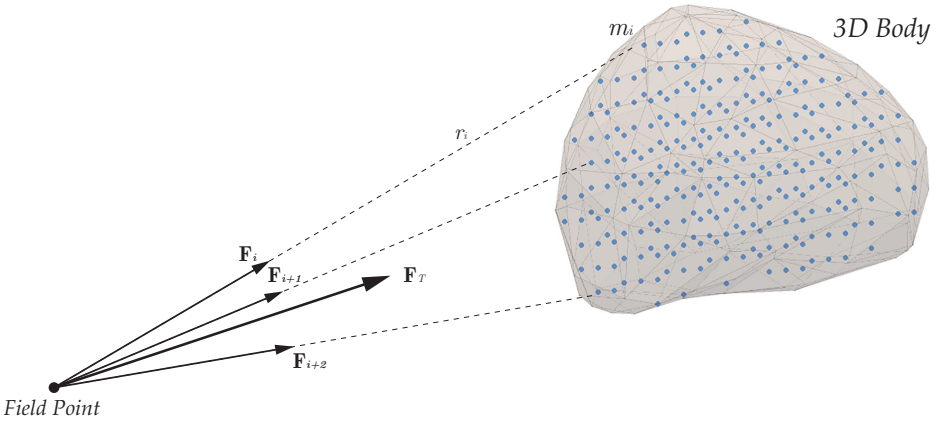

Figure 2.1: Mascons Approach.

this disadvantage is not relevant in planetary applications, but it is bothersome when dealing with irregular bodies whose shape is completely different from a sphere. Furthermore, this technique does not return any information about whether a field point is outside or inside the body.

Anyway, this gravitational modelling approach is not employed in this research work that deals with irregularly-shaped bodies without limitations in the area close to the surface.

2.2.2 Mascons Approach

The mascons, mass concentrations, approach is surprisingly simple from a conceptual point of view because it uses several point masses to reproduce the body's mass distribution, as in figure 2.1. Originally, it has been developed to compute the gravity field of bodies with a remarkably irregular shape. The results that can be obtained are influenced by the number of the employed masses, and by the way in which they are distributed inside the body. The mass of the total body is always preserved and usually the volume is filled with point masses on an evenly spaced grid, which will be referred to as *gridded mascons approach* in this thesis.

This method is very simple to develop and the final result can be easily obtained with a sum of all the contributions due to each point mass. This technique does not diverge and converge to the true gravitational field if an arbitrarily large number of masses is selected.

Remembering the equation (2.2), the gravitational potential of the whole body, making use of N_m mascons, is:

$$U = G \sum_{i=1}^{N_m} \frac{m_i}{r_i}, \tag{2.6}$$

where m_i and r_i are, respectively, the mass value and the distance from each point mass. The computational resources that are needed to obtain acceptable results are moderate and the computing time is still tolerable.

Nevertheless, this method has various flaws that overshadow its simplicity. First, for a given computational effort, the mascons approach is less accurate than a harmonic series expansion; in particular, this method produce significant errors in the force computation, as will be discussed. Moreover, also the mascons approach is not able to determine if a field point is inside or outside the body.

If two point masses are employed, $N_m = 2$, the dynamics of a particle around the irregular object is governed by the rules of the circular restricted three-body problem, whose characteristics are well known.

Obviously, for a fixed number of masses there is not a unique way to distribute them inside the volume circumscribed by the body. In the literature, [16, 46], the evenly spaced grid distribution is the most common, but in this work, an optimization procedure is developed to find the best allocation of the mascons within the body. This aspect will be addressed afterwards, and this approach will be referred to as *optimized mascons approach*.

2.2.3 Polyhedron Shape Approach

The polyhedron shape approach is based on the concept that any body of arbitrary shape can be approximated with a polyhedron having a variable number of faces. Then, exploiting the analytic form of the gravitational potential due to a homogeneous polyhedron having triangular faces [54], it is possible to evaluate the field generated by a very irregularly-shaped body. In fact, the geometry of the polyhedron can be extremely complex and the model can include concavities in the surface of the body (e.g. craters), overhangs, interior voids, caves, and even holes that extend all the way through the body (e.g. torus). Furthermore, fine details can be included without affecting the entire model, since it is not necessary to discretize the whole body at a constant resolution level.

The closed-form analytical expression of the exterior gravitational influence of a constant-density polyhedron guarantees that the gravity

field is exact for the given shape and density. The errors present in this model are entirely reduced to the errors in the body shape determination and in the chosen level of accuracy and discretization. However, the polyhedron is still an approximation of the real geometry of the body, but since most shape determinations have a limited resolution, this technique produces a field whose accuracy is consistent with the accuracy of the shape determination [55].

The solution obtained with the polyhedron approach is valid and exact at a distance from infinity up to the surface of the body. So, the region of divergence does not exist and the accuracy of the result is the same both for the potential and for the force. In addition, the analytical solution allows the calculation of the Laplacian of the gravitational potential without additional computational effort. This quantity can be used to determine if a field point is outside or inside the body: if the Laplacian vanishes, equation (2.3), the point is outside the body, in free space; otherwise the point is inside the body, Poisson's equation.

According to what has been said, this model is particularly valid and attractive for evaluating the gravitational forces that affect the surface dynamics or for analysing orbits and trajectories that exist close to the body. This aspect is exceptionally valuable for mission involving landings or operations in the close vicinity of an irregularly-shaped body [7].

Notwithstanding all these positive features, this method is markedly expensive in terms of the computational cost, as the entire surface must be summed over to achieve one single force value, and certainly this cost increases with the resolution of the shape discretization. With the current computing power available the time needed to make such calculations is still tolerable. This is especially true when parallel computing techniques are employed, since they significantly improve the computational speed.

In this work, the polyhedron approach assumes a constant-density model, and this is generally valid for many existing irregular bodies. In spite of this, the polyhedral approach also allows the simulation of density variations: they can be reproduced adding or subtracting small polyhedra internal to whole polyhedron model. The total mass of the body must be held constant, and this is made possible choosing the proper average density, σ, to be used in the homogeneous polyhedron analytical solution. In practice, being respectively σ_i and V_i the density and the volume of the i-th internal small additional polyhedron, σ can

be computed as:

$$\sigma = \frac{M - \sum_{i=1}^{N} \sigma_i V_i}{V - \sum_{i=1}^{N} V_i}, \tag{2.7}$$

where M is the total mass of the body and V the volume of the whole body shape.

Polyhedron Gravitation

In this section, the closed-form expression for the gravitational influence due to a homogeneous polyhedron is derived. The potential and acceleration components experienced by a unit mass can be expressed in terms of polyhedron's edges and vertex angles exploiting the Gauss Divergence theorem and the Green's theorem.

First of all, the real and complex shape of the body must be discretized using simple geometrical entities. In the polyhedral approach the surface of the body is represented by means of planar faces meeting along straight edges or at isolated points called vertices; this is the geometrical shape that will be herein referred to as *polyhedron*. It is important to note that the coordinates of the vertices are not sufficient to univocally define the shape, but the connective topology must be provided to have a fully and correctly described geometry.

The gravitational effect due to the whole body is then computed summing the contribution from each discrete tetrahedral element, as illustrated in figure 2.2.

In order to better explain this technique, it is worthwhile to recall the problem formulation that is used in the classical two-body system. Consider a unit mass particle P located at the field point (x, y, z), in terms of an inertial reference frame with origin in O. Assume that P is in motion under the attraction of another particle, P_m, with mass m and position (ξ, η, ζ), with respect to the same inertial reference frame in O. The position of the particle P is mathematically defined in terms of a Cartesian coordinate system with unit vectors $\hat{\mathbf{i}}$, $\hat{\mathbf{j}}$ and $\hat{\mathbf{k}}$ such that the position vector, $\mathbf{p}$, is expressed as $\mathbf{p} = x\hat{\mathbf{i}} + y\hat{\mathbf{j}} + z\hat{\mathbf{k}}$. The gravitational attraction, $\mathbf{f}$, experienced by P due to P_m can be expressed, with equation (2.1), as the gradient of a potential function U.

The discussion can be easily extended to bodies that are not point masses using equation (2.4). In this case, the dynamics of the unit point mass P is influenced by the gravitational force due to each differential

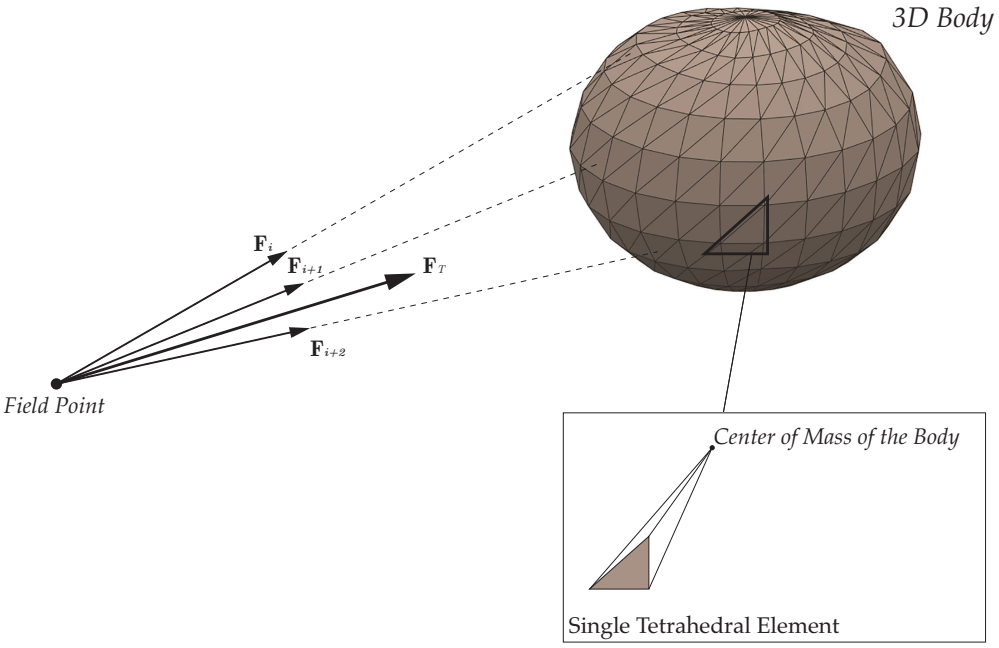

Figure 2.2: Polyhedron Shape Approach.

mass element P_m of the whole body $\boldsymbol{B}$, as can be seen in figure 2.3. The vector $\mathbf{r}$, whose Cartesian form is $\mathbf{r} = \Delta x\hat{\mathbf{i}} + \Delta y\hat{\mathbf{j}} + \Delta z\hat{\mathbf{k}}$ with $\Delta x = \xi - x$, $\Delta y = \eta - y$ and $\Delta z = \zeta - z$, locates the differential element P_m, with mass dm, with respect to the field point where P is. Thus, $r = \|\mathbf{r}\|$ is the distance from the field point to the differential mass element.

At this point, assuming a constant density, σ, throughout the body, the potential can be expressed with an integral over the volume, V, of $\boldsymbol{B}$. In fact, in this case $dm = \sigma dV$, and equation (2.4) can be rewritten as:

$$U = G\sigma \iiint_V \frac{1}{r}\, dV. \tag{2.8}$$

Now, the Gauss's theorem of divergence can be used, to manipulate equation (2.8), knowing a vector function, $\mathbf{w} = \mathbf{w}(\xi, \eta, \zeta)$, such that:

$$\nabla \cdot \mathbf{w} = \frac{1}{r}. \tag{2.9}$$

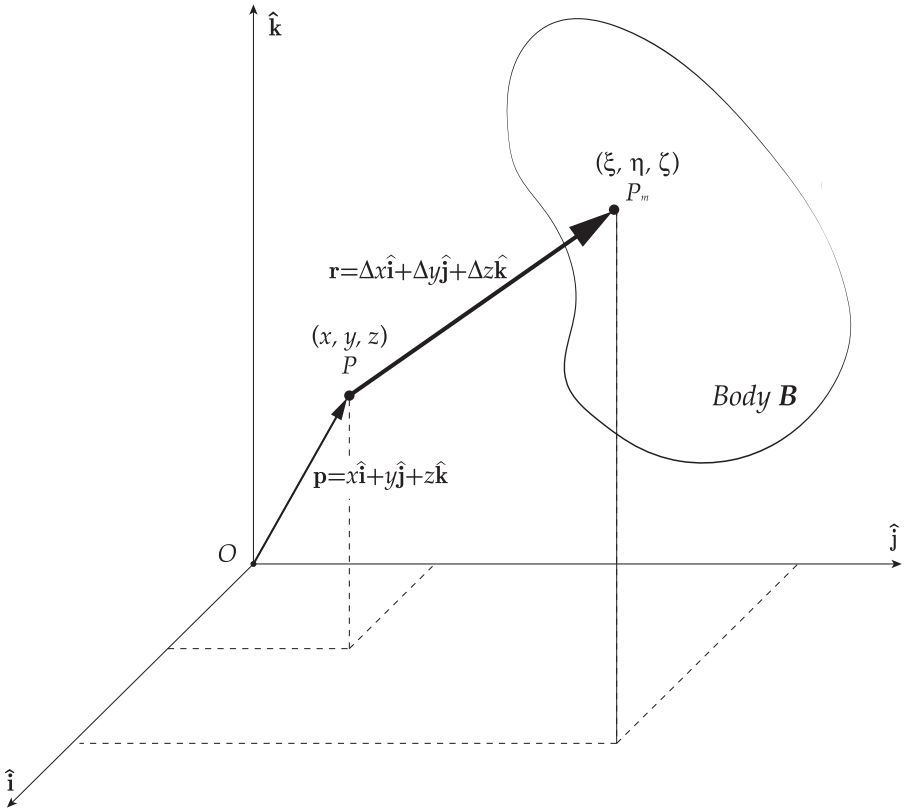

Figure 2.3: Point mass-Extended body problem formulation.

This theorem, already exploited and explained in section 2.1 to verify equation (2.3), allows to write:

$$\iiint_V \nabla \cdot \mathbf{w}\, dV = \iint_S \hat{\mathbf{n}} \cdot \mathbf{w}\, dS, \tag{2.10}$$

where S is the surface of the volume V and $\hat{\mathbf{n}}$ is the surface normal. This general relation is valid if the volume V is bounded and connected, its surface S is piecewise smooth and orientable, and the vector $\mathbf{w}$ and its derivative exist and are continuous throughout the volume and on its surface [18].

The polyhedron models that are used in this work satisfy these requirements, and in addition, the desired vector function that satisfies equation (2.9) is:

$$\mathbf{w} = \frac{1}{2}\hat{\mathbf{r}} = \frac{\mathbf{r}}{2r}. \tag{2.11}$$

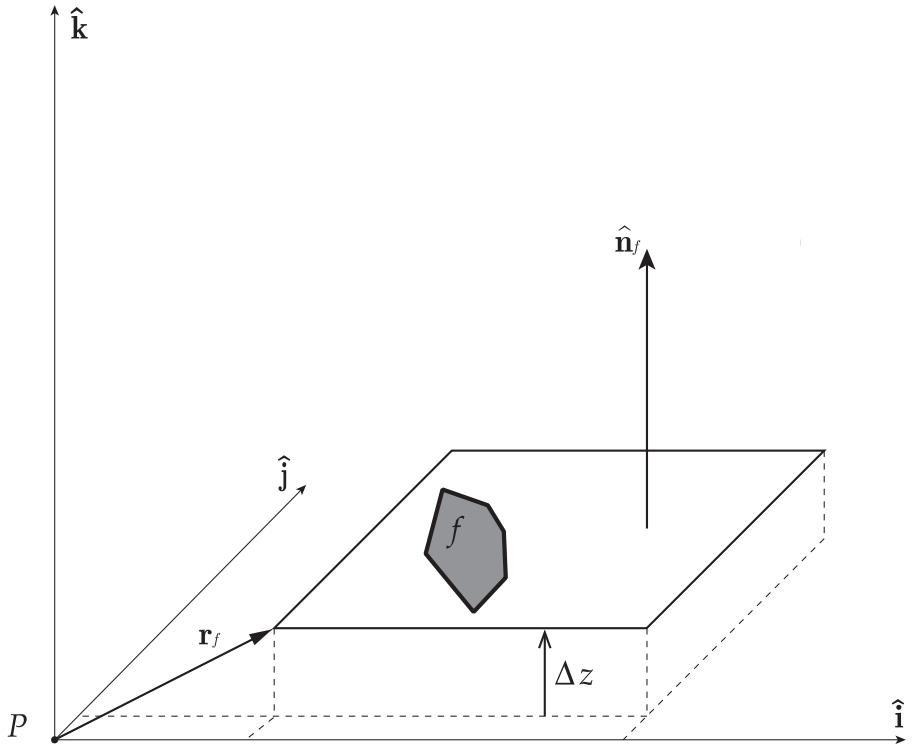

Figure 2.4: Reference frame for each face f.

Hence, it is possible to write:

$$U = G\sigma \iiint_V \frac{1}{r}\, dV = \frac{1}{2} G\sigma \iiint_V \nabla \cdot \hat{\mathbf{r}}\, dV = \frac{1}{2} G\sigma \iint_S \hat{\mathbf{n}} \cdot \hat{\mathbf{r}}\, dS. \quad (2.12)$$

It is important to note that, if the field point P lies on or within the body, $\hat{\mathbf{r}}$ is undefined where the field point coincides with the differential elements. Thus, this expression is considered to be valid only when the field point is exterior to the body.

Polyhedron Potential From now on, the 3D body $\boldsymbol{B}$ is a polyhedron and each polygonal face, f, has its own Cartesian reference frame with the origin at the field point, P. This coordinate system has unit vector $\hat{\mathbf{k}}$ aligned with the outward-pointing face normal vector, $\hat{\mathbf{n}}_f$. The other directions, $\hat{\mathbf{i}}$ and $\hat{\mathbf{j}}$, are parallel to the face as in figure 2.4.

The surface integral in equation (2.12) can be separated into a sum of integrals, one per each face:

$$U = \frac{1}{2}G\sigma \sum_{f \in faces} \iint_f \hat{\mathbf{n}}_f \cdot \hat{\mathbf{r}}\, dS = \frac{1}{2}G\sigma \sum_{f \in faces} \iint_f \hat{\mathbf{n}}_f \cdot \left(\frac{\mathbf{r}}{r}\right) dS$$
$$= \frac{1}{2}G\sigma \sum_{f \in faces} \hat{\mathbf{n}}_f \cdot \mathbf{r}_f \iint_f \frac{1}{r}\, dS, \tag{2.13}$$

where $\mathbf{r}_f$ is the vector that extends from P to any point in the face plane. Moreover, since the integration is performed on a planar surface the quantity $\Delta z = \hat{\mathbf{n}}_f \cdot \mathbf{r}$ is constant, and it is possible to replace $\mathbf{r} \to \mathbf{r}_f$, with the sole purpose to calculate Δz by a dot product with $\hat{\mathbf{n}}_f$.

The surface integral in equation (2.13) is the potential over a 2D planar region, and even if that equation is dealing with the polygon f, it is possible to derive a result for an arbitrary planar region, S. Indeed, with some algebraic manipulations:

$$\iint_S \frac{1}{r}\, dS = \iint_S \left(\frac{1}{r} + \frac{\Delta z^2}{r^3}\right) dS - \iint_S \frac{\Delta z^2}{r^3}\, dS$$
$$= \iint_S \left(\frac{r^2 - \Delta x^2}{r^3} + \frac{r^2 - \Delta y^2}{r^3}\right) dS - \Delta z \iint_S \frac{\Delta z}{r^3}\, dS, \tag{2.14}$$

where the equality $r^2 = \Delta x^2 + \Delta y^2 + \Delta z^2$ has been used.

Invoking the Green's theorem and defining a new quantity, ω_f, which will be discussed later, the potential of a planar region can be evaluated as a line integral around the boundary C of the region S and another term representing the entire planar surface:

$$\iint_S \frac{1}{r}\, dS = \oint_C \frac{1}{r}\left(\Delta x d\Delta y - \Delta y d\Delta x\right) - \hat{\mathbf{n}}_f \cdot \mathbf{r}_f\, \omega_f. \tag{2.15}$$

The boundary C must be crossed counterclockwise according to $\hat{\mathbf{n}}_f$ and the right-hand rule.

The quantity

$$\omega_f \stackrel{\text{def}}{=} \iint_S \frac{\Delta z}{r^3}\, dS, \tag{2.16}$$

is the solid angle, with sign, subtended by S when it is viewed from the field point, P. This fact can be proved considering a differential planar

surface, dS, distant r from the field point P. With reference to figure 2.5, $d\omega$ is also the projected area of dS onto a unit sphere centred on P, and it has normal direction represented by $\hat{\mathbf{r}}$. Hence, the area of $d\omega$, because of the projection, is:

$$d\omega = \hat{\mathbf{r}} \cdot \hat{\mathbf{n}}_f \frac{dS}{r^2} = \frac{\mathbf{r} \cdot \hat{\mathbf{n}}_f}{r^3} dS = \frac{\Delta z}{r^3} dS. \tag{2.17}$$

If equation (2.17) is integrated over the entire planar region, S, equation (2.16) is verified. For evident geometrical reasons the value of ω_f cannot be greater than the area of a hemisphere, which is equal to 2π sr. Furthermore, the sign of ω_f is in accordance with Δz: when $\hat{\mathbf{r}}$ points in the same general direction as $\hat{\mathbf{n}}_f$, ω_f is positive, otherwise it is negative. A more explicit form of this quantity will be presented subsequently.

At this point, equation (2.15) can be specialized for a planar face f of a polyhedron, that is, a polygon. In fact, the line integral integral can be written as a sum over polygon edges, e, and that equation becomes:

$$\iint_f \frac{1}{r}\, dS = \sum_{e \in edges} \int_e \frac{1}{r} \left(\Delta x d\Delta y - \Delta y d\Delta x\right) - \hat{\mathbf{n}}_f \cdot \mathbf{r}_f\, \omega_f. \tag{2.18}$$

Then, it is possible to define the normal vector to an edge of the polygon. With reference to figure 2.6, $\hat{\mathbf{n}}_{e_2}^B$ is the vector normal to the edge e_2, lies in the face plane, is orthogonal to both the edge direction, $\hat{\mathbf{s}}$, and the face normal vector, $\hat{\mathbf{n}}_B$, and points outward. In addition, knowing the coordinates of a generic fixed point, E_e, on the edge extension, the ones of an arbitrary point along e can be expressed as:

$$(\Delta x,\, \Delta y) = (\Delta x_{E_e} + s\cos\alpha_e,\, \Delta y_{E_e} + s\sin\alpha_e). \tag{2.19}$$

Thus, it is possible to evaluate the integral in equation (2.18) for a typical edge e as:

$$\begin{aligned}
&\int_e \frac{1}{r} \left(\Delta x d\Delta y - \Delta y d\Delta x\right) \\
&\quad = \int_e \frac{1}{r} \left[\left(\Delta x_{E_e} + s\cos\alpha_e\right)\sin\alpha_e - \left(\Delta y_{E_e} + s\sin\alpha_e\right)\cos\alpha_e\right] ds \\
&\quad = \left(\Delta x_{E_e}\sin\alpha_e - \Delta y_{E_e}\cos\alpha_e\right) \int_e \frac{1}{r} ds = \hat{\mathbf{n}}_e^f \cdot \mathbf{r}_e^f \int_e \frac{1}{r} ds,
\end{aligned} \tag{2.20}$$

where $\mathbf{r}_e^f = \Delta x_{E_e}\hat{\mathbf{i}} + \Delta y_{E_e}\hat{\mathbf{j}} + \Delta z_{E_e}\hat{\mathbf{k}}$ is the vector from the field point, P, to the fixed point E_e.

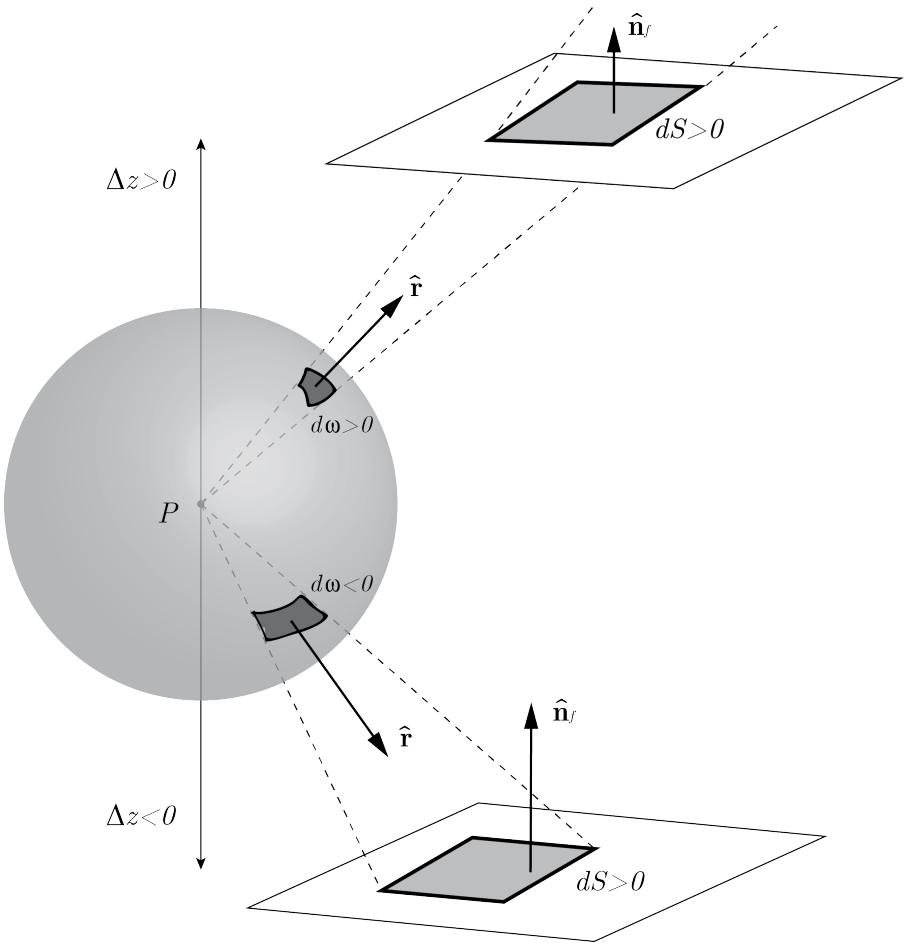

Figure 2.5: Projection of a differential surface dS onto a unit sphere centred in P. The spherical area $d\omega$ has the same sign of Δz.

It should also be noted that $\hat{\mathbf{n}}_e^f \cdot \hat{\mathbf{i}} = \sin\alpha_e$, $\hat{\mathbf{n}}_e^f \cdot \hat{\mathbf{j}} = -\cos\alpha_e$ and $\hat{\mathbf{n}}_e^f \cdot \hat{\mathbf{k}} = 0$. Furthermore, the integral in the previous equation is the potential of a 1D straight line. A new quantity, L_e^f, can be defined to indicate the potential of a generic edge e of face f:

$$L_e^f \stackrel{\text{def}}{=} \int_e \frac{1}{r}\, ds. \tag{2.21}$$

Preceding studies, [26, 54], proved that the aforementioned quantity is expressed only in terms of the edge length, e, and of the distances, l_1 and l_2, from the field point P to the edge's ends, in figure 2.6 E_{P1} and E_{P2}:

$$L_e^f = \ln \frac{l_1 + l_2 + e}{l_1 + l_2 - e}. \tag{2.22}$$

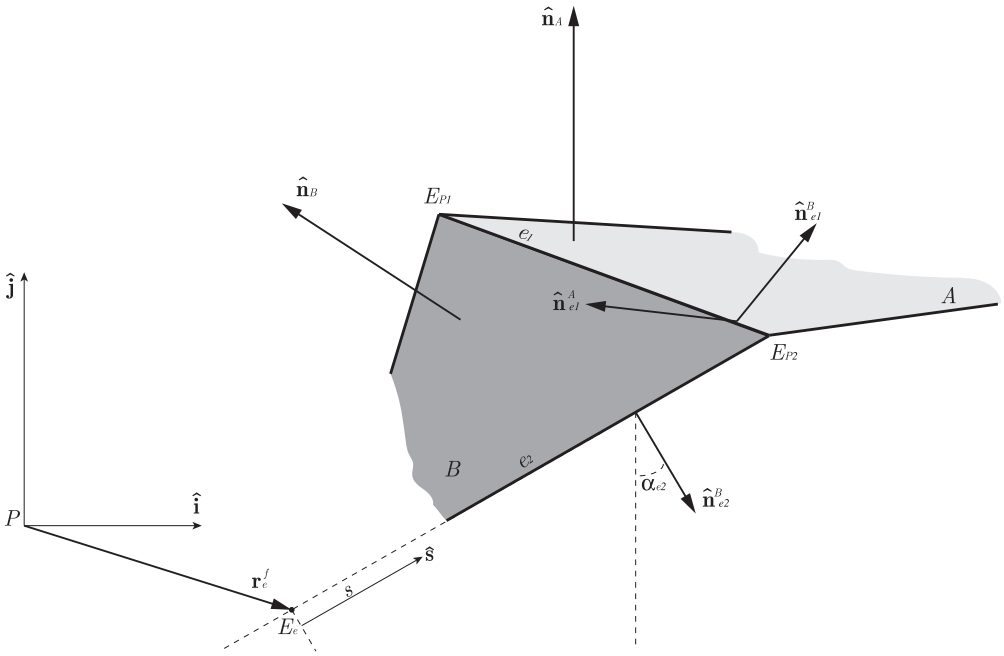

Figure 2.6: Edge e_1 between faces A and B and edge e_2 on face B.

Substituting these results valid for a polygon into the polyhedron potential expression, equation (2.13), it is possible to write:

$$\begin{aligned} U &= \frac{1}{2} G\sigma \sum_{f \in faces} \hat{\mathbf{n}}_f \cdot \mathbf{r}_f \iint_f \frac{1}{r}\, dS \\ &= \frac{1}{2} G\sigma \sum_{f \in faces} \left(\sum_{e \in edges} \mathbf{r}_f \cdot \hat{\mathbf{n}}_f \hat{\mathbf{n}}^f_e \cdot \mathbf{r}^f_e \, L^f_e \right) - \frac{1}{2} G\sigma \sum_{f \in faces} \mathbf{r}_f \cdot \hat{\mathbf{n}}_f \hat{\mathbf{n}}_f \cdot \mathbf{r}_f \, \omega_f . \end{aligned} \tag{2.23}$$

The above equation can be simplified making some considerations about the involved quantities. First, for all the edges e_i of a face f the substitution, $\mathbf{r}_f \rightarrow \mathbf{r}^f_e$, is valid because $\Delta z = \mathbf{r}_f \cdot \hat{\mathbf{n}}_f = \mathbf{r}^f_e \cdot \hat{\mathbf{n}}_f$. Then, considering an edge in common with two faces, like e_1 in figure 2.6, it is possible to choose the same $\mathbf{r}^f_e$ for both faces, i.e. $\mathbf{r}^A_{e_1} = \mathbf{r}^B_{e_1} = \mathbf{r}_{e_1}$. Moreover, the integrals $L^A_{e_1}$ and $L^B_{e_1}$ are equals to L_{e_1} for both A and B, because they depend on quantities that are the same for given field point and edge. The nested sums becomes a single summation over all the polyhedron

edges, again with reference to figure 2.6:

$$\begin{aligned}
&\sum_{f\in faces}\left(\sum_{e\in edges}\mathbf{r}_e^f\cdot\hat{\mathbf{n}}_f\hat{\mathbf{n}}_e^f\cdot\mathbf{r}_e^f\,L_e^f\right)\\
&=\cdots+\mathbf{r}_{e_1}^A\cdot\hat{\mathbf{n}}_A\hat{\mathbf{n}}_{e_1}^A\cdot\mathbf{r}_{e_1}^A\,L_{e_1}^A+\cdots+\mathbf{r}_{e_1}^B\cdot\hat{\mathbf{n}}_B\hat{\mathbf{n}}_{e_1}^B\cdot\mathbf{r}_{e_1}^B\,L_{e_1}^B+\ldots\\
&=\cdots+\mathbf{r}_{e_1}\cdot\left(\hat{\mathbf{n}}_A\hat{\mathbf{n}}_{e_1}^A+\hat{\mathbf{n}}_B\hat{\mathbf{n}}_{e_1}^B\right)\cdot\mathbf{r}_{e_1}\,L_{e_1}+\ldots\\
&=\cdots+\mathbf{r}_{e_1}\cdot\mathbb{E}_{e_1}\cdot\mathbf{r}_{e_1}\,L_{e_1}+\ldots\\
&=\sum_{e\in edges}\mathbf{r}_e\cdot\mathbb{E}_e\cdot\mathbf{r}_e\,L_e,
\end{aligned}\tag{2.24}$$

where $\mathbf{r}_e$ is a vector from the field point to any point on the generic edge e or its infinite extension, and

$$\mathbb{E}_e\stackrel{\text{def}}{=}\hat{\mathbf{n}}_{f_1}\hat{\mathbf{n}}_e^{f_1}+\hat{\mathbf{n}}_{f_2}\hat{\mathbf{n}}_e^{f_2}\tag{2.25}$$

is a dyad associated with e and the two adjoining faces f_1 and f_2. This dyad is expressed in matrix notation as the sum of two outer products, i.e. $\hat{\mathbf{n}}_{f_1}(\hat{\mathbf{n}}_e^{f_1})^T+\hat{\mathbf{n}}_{f_2}(\hat{\mathbf{n}}_e^{f_2})^T$ [17].

It is possible to define a dyad even for each face f in the polyhedron shape:

$$\mathbb{F}_f\stackrel{\text{def}}{=}\hat{\mathbf{n}}_f\hat{\mathbf{n}}_f,\tag{2.26}$$

which is the outer product of $\hat{\mathbf{n}}_f$ with itself.

$\mathbb{F}_f$ and $\mathbb{E}_e$ are 3×3 dyads, and it can be shown that they are both symmetric [55]. Dyads are intrinsically convenient for the expression of the final result; they represent the transformation from edge and face frames to a common body frame, which allows the summation over all the elemental gravitational potential contributions.

The previous results and definitions can be included in equation (2.23), and the potential of a constant-density polyhedron can be expressed as:

$$U=\frac{1}{2}G\sigma\sum_{e\in edges}\mathbf{r}_e\cdot\mathbb{E}_e\cdot\mathbf{r}_e\,L_e-\frac{1}{2}G\sigma\sum_{f\in faces}\mathbf{r}_f\cdot\mathbb{F}_f\cdot\mathbf{r}_f\,\omega_f.\tag{2.27}$$

Polyhedron Attraction The attraction exerted by a 3D polyhedron in the surrounding space can be derived differentiating the expression of the potential in equation (2.27):

$$\nabla U=\frac{1}{2}G\sigma\nabla\sum_{e\in edges}\mathbf{r}_e\cdot\mathbb{E}_e\cdot\mathbf{r}_e\,L_e-\frac{1}{2}G\sigma\nabla\sum_{f\in faces}\mathbf{r}_f\cdot\mathbb{F}_f\cdot\mathbf{r}_f\,\omega_f.\tag{2.28}$$

However, this expression can be simplified analysing the attraction of a 2D polygon, which can be obtained from the definition of a general planar region's potential. In fact, differentiating equation (2.15) the result is:

$$\nabla \iint_S \frac{1}{r}\, dS = -\hat{\mathbf{i}} \oint_C \frac{1}{r} d\Delta y + \hat{\mathbf{j}} \oint_C \frac{1}{r} d\Delta x + \hat{\mathbf{k}}\, \omega_f, \tag{2.29}$$

where the Green's theorem has been used again. Now, if the planar region is restricted to be a polygon, f, the boundary integrals can be substituted with a sum of integrals along the edges:

$$\begin{aligned}
\nabla \iint_f \frac{1}{r}\, dS &= \sum_{e \in edges} \left[-\hat{\mathbf{i}} \int_e \frac{1}{r} d\Delta y + \hat{\mathbf{j}} \int_e \frac{1}{r} d\Delta x \right] + \hat{\mathbf{k}}\, \omega_f \\
&= \sum_{e \in edges} \left[-\hat{\mathbf{i}} \sin\alpha_e \int_e \frac{1}{r} ds + \hat{\mathbf{j}} \cos\alpha_e \int_e \frac{1}{r} ds \right] + \hat{\mathbf{k}}\, \omega_f \\
&= -\sum_{e \in edges} \hat{\mathbf{n}}_e^f L_e^f + \hat{\mathbf{n}}_f \omega_f.
\end{aligned} \tag{2.30}$$

The same result can also be obtained differentiating directly the potential of a single polyhedron's face, as contained in equation (2.23), and considering that $\nabla \mathbf{r} = -\mathbb{I}^{3\times 3}$:

$$\begin{aligned}
&\nabla \left(\sum_{e \in edges} \hat{\mathbf{n}}_e^f \cdot \mathbf{r}_e^f\, L_e^f - \hat{\mathbf{n}}_f \cdot \mathbf{r}_f\, \omega_f \right) \\
&= -\sum_{e \in edges} \hat{\mathbf{n}}_e^f L_e^f + \hat{\mathbf{n}}_f \omega_f + \left[\sum_{e \in edges} \hat{\mathbf{n}}_e^f \cdot \hat{\mathbf{r}}_e^f \nabla L_e^f - \hat{\mathbf{n}}_f \cdot \hat{\mathbf{r}}_f \nabla \omega_f \right].
\end{aligned} \tag{2.31}$$

Equation (2.30) and equation (2.31) represent the same quantity and therefore the last two terms in the square brackets must vanish:

$$\sum_{e \in edges} \hat{\mathbf{n}}_e^f \cdot \hat{\mathbf{r}}_e^f \nabla L_e^f = \hat{\mathbf{n}}_f \cdot \hat{\mathbf{r}}_f \nabla \omega_f, \tag{2.32}$$

which can be extended in the 3D case. Multiplying by $\mathbf{r}_f \cdot \hat{\mathbf{n}}_f$, summing all over the polyhedral faces and expanding the nested sums as before, equation (2.32) becomes:

$$\sum_{e \in edges} \mathbf{r}_e \cdot \mathbb{E}_e \cdot \mathbf{r}_e \nabla L_e = \sum_{f \in faces} \mathbf{r}_f \cdot \mathbb{F}_f \cdot \mathbf{r}_f \nabla \omega_f. \tag{2.33}$$

At this point, using equation (2.33), the attraction of a 3D polyhedron can be expressed, from equation (2.28), as:

$$\nabla U = -G\sigma \sum_{e \in edges} \mathbb{E}_e \cdot \mathbf{r}_e \, L_e + G\sigma \sum_{f \in faces} \mathbb{F}_f \cdot \mathbf{r}_f \, \omega_f. \tag{2.34}$$

Gravity Gradient Matrix The symmetric gravity gradient matrix of second partial derivatives can be calculated differentiating the previous equation (2.34) and canceling terms, similarly to what has been done in the previous paragraph:

$$\nabla \left(\nabla U \right) = G\sigma \sum_{e \in edges} \mathbb{E}_e \, L_e - G\sigma \sum_{f \in faces} \mathbb{F}_f \, \omega_f. \tag{2.35}$$

Laplacian of the Potential The Laplacian $\nabla^2 U$ can be computed as the trace of the gravity gradient matrix, but it can also be easily derived from equation (2.13):

$$\begin{aligned} \nabla^2 U &= \frac{1}{2} G\sigma \sum_{f \in faces} \nabla^2 \iint_f \hat{\mathbf{n}}_f \cdot \hat{\mathbf{r}} \, dS \\ &= \frac{1}{2} G\sigma \sum_{f \in faces} \nabla^2 \iint_f \hat{\mathbf{k}} \cdot \left[\hat{\mathbf{i}} \frac{\Delta x}{r} + \hat{\mathbf{j}} \frac{\Delta y}{r} + \hat{\mathbf{k}} \frac{\Delta z}{r} \right] dS \\ &= \frac{1}{2} G\sigma \sum_{f \in faces} \iint_f \nabla^2 \frac{\Delta z}{r} \, dS = G\sigma \sum_{f \in faces} \iint_f \frac{-\Delta z}{r^3} \, dS. \end{aligned} \tag{2.36}$$

Recalling equation (2.16) the Laplacian of U is:

$$\nabla^2 U = -G\sigma \sum_{f \in faces} \omega_f. \tag{2.37}$$

Since all the previous quantities in equations (2.27), (2.34) and (2.35) require the calculation of ω_f, the Laplacian can be obtained at practically no additional computational cost. In addition, as previously mentioned, a dynamical simulation can use the Laplacian to determine whether a point is inside or outside the body. Indeed, in agreement with equation (2.3), the sum over all ω_f vanishes if the field point is outside the polyhedron, and it is equals to 4π inside, satisfying the Poisson's equation for gravity:

$$\nabla^2 U = -4\pi G\sigma. \tag{2.38}$$

In order to conclude the discussion about the polyhedron gravitation, a simple way to compute ω_f is presented. Similarly to the logarithmic equation (2.22) that is used to calculate L_e, the value of ω_f can be easily obtained from an expression valid for a triangular face f bounded by vertices E_{Pi}, E_{Pj}, E_{Pk} as:

$$\omega_f = 2 \arctan \frac{\mathbf{r}_i \cdot \mathbf{r}_j \times \mathbf{r}_k}{r_i r_j r_k + r_i \left(\mathbf{r}_j \cdot \mathbf{r}_k\right) + r_j \left(\mathbf{r}_k \cdot \mathbf{r}_i\right) + r_k \left(\mathbf{r}_i \cdot \mathbf{r}_j\right)}. \tag{2.39}$$

All the previously defined techniques to model the gravitational field generated by irregularly-shaped bodies are available and they can be used with different levels of fidelity to compute approximated values of the gravitational potential and acceleration in the vicinity of these celestial objects. The most appropriate model depends on the specific application, since each approach has advantages and drawbacks. Nevertheless, they all require information on the actual shape and mass distribution of the real body and for this reason, shape and mass models are required.

2.3 Physical Model of the Body

The precise and complete physical model of irregularly-shaped bodies is usually not available. The knowledge about topography of a typical celestial object is often acquired by means of radar observations and optical light curves measured from Earth, and only in few cases those data are coming from a deep space mission that flew close to one of these small bodies in the Solar System [6]. But, even in this latter case, the physical model of the body is a reconstruction from indirect measurements and so it is exact within a certain accuracy. However, the available precision is generally acceptable for the majority of real applications, and moreover, there is a large abundance of data available on several bodies, even though they are only a tiny fraction of all the existing minor space bodies.

The information about the mass and the mass distribution of these celestial objects is sometimes more inaccurate with respect to the topographical data. The difficulty in determining minor bodies masses lies in their small size and in the techniques that are usually employed to compute mass values, based on perturbations of asteroids [20]. Frequently, the total mass of a body is also computed from the shape volume and from an assumed constant bulk density that is typical for the class of

objects that is being considered [27]. These general values of density are studied and listed in literature according to the average soil composition and porosity of categories of analogous minor bodies.

The gravitational models that are presented in this research work are all obtained with the mascons approach and the polyhedron approach. These two techniques require only the shape model and one quantity among total mass and bulk density to be correctly applied. In fact, knowing the geometry of a body it is possible to compute its volume, and considering a homogeneous object, the values of density, mass and volume are easily related together. In addition, as will be explained in the following, also the rotational inertia properties can be evaluated from these data with a simple discretization process. Obviously, the absolute values of the obtained results are influenced by the assumed values in the physical properties of the body, although the general behaviours and conclusions are somewhat independent from the arbitrary assumptions. For this reason, the validity of this kind of analysis is beyond the availability of exact data and can be applied to the dynamical environment of a generic celestial body, even if its physical properties are known only with a large level of approximation.

2.3.1 Shape Models

The *shape model* of a celestial body represents its topographical characteristics by means of certain model parameters. Usually the raw data coming from an Astronomical Observatory or from a Deep Space Probe must be elaborated, reduced and transformed in a topographic map, representing the surface of the body, for the successive analyses. This map is then transformed in a *vertex model*, consisting on a finite set of point describing the geometry of the body, which is often derived from the best-fit harmonic model of the topographic map: practically, it is just a point discretization of the measured and processed surface of the body.

Then, all these single points must be converted in a topological entity to have the complete and final shape representation. Therefore, a *connectivity list* between the numbered vertices must be provided, indeed without this element is not possible to univocally define the shape of the body. The connectivity list is simply a list of the vertices that must be connected together in a certain order to obtain the elemental constituent of the whole shape model. In this case the polyhedron representation in composed by several tetrahedra having one vertex in the centre of mass of the body, hence, the connectivity list is a $N \times 3$ matrix, where each

row defines one of the N triangular faces of the polyhedron, and each triangle is the base of a tetrahedron.

So, each shape model is initially defined only by its *vertex list* that indicates the position of each of the N_v vertices with respect to a certain reference frame. In general, their coordinates are expressed in a Cartesian or in a Spherical reference system centred in the centre of mass of the body. From the $N_v \times 3$ vertex list the *convex hull* and the volume of the body can be obtained; the former is the smallest convex set that contains all the vertices in the Euclidean space, and can be used as the volume to be filled with discrete point masses in the mascons approach.

At this point, the connectivity list can be computed performing a *Delaunay triangulation* in a 3D Euclidean space, or can be obtained through a longitudinal and latitudinal connection pattern of the vertices [24]. In this work a Delaunay triangulation is used to obtain the final mesh of the body, since it is more flexible, scalable and allows performing a large variety of topological and geometric queries on the shape model. This triangulation scheme has been deeply developed to improve the meshing algorithms that are used in the finite element codes, and it tries to find a three-dimensional triangulation such that no vertex is inside the circumsphere of any triangle in the mesh.

The shape models that are here presented consist in a vertex list, expressed in a 3D Cartesian reference with origin in the centre of mass and aligned with the principal inertia axes of the uniform body. The coordinate system is oriented in a way that the $\hat{\mathbf{z}}$ direction is the one of the maximum inertia axis, while the $\hat{\mathbf{x}}$ is along the minimum inertia axis and $\hat{\mathbf{y}}$ completes the right-hand reference frame. The connectivity list define univocally the triangulation and it is used to obtain all the quantities that are then necessary to fully describe the irregular body, e.g. the Edge List, the Face Normal List, the Edge Normal List and so on.

The bodies that will be analysed in this thesis are: 67P Churyumov-Gerasimenko (67P C-G) comet, 216 Kleopatra Main-Belt asteroid, 4179 Toutatis Apollo-Alinda asteroid, 433 Eros Amor asteroid and 1580 Betulia Amor asteroid. These data are all coming from the Rosetta Mission[1] of ESA, from the Planetary Data System Asteroid and Dust Archive[2] of NASA and from the Asteroid Radar Research Group[3] of JPL.

Analysing the 67P Churyumov-Gerasimenko model in figure 2.7, it can be noted the accuracy of the surface representation, which is highly

[1] http://rosetta.esa.int
[2] http://sbn.psi.edu/pds
[3] http://echo.jpl.nasa.gov

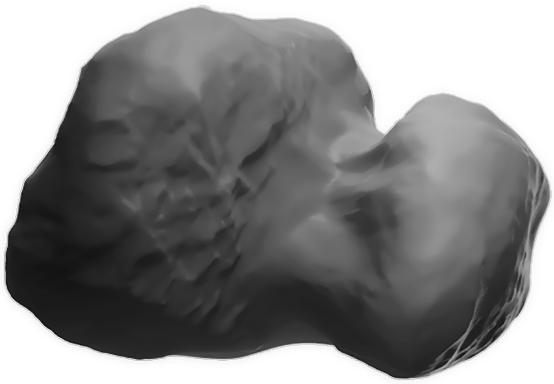

Figure 2.7: 67P Churyumov-Gerasimenko model.

detailed thanks to the images acquired by the OSIRIS camera on ESA's Rosetta spacecraft during the mission around the comet. Moreover, now it is evident why the spherical models, and even the harmonic expansion models, are not capable to correctly represent the field of a so irregularly-shaped body.

The render of the 67P Churyumov-Gerasimenko comet has been realized with the same topographical data that are used to create the polyhedron shape model. In fact, the full triangulation from the raw data, which has approximately 66000 faces, is rescaled in order to obtain the polyhedron shape model that is used in this thesis to compute the gravitational field generated by the body. The number of triangles used to discretize the surface of the object is fully arbitrary and determines the resolution of the polyhedron mesh. Clearly, this characteristic affects directly the accuracy of the gravitational potential and consequently the required computational time.

In figure 2.8, the polyhedron shape model of the comet is shown with two different discretization resolutions; they are typically used in this thesis and will be referred to as Lo-Fi polyhedron model, in figure 2.8a, and Hi-Fi polyhedron model, in figure 2.8b. The order of magnitude of the number of faces in the former is 10^3, while in the latter is 10^4.

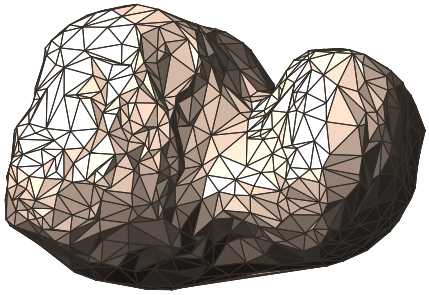

(a) Lo-Fi Polyhedron Discretization with $\sim 10^3$ faces

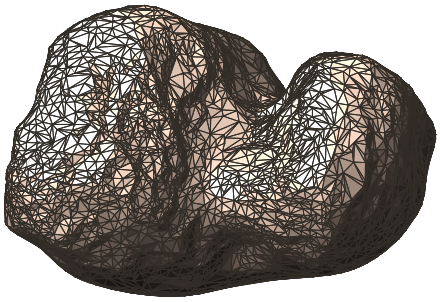

(b) Hi-Fi Polyhedron Discretization with $\sim 10^4$ faces

Figure 2.8: Polyhedron Shape Model for 67P Churyumov-Gerasimenko. (Shape Data Credits: ESA, Rosetta, MPS for OSIRIS Team, MPS, UPD, LAM, IAA, SSO, INTA, UPM, DASP, IDA [13].)

Since, the accuracy of the gravity potential depends on the resolution of the mesh, the fidelity of the gravity field can be directly verified from the accuracy of the approximated polyhedral shape. Thus, the Hi-Fi model is assumed as the *model of reality* and will be used as a reference to evaluate the accuracy of another model with a lower resolution.

In figure 2.9, the shape model of the asteroid 216 Kleopatra is shown with a discretization resolution that is intermediate between the Hi-Fi

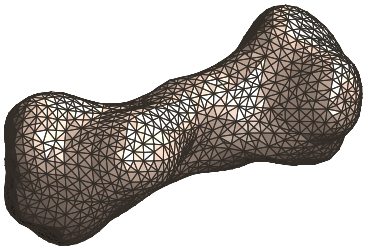

Figure 2.9: Polyhedron Shape Model for 216 Kleopatra. (Shape Data Credits: NASA, PDS, Arecibo Observatory, 2004 Ostro et al. [37].)

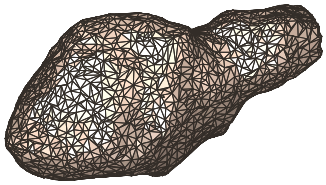

Figure 2.10: Polyhedron Shape Model for 4179 Toutatis. (Shape Data Credits: NASA, PDS, Goldstone Solar System Radar, Arecibo Observatory, 1995 Hudson et al. [21].)

and the Lo-Fi model. Similarly, respectively in figures 2.10 to 2.12, the shape models of the asteroids 4179 Toutatis, 433 Eros and 1580 Betulia are shown.

The majority of these models is obtained by means of ground observation and only the data for 433 Eros and 67P Churyumov-Gerasimenko are coming from deep space fly-bys missions. However, in this thesis, they are all assumed to have the same precision and they are employed without distinction.

It is evident that these bodies are all different and they are used as a reference for characteristic shapes of typical celestial objects. Namely, the comet Churyumov-Gerasimenko is representative for *two-masses* bodies,

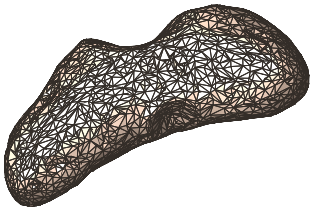

Figure 2.11: Polyhedron Shape Model for 433 Eros. (Shape Data Credits: NASA, Johns Hopkins APL, NEAR, Multi-Spectral Imager, 2002 Miller et al. [30].)

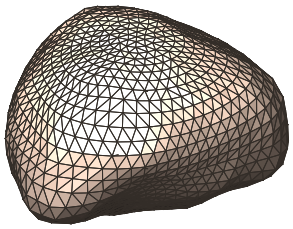

Figure 2.12: Polyhedron Shape Model for 1580 Betulia. (Shape Data Credits: California Institute of Technology, JPL, 2007 Magri et al. [27].)

the asteroid Kleopatra for the so-called *dog-bone* shape, Toutatis and Eros for *elongated* objects, and Betulia for *quasi-spherical* asteroids.

The polyhedral representation is extremely flexible and can be used with any shape, but the approximation for non-convex geometries can be somewhat challenging. Indeed, a part of the volume of a single shape element may include some mass beyond the physical volume of a concave body, which is discretized with constant density tetrahedra having a vertex in the centre of mass. Consequently, the meshing algorithm must have a check to ensure that each tetrahedron in the shape discretization is solid in terms of the physical volume of the body.

From a query on the shape model of the body, several physical quantities can be obtained; they are important for the following steps and

Table 2.1: Shape properties of reference irregular bodies.

		V [km^3]	D_E [km]	D_P [km]
67P	C-G	25.11	4.49	2.16
216	Kleopatra	1.11×10^6	214.52	52.42
4179	Toutatis	8.60	4.43	2.23
433	Eros	2.98×10^3	31.65	11.33
1580	Betulia	83.25	6.29	4.12

for the complete description of the object. Some of them are listed in table 2.1, including the body volume, V, and the diameters along the minimum and maximum inertia axes, respectively D_E and D_P. These values allow a preliminary understanding of the characteristic dimensions of the analysed bodies, which in this case have their linear dimensions in the order of $\sim 10^0$km to 10^2km.

2.3.2 Inertia Properties

The physical model of these bodies can be completed including the information about the inertia properties. In this work, the total mass of the objects is taken from the literature and then the density is derived exploiting the volume obtained from the shape model. In table 2.2, the masses of the considered celestial objects are shown with their respective sources.

It is worth noting that these values have often large uncertainties, and in the references different values for a single body can be found. However, the validity of the analysis that is presented in this work is independent from the available data, because, even if the computations have been performed on selected bodies, the presented methods and approach apply to any kind of irregular object. Hence, the study can be performed again when a new and more refined physical model is available.

Using the information available in tables 2.1 and 2.2 the density of the uniform body can be easily calculated, and the obtained values are reported in table 2.3. From this list, the physical differences between asteroids and comets is evident, with a difference of an order of magnitude between their densities. Obviously, this can be easily explained considering the different origins and internal structures of the two kind of celestial objects.

Table 2.2: Mass of reference irregular bodies.

		M [kg]
67P	C-G [12]	1.00×10^{13}
216	Kleopatra [11]	4.64×10^{18}
4179	Toutatis [57]	5.00×10^{13}
433	Eros [30]	6.69×10^{15}
1580	Betulia [27]	1.63×10^{14}

Table 2.3: Density of reference irregular bodies.

		σ [kg m^{-3}]
67P	C-G	398.24
216	Kleopatra	4180.18
4179	Toutatis	5813.95
433	Eros	2244.96
1580	Betulia	1957.95

Moreover, from the data contained in the shape model and from the mass of the object, also the rotational inertia properties of the body can be computed. In the present work, they are obtained directly from the constant density shape model, as the moments of inertia with respect to its principal axes $\hat{\mathbf{x}}$, $\hat{\mathbf{y}}$ and $\hat{\mathbf{z}}$. In fact, the rotational inertia of a continuous body with respect to a specified axis, α, is defined as:

$$I_\alpha = \int_M \mathbf{r}_\alpha^2 \, dM, \tag{2.40}$$

where $\mathbf{r}_\alpha$ is the position of the differential mass element dM with respect to the axis α. This expression can be extended to a body that is composed by an assembly of several discrete masses, converting the integral to a summation.

So, the shape model of the body can be filled with N_m masses of equal mass $m = \frac{M}{N_m}$, and the principal moments of inertia are:

$$I_x = m \sum_{i=1}^{N} \mathbf{r}_{x_i}^2, \quad I_y = m \sum_{i=1}^{N} \mathbf{r}_{y_i}^2, \quad I_z = m \sum_{i=1}^{N} \mathbf{r}_{z_i}^2. \tag{2.41}$$

where $\mathbf{r}_{x_i}$, $\mathbf{r}_{y_i}$, $\mathbf{r}_{z_i}$ are the distances of each mass m from the respective principal axes. The resulting values are summarized in table 2.4, and

Table 2.4: Principal Moments of Inertia of reference irregular bodies.

		I_x [kg m^2]	I_y [kg m^2]	I_z [kg m^2]
67P	C-G	9.64×10^{18}	1.74×10^{19}	1.86×10^{19}
216	Kleopatra	3.05×10^{27}	2.08×10^{28}	2.10×10^{28}
4179	Toutatis	1.86×10^{19}	5.58×10^{19}	5.92×10^{19}
433	Eros	1.02×10^{23}	4.93×10^{23}	5.01×10^{23}
1580	Betulia	4.21×10^{20}	5.02×10^{20}	6.36×10^{20}

according to the shape model definition, $\hat{\mathbf{x}}$ and $\hat{\mathbf{z}}$ are correctly the minimum and the maximum principal inertia axes, respectively. Furthermore, these values agree with the shape of the object, considering, for example, the almost axisymmetric Kleopatra or the quasi-spherical Betulia.

2.4 Dynamical Model

The dynamics of a particle around irregularly-shaped bodies is extremely different from the familiar two-body problem, where the main attractor is reduced to a point mass and analytical solutions exist. In that case, the motion of a particle around a main body is fully described by conic sections, i.e. circles, ellipses, hyperbolas and parabolas, according to Kepler's laws of planetary motion. However, when the main attractor cannot be considered equivalent to a point mass, that is, the body is not centrobaric, the equations of motion do not allow an analytical solution and the resulting dynamics is a way more complex than the Keplerian one. In this case, a numerical investigation is necessary, from the computation of the gravitational attraction in any field point to the propagation of the trajectory. In order to fully describe the environment in the vicinity of one irregular body is necessary to take into account the rotational dynamics of the main attractor itself, and therefore the orbital evolution of a particle is coupled with the motion of the primary. This characteristic leads to trajectories that are dependent from the spin state of the central attractor. If this is uniformly rotating about a principal inertia axis, one integral of motion can be found and thus, similarly to the circular restricted three-body problem, surfaces bounding the motion of the particle and equilibrium solutions exist. Nevertheless, these features disappear if the rotational dynamics of the main body is more complex and the angular velocity is varying in time.

2.4.1 Model Definition

The presented dynamical model deals with two bodies: an irregularly-shaped rigid central attractor and a massless particle. Namely, the less massive body is sufficiently small with respect to the primary to be modelled as a massless point, regardless of its shape. Some assumptions are required to formulate the problem with a balance between a reasonable level of complexity and an acceptable fidelity of the obtained results.

The assumptions related with the computation of the gravitational field are described in the dedicated sections 2.2.2 and 2.2.3 and depend on the technique, polyhedron or mascons, which is used to originate the gravity model. Anyway, the major assumption in the gravitational model is the constant density body, and given a certain resolution in the asteroid or comet discretization, the use of an approximation of the real gravity force in the equations of motion. It is worthwhile to point out that even the Hi-Fi model does not allow the exact description of gravitational field, both for the limits of the modelling techniques and for the uncertainties in the available body physical characteristics; hence, there is no possibility to have the exact representation of the dynamical environment around irregularly-shaped bodies, even using numerical analysis.

The first assumption contained in the dynamical model is related with the orbital motion of the primary, in fact it is considered to be in a circular and planar orbit around the Sun with radius equal to the semi-major axis of the real orbit of the body. Consequently, the perturbations are included only in the integration of the rotational motion of the main attractor and these are limited to third body, Sun, gravitational effect, Solar Radiation Pressure, YORP effect and internal dissipation of energy. For what concern the comet 67P Churyumov-Gerasimenko the presence of the coma, comet outgassing, is neglected; the model is valid, in this case, only when the body is far from the Sun and the comet activity is low.

Then, the model is developed in a rotating frame that is fixed with respect to the irregular body, and accordingly, the rotational dynamics of the primary is coupled with the orbital dynamic around the same body. The use of this rotating frame facilitates the numerical investigation and understanding of the motion of a particle in the dynamical environment of the irregular asteroid or comet.

The particle is assumed to be massless and does not affect the motion of the main body, defining a restricted two-body problem, where the massless particle gives no contribution to the global gravitational force.

The orbital dynamics is unperturbed and it is influenced only by the irregular gravitational attraction and the rotational motion of the asteroid. In practice, the perturbative effects are assumed to act only indirectly on the motion of the particle through the effects on the attitude of the primary.

2.4.2 Reference Frames Definition

The description of the dynamics around an irregular shape body can be derived or in an inertial reference frame or in a rotating one. As previously said, the rotating body-fixed coordinate system has several advantages in spite of the necessity to add the fictitious forces proper of the non-inertial reference frames. In fact, first of all, the body-fixed frame avoid the rotation of the shape model to evaluate the gravitational accelerations, which is computationally more expensive with respect to the simple rotation of a coordinate system, since in that case the rotation procedure should be applied at each integration step to any vertex of the model. Hence, in the rotating frame the gravitational field is not time dependent, and it can be computed only once in a region of interest around the body. Moreover, if the body is in a uniform principal rotation state, the time dependence is also eliminated from the dynamics, and the equations of motion are time invariant. In general, this is note the case for the real motion of celestial bodies under the effect of perturbations, but if a simplified dynamical behaviour is considered, then the rotating frame is even more convenient. Nevertheless, an inertial reference frame must be defined, because it is needed to take easily into account the presence of the Sun for the perturbative effects, and because it could be interesting and more intuitive to see how the trajectories evolve in the inertial space.

The most convenient choice for the body-fixed frame is obviously the same coordinate system that is used for the shape model; in this way, no transformation is necessary between the gravitational field and the dynamical model. So the rotating frame, B, is a right-handed 3D Cartesian reference with origin in the centre of mass of the body and basis vectors $\hat{\mathbf{x}}$, $\hat{\mathbf{y}}$ and $\hat{\mathbf{z}}$. They are aligned with the principal inertia directions associated with the body, so that $\hat{\mathbf{z}}$ is aligned with the direction of the maximum inertia axis. The triad is completed with $\hat{\mathbf{x}}$ and $\hat{\mathbf{y}}$ that are parallel to the axes associated with the minimum and the intermediate moments of inertia, respectively.

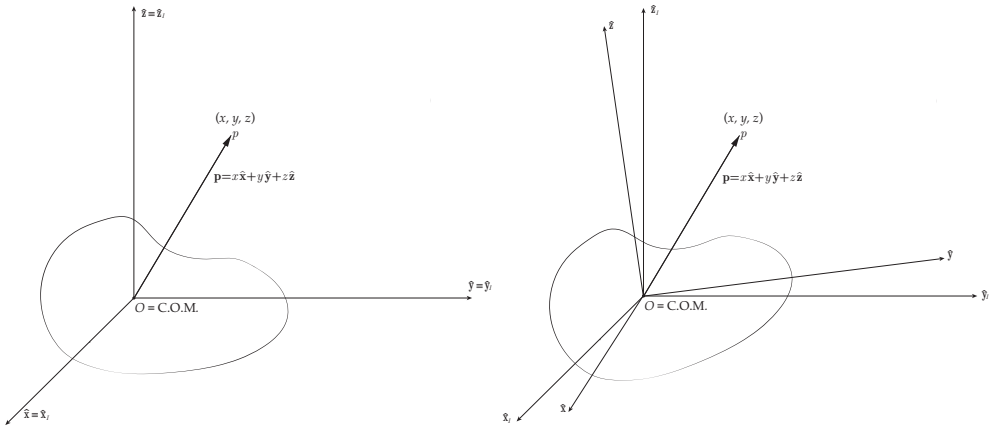

(a) $t = 0$ (b) $t > 0$

Figure 2.13: Inertial, I, and Rotating Body-Fixed, B, Reference Frames.

The inertial reference frame, I, is centred in the centre of mass of the main body and its basis vectors, $\hat{\mathbf{x}}_I$, $\hat{\mathbf{y}}_I$ and $\hat{\mathbf{z}}_I$, are aligned in order to coincide with those of the rotating coordinate system at $t = 0$. The Sun is rotating in this inertial frame that is fixed with respect to the centre of the body. Obviously, this is an assumption and the reference system is not really inertial, since it is moving with the celestial object in an orbit around the Sun. However, the orbital dynamics of the asteroid or the comet is not considered in this work, and the motion around the Sun is only necessary to compute the perturbations involving the Sun-Body direction. For this reason, the origin of I coincides with the centre of mass of the irregular object, and the Sun is moving on a circular "path" around the asteroid or the comet[4]. The motion of the Sun lies on the $x_I y_I-$plane, and $\hat{\mathbf{z}}_I$ is aligned with the normal to the orbital plane. Both the inertial and the body-fixed frames are illustrated in figure 2.13 at two different instants in time.

The position vector that locates the massless particle P at the field point (x, y, z) is $\mathbf{p}$. It can be expressed in the body-fixed reference frame as $\mathbf{p} = x\hat{\mathbf{x}} + y\hat{\mathbf{y}} + z\hat{\mathbf{z}}$. Obviously, this vector can also be expressed in the inertial reference frame by means of a transformation between the two coordinate systems.

In fact, any reference frame can be switched to another one with a proper conversion process. To define the relative orientation of the two frames at least three parameters are required and in this thesis the Euler angles are used to express the rotation from the frame I to the frame B.

[4]Galileo, I am really sorry.

It is convenient to use them since they are a minimal representation, i.e. no redundant parameters are used, and they have an evident physical interpretation: Euler angles represent a sequence of three elemental rotations about the reference axes. The respective rotation matrices can be combined, adopting the rule of consecutive rotations, into the direction cosine matrix that allows transforming the representation of a vector expressed in the inertial frame to the representation of the same vector in the rotating body-fixed reference system. So, the formal expression of a vector in B is obtained by multiplying a vector in I by the direction cosine matrix $\mathbf{A}$:

$$\mathbf{v}_B = \mathbf{A}\mathbf{v}_I. \tag{2.42}$$

The matrix $\mathbf{A}$ is orthogonal and therefore it can be said that:

$$\mathbf{A}^{-1} = \mathbf{A}^{\mathrm{T}}, \tag{2.43}$$

and from equation (2.42), the inverse rotation is expressed as:

$$\mathbf{v}_I = \mathbf{A}^{-1}\mathbf{v}_B = \mathbf{A}^{\mathrm{T}}\mathbf{v}_B = \mathbf{A}_I\mathbf{v}_B. \tag{2.44}$$

If the position vector $\mathbf{p}$ is considered, equation (2.44) can be written as:

$$\mathbf{p}_I = \mathbf{A}_I\mathbf{p}. \tag{2.45}$$

where $\mathbf{p}_I$ is the position of the massless particle expressed in the inertial reference frame. As a consequence, if the velocity and the acceleration of the massless particle in the inertial frame are needed, equation (2.45) has to be derived in time obtaining:

$$\dot{\mathbf{p}}_I = \dot{\mathbf{A}}_I\mathbf{p} + \mathbf{A}_I\dot{\mathbf{p}}, \tag{2.46}$$

and

$$\ddot{\mathbf{p}}_I = \ddot{\mathbf{A}}_I\mathbf{p} + 2\dot{\mathbf{A}}_I\dot{\mathbf{p}} + \mathbf{A}_I\ddot{\mathbf{p}}, \tag{2.47}$$

where the single dot represents time derivative and the double dot represents second time derivative.

Equations (2.45) to (2.47) provide useful relations that relate the rotating body-fixed frame with the inertial one.

2.4.3 Rotational Kinematics

The matrix $\mathbf{A}$ is obviously time-dependent since it is continuously changing as the rotational motion of the body evolves. For this reason, it is

important to define how the rotational parameters change with time, and it must be noted that kinematic equations of rotational motion are not as simple as those related with translational motion.

The time dependence of the rotation matrix can be related to the angular velocity of the primary expressed in the rotating body frame, $\boldsymbol{\omega}$, having:

$$\dot{\mathbf{A}} = f\left(\boldsymbol{\omega}\right) = f\left(\omega_x, \omega_y, \omega_z\right), \tag{2.48}$$

where ω_x, ω_y and ω_z are the components of the angular velocity, respectively, around the $\hat{\mathbf{x}}$, $\hat{\mathbf{y}}$ and $\hat{\mathbf{z}}$ axes. The explicit expression of equation (2.48) can be derived, as in [28, 56], obtaining:

$$\begin{aligned}\dot{\mathbf{A}} &= \lim_{\Delta t \to 0} \frac{\mathbf{A}(t+\Delta t) - \mathbf{A}(t)}{\Delta t} = \lim_{\Delta t \to 0} -\frac{\Delta t \left[\boldsymbol{\omega}\wedge\right] \mathbf{A}(t)}{\Delta t} \\ &= -\left[\boldsymbol{\omega}\wedge\right] \mathbf{A}(t),\end{aligned} \tag{2.49}$$

where $[\boldsymbol{\omega}\wedge]$ is the skew symmetric cross product matrix, defined by:

$$\left[\boldsymbol{\omega}\wedge\right] = \begin{bmatrix} 0 & -\omega_z & \omega_y \\ \omega_z & 0 & -\omega_x \\ -\omega_y & \omega_x & 0 \end{bmatrix}. \tag{2.50}$$

Knowing $\boldsymbol{\omega}$, equation (2.49) can be integrated in order to compute $\mathbf{A}$ at the next instant in time, but taking into account the numerical errors, $\mathbf{A}$ is not guaranteed to stay orthogonal. For this reason, it necessary to implement a numerical orthogonalization process that at each iteration step enforces the orthogonality of the rotation matrix.

For sure the Euler angles could also be used to propagate the rotational dynamics without the integration of the whole $\mathbf{A}$ matrix. There are some advantages, since they have fewer parameters and fewer constraints, but some singular conditions, which must be avoided, exist, and the entire integration process has to be carefully managed. On the other hand, the integration of equation (2.49) is straightforward and very simple to be implemented with the code that is developed in this work, for this reason, the direction cosine matrix is here used for rotational kinematics.

2.4.4 Equations of Motion

The equations of motion for the particle moving under the gravitational attraction of an irregularly-shaped body are derived from Newton's second law of motion: the acceleration of a point in a force field is

directly proportional to the vector sum of the forces in that point. This can be computed as the gradient of the gravitational potential, according to equation (2.1). The potential function is obtained with the enhanced gravitational modelling techniques that are employed in this thesis, and obviously, it depends on the specific approach that is adopted. However, for the present purpose, U is the potential function independently from the gravity model formulation.

Newton's law is valid only in an inertial reference frame, and so it can be expressed in the system I as:

$$\ddot{\mathbf{p}}_I = \nabla U(\mathbf{p}_I, t), \tag{2.51}$$

where the potential function is dependent on the position of the particle, and it is also time dependent because the primary is in a rotational motion with respect to I.

As explained in section 2.4.2, this time dependence can be eliminated if equation (2.51) is written in the rotating body-fixed frame, B. In order to correctly transform the previous equation, the basic kinematic equations must be correctly applied to expand the inertial acceleration in the rotating body-fixed frame, which is a non-inertial reference frame and therefore exhibit fictitious accelerations.

The kinematic equations that relate the inertial with the rotating frame can be expressed, applying the transport theorem, as:

$$\mathbf{v}_I = \dot{\mathbf{p}}_I = \dot{\mathbf{p}} + \boldsymbol{\omega} \times \mathbf{p}, \tag{2.52}$$

and

$$\mathbf{a}_I = \ddot{\mathbf{p}}_I = \ddot{\mathbf{p}} + 2\boldsymbol{\omega} \times \dot{\mathbf{p}} + \boldsymbol{\omega} \times (\boldsymbol{\omega} \times \mathbf{p}) + \dot{\boldsymbol{\omega}} \times \mathbf{p}, \tag{2.53}$$

where $\boldsymbol{\omega}$ is the angular velocity of the rotating body-fixed frame with respect to the inertial one.

In equation (2.53), the fictitious accelerations typical of a rotating reference system can be recognized, indeed the second term after the equality sign is the *Coriolis* acceleration, the third is the *centrifugal* acceleration and the last one is *Euler* acceleration. The first term after the equality sign is obviously the acceleration of the particle as measured in the rotating body-fixed frame. The centrifugal acceleration points always in the outward radial direction, the Coriolis acceleration is always perpendicular to the velocity vector and the Euler acceleration might be considered as a "tangential" acceleration due to a variation in the angular velocity of the reference frame's axes.

Now, substituting equation (2.53) in equation (2.51), the equations of motion of the particle, in the body-fixed coordinate system, is obtained as:

$$\ddot{\mathbf{p}} + 2\boldsymbol{\omega} \times \dot{\mathbf{p}} + \boldsymbol{\omega} \times (\boldsymbol{\omega} \times \mathbf{p}) + \dot{\boldsymbol{\omega}} \times \mathbf{p} = \nabla U(\mathbf{p}), \tag{2.54}$$

where now U is time invariant, and can be specialized according to the considered gravitational modelling technique. The gradient can be evaluated and the respective expressions are reported here for the convenience of the reader:

$$\nabla U^{Poly} = -G\sigma \sum_{e \in edges} \mathbb{E}_e \cdot \mathbf{r}_e \, L_e + G\sigma \sum_{f \in faces} \mathbb{F}_f \cdot \mathbf{r}_f \, \omega_f, \tag{2.55}$$

$$\nabla U^{Mascons} = -G \sum_{i=1}^{N_m} \frac{m_i}{r_i^3} \mathbf{r}_i. \tag{2.56}$$

All the quantities in the previous two equations have been defined in the related sections 2.2.2 and 2.2.3.

The velocity and the acceleration of the particle can be expressed in the rotating frame as:

$$\dot{\mathbf{p}} = \dot{x}\hat{\mathbf{x}} + \dot{y}\hat{\mathbf{y}} + \dot{z}\hat{\mathbf{z}}, \tag{2.57}$$

$$\ddot{\mathbf{p}} = \ddot{x}\hat{\mathbf{x}} + \ddot{y}\hat{\mathbf{y}} + \ddot{z}\hat{\mathbf{z}}. \tag{2.58}$$

In this way, inserting equations (2.57) and (2.58) in the vector differential equation (2.54), remembering that $\nabla U = [U_x, U_y, U_z]$, and carrying out some algebraic manipulations, the Cartesian scalar equations can be obtained. These are a system of three second order scalar differential equations of motion that can be numerically integrated.

The quantities $\boldsymbol{\omega}$ and $\dot{\boldsymbol{\omega}}$ in equation (2.54) are connected with the rotational dynamics of the main body and are related together by the rigid body motion equations. These are obtained extending the Newton's law of motion for point particle to rigid body motion. In fact, it is possible to write the fundamental Euler's second law in an inertial reference as:

$$\frac{\mathrm{d}\mathbf{h}_I}{\mathrm{d}t} = \dot{\mathbf{h}}_I = \mathbf{m}_I, \tag{2.59}$$

where $\mathbf{h}_I$ is the angular momentum in I, and $\mathbf{m}_I$ is the net external perturbing torque with respect to the centre of mass in I. Anyhow, as done before with the equations of motion of a particle moving under the gravitational attraction of an irregularly-shaped body, it is possible to transform the previous equation into the body-fixed frame. Using the

correspondent of equation (2.52) for the angular momentum, and evaluating the external perturbing torques in the rotating reference system, equation (2.59) becomes:

$$\dot{\mathbf{h}} + \boldsymbol{\omega} \times \mathbf{h} = \mathbf{m}, \tag{2.60}$$

which is expressed in B.

In the principal inertia reference frame the angular momentum can be expressed as:

$$\mathbf{h} = \mathbf{I}\boldsymbol{\omega} = I_x\omega_x + I_y\omega_y + I_z\omega_z, \tag{2.61}$$

since the inertia tensor, **I**, in principal inertia axes is:

$$\mathbf{I} = \begin{bmatrix} I_x & 0 & 0 \\ 0 & I_y & 0 \\ 0 & 0 & I_z \end{bmatrix}, \tag{2.62}$$

where I_x, I_y and I_z are the principal moments of inertia with respect to the axes of the body-fixed principal reference frame. So, the equation (2.60) becomes:

$$\mathbf{I}\dot{\boldsymbol{\omega}} + \boldsymbol{\omega} \times \mathbf{I}\boldsymbol{\omega} = \mathbf{m}. \tag{2.63}$$

Even in this case, recognizing that $\boldsymbol{\omega} = [\omega_x, \omega_y, \omega_z]$ and $\mathbf{m} = [\mathrm{m}_x, \mathrm{m}_y, \mathrm{m}_z]$, it is possible to obtain the Cartesian scalar form of equation (2.60), for numerical integration, with few algebraic manipulations. The result is composed by a set of three first order scalar differential equations.

The complete dynamical and kinematic model is now completely defined and it is important to note that the equations of motion are coupled, and they must be solved together to correctly propagate the evolution of the particle-main body system. Hence, the full model is composed by a (3×3) first order matrix differential equation (2.49), a (3×1) second order vector differential equation (2.54), and a (3×1) first order vector differential equation (2.63). Then, in order to facilitate the numerical investigation, a system of only first order differential equations is preferred, and for this reason, the (3×1) second order vector differential equation is reduced in two different (3×1) first order vector differential equations. Moreover, the integration of vector and matrix equations is easier if they are expressed in a scalar form, which in this case is composed by 18 different first order scalar differential equations, expressed in the Cartesian body-fixed reference frame.

The state vector of the whole model is:

$$\boldsymbol{V} = [A_{11},\, A_{12},\, \ldots,\, A_{33},\, \omega_x,\, \omega_y,\, \omega_z,\, x,\, y,\, z,\, \dot{x},\, \dot{y},\, \dot{z}]^{\mathrm{T}}, \tag{2.64}$$

where A_{11}, A_{12}, $\ldots$, A_{33} are the 9 components of the rotation matrix $\mathbf{A}$. The entire system of first order scalar differential equations can be written as:

$$\dot{\boldsymbol{V}} = \boldsymbol{f}(\boldsymbol{V}). \tag{2.65}$$

Here, $\boldsymbol{f}(\boldsymbol{V})$, is the vector containing all the scalar differential equations. To integrate the system, a set of 18 scalar initial conditions must be provided, through a known state vector, $\boldsymbol{V}_0$, evaluated at $t = 0$.

The set of differential equations is integrated using MATLAB® and a variable order method differential equations solver, with medium to high order of accuracy. The problem is computational intensive because several operations must be repeated at each step of integration, thus, to reduce the time to run a simulation, the algorithms make an extensive use of parallel computing techniques on multi-processor workstations.

2.4.5 Integral of Motion

The equations of motion of the particle can be further analysed considering possible conserved quantities, or integrals of motion. The scalar quantity, J, can be defined as:

$$J \overset{\text{def}}{=} \frac{1}{2}\,\dot{\mathbf{p}} \cdot \dot{\mathbf{p}} - \frac{1}{2}\,(\boldsymbol{\omega} \times \mathbf{p}) \cdot (\boldsymbol{\omega} \times \mathbf{p}) - U(\mathbf{p}), \tag{2.66}$$

where all the quantities have been previously defined. Then, taking the time derivative of J with respect to the body-fixed frame, and rearranging the dot product of $\dot{\mathbf{p}}$ with equation (2.54), is possible to write:

$$\dot{J} = \dot{\boldsymbol{\omega}} \cdot (\mathbf{v}_I \times \mathbf{p})\,, \tag{2.67}$$

where $\mathbf{v}_I$ has been defined in equation (2.52). If the main body is in uniform principal axis rotation, i.e. $\dot{\boldsymbol{\omega}} = 0$, then J is conserved and will be referred to as Jacobi integral of motion. Hence, only if the body is uniformly rotating an integral of motion exist, and as mentioned in section 2.4.2, the equations of motion in B are fully time invariant.

Assuming, in the meanwhile, a uniformly principal axis rotating asteroid or comet, J is constant for all the resultant motion of the particle, and for a given set of initial conditions on particle position and velocity. Different initial conditions can obviously lead to the same constant value

of the Jacobi integral, and consequently it is convenient to define a Jacobi constant, C, as:

$$C \stackrel{\text{def}}{=} -J(\mathbf{p}, \dot{\mathbf{p}}), \tag{2.68}$$

where the dependence of J from position and velocity of the particle in the body-fixed frame has been explicitly declared. Under the current assumptions of constant angular velocity, $\mathbf{\Omega} = [\Omega_x, \Omega_y, \Omega_z]$, the Jacobi constant expression can be derived from equation (2.66):

$$C = V(\mathbf{p}) - T(\dot{\mathbf{p}}) = U(\mathbf{p}) + \frac{1}{2}\left(\mathbf{\Omega} \times \mathbf{p}\right) \cdot \left(\mathbf{\Omega} \times \mathbf{p}\right) - \frac{1}{2}T(\dot{\mathbf{p}}). \tag{2.69}$$

In the previous equation, $V(\mathbf{p}) = V(x, y, z)$ is the pseudo-potential function:

$$V(x, y, z) = U(x, y, z) + \frac{1}{2}\left(\mathbf{\Omega} \times [x, y, z]\right) \cdot \left(\mathbf{\Omega} \times [x, y, z]\right), \tag{2.70}$$

and $T(\dot{\mathbf{p}}) = T(\dot{x}, \dot{y}, \dot{z})$ is the kinetic energy of the particle with respect to the rotating main body:

$$T(\dot{x}, \dot{y}, \dot{z}) = \frac{1}{2}\left(\dot{x}^2 + \dot{y}^2 + \dot{z}^2\right). \tag{2.71}$$

It is worthwhile to note that the Jacobi constant is a function of the kinetic energy and the pseudo-potential, and so it is an energy-like quantity, and because of the opposite sign, if the energy increases the Jacobi constant decreases.

Even in the simplest case of uniformly rotating body, the only integral of motion that exists, J, is not enough to have an analytical solution. However, it can offer interesting hints on the dynamical behaviour around the principal body, which are useful for numerical investigation. In fact, the Jacobi integral helps to illustrate and understand an important concept that is related with the presented dynamical environment.

Considering equation (2.69), it can be re-arranged to highlight a relation between the kinetic energy of the particle and the Jacobi constant:

$$T(\dot{\mathbf{p}}) = V(\mathbf{p}) - C \geq 0, \tag{2.72}$$

where the inequality sign comes from the definition of kinetic energy that must be non-negative in order to maintain a physical meaning. This inequality suggests possible restrictions on the position of the particle, since, for a given C, the motion is bounded in a region where the position,

$\mathbf{p}$, allows $V(\mathbf{p})$ to be greater than the Jacobi constant, C. Note that $V(\mathbf{p}) \geq 0$ for any $\mathbf{p}$, and so, if $C < 0$, there are no constraints on where the particle may be found. On the contrary, if $C > 0$, the trajectories of the particle can evolve only in certain portion of space.

The limit condition is generated by a zero relative velocity, and thus, a zero kinetic energy, $T(\dot{\mathbf{p}}) = 0$. In this case equation (2.72) becomes:

$$V(\mathbf{p}) = C, \tag{2.73}$$

and the infinite solutions of the previous describe a surface in three-dimensional space, which constraints the possible motion of the particle. When the constant of motion is varying in time, e.g. in a non-principal rotation state of the main body, the three-dimensional surface evolves in time accordingly. Therefore, when the Jacobi integral is not conserved, the previous considerations are still valid, but they are limited to an instantaneous authority, without uniformity through all the motion propagation. These surfaces are denoted as the Zero Velocity Surfaces (ZVS) and separate two distinct regions of space: the *forbidden* region, when $V(\mathbf{p}) < C$, and the *admissible* one, where $V(\mathbf{p}) > C$ and the modulus of the velocity is real. The projection of a Zero Velocity Surface on a plane is called Zero Velocity Curve (ZVC).

2.4.6 Equilibrium Solutions

Another useful concept to have some insights on the dynamical properties of the dynamics of a particle around an irregularly-shaped body is the one related with the equilibrium solutions of the equations of motion, i.e. points in the physical space where an object is subject to zero velocity and zero acceleration. There, it remains at rest in time with respect to the rotating frame. Since the equilibrium solutions require that the particle has zero relative velocity, they are particular solutions of the Zero Velocity Surfaces for certain values of the Jacobi Constant.

In this dynamical framework, the number of equilibrium solutions is not pre-determined, and there is no analytical expression for their locations. Hence, a numerical algorithm has been implemented to find their positions, and it will be described afterwards. It is important to remember that these equilibrium solutions exist in general only if the Jacobi constant is conserved, while in the case of varying angular velocity they can be only defined at each instant of time, and thus, no real equilibrium position can be found in the physical space.

In the case of $\boldsymbol{\omega} = \boldsymbol{\Omega}$, it can be easily proved that equation (2.54) can be expressed as a function of the pseudo potential function $V(\mathbf{p})$:

$$\ddot{\mathbf{p}} + 2\boldsymbol{\Omega} \times \dot{\mathbf{p}} = \nabla V(\mathbf{p}). \tag{2.74}$$

Then, since the equilibrium condition implies $\ddot{\mathbf{p}} = 0$, and $\dot{\mathbf{p}} = 0$, the locations of the equilibrium points can be calculated by equating the gradient of the pseudo-potential, $V(\mathbf{p})$, to zero, that is:

$$\frac{\partial V(\mathbf{p})}{\partial x} = \frac{\partial V(\mathbf{p})}{\partial y} = \frac{\partial V(\mathbf{p})}{\partial z} = 0. \tag{2.75}$$

The equilibrium points represent the extrema of the pseudo-potential function, where a balance between the forces in the rotating frame is guaranteed.

2.4.7 Dynamical Properties

The simulations that are analysed in this thesis make use of different set of data about the dynamical status of the considered Solar System's bodies.

These properties are used as initial conditions to propagate the dynamics of the particle-irregular body system, and they are grouped in the state vector $\boldsymbol{V}_0$, evaluated at $t = 0$. However, in this vector, some of them are arbitrarily chosen: the initial conditions of the particle, x_0, y_0, z_0, $\dot{x}_0$, $\dot{y}_0$, $\dot{z}_0$, and the initial Euler angles, ϕ_0, θ_0 and ψ_0. The formers are immediately used to compute the initial direction cosine matrix, $\mathbf{A}_0$, between the inertial and the body-fixed reference frame, since its components, $A_{11_0}, A_{12_0}, \ldots, A_{33_0}$, are used in the initial state vector, $\boldsymbol{V}_0$. So, considering that the two reference systems are assumed to coincide at the initial time, ϕ_0, θ_0 and ψ_0 are all equal to zero and $\mathbf{A}_0$ is equal to the 3×3 identity matrix, $\mathbb{I}^{3\times3}$. The initial conditions of the particle are selected in order to obtain insightful simulations, but there is no particular reason, or relation with the real world, to justify the choice of one particular set rather than another one.

On the contrary, the real dynamical properties of the main body are used as initial conditions for ω_x, ω_y and ω_z. Sometimes, these values are modified with respect to the real one for particular reasons that will be addressed in the relevant sections. Anyway, these numbers are often just slightly perturbed with respect to the actual ones. The sources of information are more or less the same that have been used to gather the inertia and shape model properties. The available data about the

Table 2.5: Rotational state of reference irregular bodies.

		$\|\boldsymbol{\omega}\|$ $[\mathrm{rad\,s^{-1}}]$	$\mathrm{T}_{2\pi}$ [h]
67P	C-G [12]	1.41×10^{-4}	12.40
216	Kleopatra [57]	3.24×10^{-4}	5.39
4179	Toutatis [41]	2.12×10^{-5}	82.33
433	Eros [30]	3.31×10^{-4}	5.27
1580	Betulia [27]	2.84×10^{-4}	6.14

magnitude of the angular velocity vector and the rotation period are listed, with their respective sources, in table 2.5.

The information about the orientation of the spin vector is more delicate, and sometimes, less accurate. Moreover, the rotational motion of the object can determine the variation in time of the spin axis, and therefore, an arbitrary choice is occasionally required for the data that are employed as initial conditions in each single simulation. These will be defined together with the presentation of the analysed situation. It is worth noting that the spin axis of a real asteroid can undergo chaotic variations due to the complex dynamical evolution of the bodies, and to the perturbative effects [22]. Thus, the use of a specified initial condition is not fundamental, since the actual rotation state could be different from the one described in the used references.

To complete the description of the initial state of the dynamical model, the position of the Sun must be specified in the inertial reference system. The assumption is that the Sun at $t = 0$ is located along the negative direction of the $\hat{\mathbf{x}}_I$, in a way that the Sun-Body direction is initially parallel to the x_I-axis. The evolution of the position of the Sun, in the I frame, has been already described in section 2.4.2, and now, the radii and the periods of the assumed circular orbit are listed in table 2.6, according to the JPL Solar System Dynamics data service[5].

2.5 Perturbations

The model described in this thesis includes also the relevant perturbations for the rotational dynamics of the analysed celestial bodies. It is important to remember that these perturbative effects act only on the rotational motion of the main body, according to the made assumptions,

[5] http://ssd.jpl.nasa.gov

Table 2.6: Radius of the orbit of reference irregular bodies.

		R_S [km]	R_S [AU]	T_S [y]
67P	C-G	5.18×10^{11}	3.46	6.45
216	Kleopatra	4.18×10^{11}	2.79	4.67
4179	Toutatis	3.78×10^{11}	2.53	4.02
433	Eros	2.18×10^{11}	1.46	1.76
1580	Betulia	3.29×10^{11}	2.20	3.26

and therefore, the dynamics of the particle is not directly influenced by the external disturbing forces. Nevertheless, since the equations of motion, (2.54) and (2.63), are coupled, the perturbations influence the dynamical evolution of the massless particle through the effects related with the rotational dynamics of the primary.

The perturbations that are relevant to the considered case, and that will be presented hereafter are: the gravity gradient due to the presence of a third body, the Sun, the Solar Radiation Pressure, the YORP effect and the internal dissipation of energy. Their effects are computed at each integration step, they are combined together and inserted in the rotational dynamics equation through the term representing the external perturbing torque, $\mathbf{m}$, computed in the rotating body-fixed frame.

2.5.1 Third Body Gravitational Effect

The motion of the particle-irregular body system is evolving under the gravitational influence of the Sun, which is a third external body with respect to the focus of this analysis. The gravitational effect of the Sun is not uniform, and since the main body is not symmetric, it is subject to a gravity gradient torque.

To explain this concept it is fundamental to consider any differential mass element of the primary body that is under the gravitational attraction of the Sun. Defining $\boldsymbol{\rho}$ as the distance of each differential mass element, $\mathrm{d}M$, with respect to the centre of mass of the body, it is possible to express the differential torque as:

$$\mathrm{d}\mathbf{m}_{GG} = -\boldsymbol{\rho} \times \frac{G\,\mathrm{d}M M_S}{\|\boldsymbol{R}_S + \boldsymbol{\rho}\|^3} \left(\boldsymbol{R}_S + \boldsymbol{\rho}\right), \tag{2.76}$$

where $\boldsymbol{\rho}$ is much smaller than the Sun-Body vector $\boldsymbol{R}_S$, and it can be considered as a perturbation. The previous equations can be integrated

all over the mass of the body, and $\|\boldsymbol{R}_S + \boldsymbol{\rho}\|^3$ can be approximated with a series expansion. After some manipulations, the torque due to the Sun gravity gradient can be expressed as:

$$\mathbf{m}_{GG} = \frac{3GM_S}{R_S^5} \int_M (\boldsymbol{\rho} \cdot \boldsymbol{R}_S)\ (\boldsymbol{\rho} \times \boldsymbol{R}_S)\, \mathrm{d}M. \tag{2.77}$$

In order to evaluate the effect of the torque on the main body dynamics, this has to be expressed in the body-fixed principal reference frame and inserted in the Euler's rotational equations. So, equation (2.77) becomes:

$$\begin{aligned} \mathbf{m}_{GG} &= \frac{3GM_S}{R_S^3} \int_M \begin{pmatrix} (y_M^2 - z_M^2)c_2c_3 \\ (z_M^2 - x_M^2)c_1c_3 \\ (x_M^2 - y_M^2)c_1c_2 \end{pmatrix} \mathrm{d}M \\ &= \frac{3GM_S}{R_S^3} \begin{pmatrix} (I_z - I_y)c_2c_3 \\ (I_x - I_z)c_1c_3 \\ (I_y - I_x)c_1c_2 \end{pmatrix}, \end{aligned} \tag{2.78}$$

where c_1, c_2 and c_3 are the direction cosines of the Sun-Body direction in principal inertia axes, and x_M, y_M and z_M are the coordinates of the differential mass elements in the same reference.

Looking at equation (2.78), it is evident that if one principal inertia axis is aligned with the Sun-Body direction, the torque is zero because only one of the direction cosines is different from zero. Moreover, this torque depends on the relative orientation of the body with respect to the Sun and thus, if averaged over one full rotation of the asteroid or comet on its axis, and over one full revolution as it orbits the Sun, the contribution is null.

When the perturbative effect due to the presence of the Sun is computed, the body is assumed infinitely rigid and no tidal deformation is taken into account. Therefore, the shape of the asteroid or the comet is preserved and the tidal torque is not considered.

2.5.2 Solar Radiation Pressure

The electromagnetic radiation emitted by the Sun interacts with the bodies that are present in the Solar System. The radiation can interact with a surface by reflection or absorption, and since it carries momentum and energy, this interaction generates a pressure that perturbs the rotational motion of a body in space.

Table 2.7: Radiation Coefficients.

c_a $[-]$	c_d $[-]$	c_s $[-]$
0.9	0.075	0.025

The average pressure due to radiation can be computed using:

$$P_S = \frac{F_S}{c}, \tag{2.79}$$

where $c = 299\,792\,458\,\mathrm{m/s}$ is the speed of light, and F_S is the flux density of solar radiation at the distance of the body from the Sun. It can be computed with an inverse square law, knowing the flux of solar radiation at a certain location in Space. For example, at the Sun-Earth distance, $F_S = 1360\,\mathrm{w/m^2}$.

In order to evaluate the force acting on a surface, it is important to model the interaction of the radiation with the body. In fact, the incident radiation coming from the Sun can be absorbed, specularly reflected and reflected with diffusion. The fraction of radiation associated with each one of these interaction modes is expressed by a coefficient of absorption, c_a, diffuse reflection, c_d, and specular reflection, c_s. The coefficients must sum to unity, $c_a + c_d + c_s = 1$, and in this work they are assumed to have the values reported in table 2.7, according to the data for typical celestial bodies present in the JPL Solar System Dynamics data service.

The force that is generated by the solar radiation pressure interaction can be computed for each triangular face of the polyhedron model, and then the global force can be found summing all over the single contributions. In this way, it is possible to use the expression for the radiation pressure on a flat surface, no approximation is made in addition to the one of discretizing the real body with a polyhedron, and the self-shadowing effect can be taken into account with simple geometrical considerations.

For the i-th body planar surface of area A_i, the solar radiation force can be expressed as:

$$\mathbf{f}_{SRP_i} = -A_i P_s \left[(1 - c_s)\hat{\mathbf{s}} + 2\left(c_s \cos(\alpha_i) + \frac{1}{3} c_d \right) \hat{\mathbf{n}}_i \right] \cos(\alpha_i)_{Sh}, \tag{2.80}$$

where $\hat{\mathbf{s}}$ and $\hat{\mathbf{n}}_i$ are, respectively, the Body-Sun direction and the surface normal direction in the body-fixed frame. The angle α is the angle between the Body-Sun and the normal to the surface directions, and $\cos(\alpha)$

can only assume positive value since, if $\hat{\mathbf{n}}_i \cdot \hat{\mathbf{s}}$ is negative, the surface is in shadow and is not illuminated by the Sun. This can be mathematically expressed with $\cos(\alpha_i)_{Sh} = \max(0, \cos(\alpha_i))$. The diffuse reflection is assumed to be Lambertian, i.e. the intensity of the reflected light in any direction is proportional to the cosine of the angle between the reflection direction and the normal, determining a Lambertian scattering coefficient of the surface, ideally equal to $2/3$. The self-shadowing is considered, and the algorithm to determine if a face is in the shadow of another one will be described in section 4.1. Equation (2.80) is obtained assuming that the absorbed radiation acts in the Body-Sun direction, the specularly reflected radiation acts in the normal to the surface direction and the diffuse radiation acts in both directions.

The whole solar radiation torque can be computed, for a N faces polyhedron, as:

$$\mathbf{m}_{SRP} = \sum_{i=1}^{N} \boldsymbol{\rho}_i \times \mathbf{f}_{SRP_i}, \tag{2.81}$$

where $\boldsymbol{\rho}_i$ is position of each triangular face's centre with respect to the centre of mass of the body.

2.5.3 YORP Effect

The Yarkovsky–O'Keefe–Radzievskii–Paddack (YORP) effect is related with the thermal radiation emission from the surface of a body. It is the rotational extension of the Yarkovsky effect, discovered by the civil engineer Ivan Osipovich Yarkovsky (1844–1902) at the beginning of the 20$^{\text{th}}$ century. Yarkovsky noted that the diurnal heating of a rotating space object would generate a tiny force that could lead to large secular effects in its orbit.

In the YORP extension, this effect can produce torques that affect the spin rate and spin axis orientation of small irregular celestial bodies. The amount of torque acting on an object is small, since the amount of momentum carried by photons is limited. Nevertheless, the YORP torque is secular, so that after a long period the body's rotation state can be noticeably different. There are several analogies with the solar radiation pressure and they are separately addressed because the YORP effect deals with the radiation emitted by the body, while the solar radiation pressure deals with the incoming radiation from the Sun, which is absorbed or reflected. Obviously, the thermal balance of the body couples these contributions, and therefore, their differences are more formal than conceptual. As explained in the related references [4, 39],

the body must have a certain amount of "windmill" asymmetry in its shape to be influenced by the YORP effect.

In this model, it is assumed that the body surface is Lambertian, i.e. the reaction force from photons departing from any given surface elements is normal to it. In this way, the differential YORP force acts on the normal to the surface direction, as the specularly reflected solar radiation pressure. This characteristic determines the secularity of the YORP torque. On the contrary, the radiation forces along the Body-Sun direction, e.g. absorbed SRP, average to zero, because they depend on the projection that the body presents to the Sun: these solar torques cancel over one full rotation and one full revolution as the Sun sees the projection in all directions.

The model that is used in this thesis assumes zero thermal conductivity for the surface of the body [8], which means that the thermal emission occurs immediately after the incoming radiation has hit the surface. Similarly to what has been done for the solar radiation pressure, the surface of the body is discretized with the N polyhedral flat triangular faces and the self-shadowing is taken into account.

With these assumptions, the torque due to the YORP effect can be expressed as:

$$\mathbf{m}_{YORP} = \frac{2}{3}(1 - c_r)P_S \sum_{i=1}^{N} A_i(\hat{\mathbf{n}}_1 \times \boldsymbol{\rho}_i)\cos(\alpha_i)_{Sh}, \tag{2.82}$$

where $c_r = c_d + c_s$ is the albedo of the body, and all the other quantities have been defined in the solar radiation pressure section 2.5.2. With the values that are used in this work, the albedo of the body is $\sim 10\%$, which is a reasonable value since the small Solar System objects tend to be very dark.

2.5.4 Dissipation of Energy

Energy losses in an anelastic material occur when the internal stresses are time-variant; hence, even freely rotating bodies in space lose energy because internal stresses are associated with the accelerations caused by nutation. As a consequence, internal dissipation of energy is associated with non-principal rotation states, since in this case the rotational acceleration is time-varying in the body-fixed frame. In presence of internal energy losses, the angular momentum vector of the body tends to align with its maximum inertia axis, and even though this effect is extremely

small, it can influence the rotational state of a small wobbling celestial object, if a long time scale is taken into account.

This effect can be modelled with an additional perturbing torque in the equations of motion. In the case of rotation axis closer to the maximum inertia axis, the torque due to the dissipation of energy is expressed as:

$$\mathbf{m}_D = \mp \frac{\sigma a_{eq}^2}{kQI_z} \|\mathbf{h}\|^3 \sin(\gamma)(b_0 + b_2 \cos^2(\gamma))\mathbf{h} \times \left(\frac{\mathbf{h} \times \hat{\mathbf{z}}}{\|\mathbf{h}\| \sin(\gamma)} \right), \quad (2.83)$$

where σ is the bulk density, a_{eq} the averaged equatorial radius, k the rigidity of the material, Q the quality factor, I_z is the maximum moment of inertia and γ is the angle between the angular momentum vector, $\mathbf{h}$, and the maximum inertia direction, $\hat{\mathbf{z}}$. The minus sign is for a rotation axis closer to $\hat{\mathbf{z}}^+$ direction, while the plus is for $\hat{\mathbf{z}}^-$.

Similarly, for the rotation axis closer to the minimum inertia direction, equation (2.83) becomes:

$$\mathbf{m}_D = \pm \frac{\sigma a_{eq}^2}{kQI_x} \|\mathbf{h}\|^3 \sin(\gamma)(b_0 + b_2 \cos^2(\gamma))\mathbf{h} \times \left(\frac{\mathbf{h} \times \hat{\mathbf{x}}}{\|\mathbf{h}\| \sin(\gamma)} \right), \quad (2.84)$$

where now γ is the angle between the angular momentum vector and the minimum inertia direction $\hat{\mathbf{x}}$, with moment of inertia I_x. In this case, the plus sign must be used when the rotation axis is closer to $\hat{\mathbf{x}}^+$, and the minus when it is closer to $\hat{\mathbf{x}}^-$.

In both equations the coefficients b_0 and b_2 are known constants, expressed by [53] as:

$$b0 = \frac{325 + 760\,\upsilon^2 + 608\,\upsilon^4 + 320\,\upsilon^6}{7(1+\upsilon^2)^4\,(13+20\upsilon^2)\,(15+10\upsilon^2+8\upsilon^4)} \quad (2.85a)$$

$$b2 = \frac{-325 - 760\,\upsilon^2 + 952\,\upsilon^4 + 2820\,\upsilon^6 + 2232\,\upsilon^8 + 1120\,\upsilon^{10}}{7(1+\upsilon^2)^4\,(13+20\upsilon^2)\,(15+10\upsilon^2+8\upsilon^4)}, \quad (2.85b)$$

where υ is the geometric flattening of the spheroid. The value of the physical parameter kQ is, according to [48], $kQ = 5 \times 10^{11}\,\mathrm{kg\,m^{-1}\,s^{-2}}$.

The dissipation of energy involves the angular momentum magnitude as an important parameter. Indeed, if $\mathbf{h}$ is small, the effect of the dissipation is small, and there is a small perturbative effect. In general, the energy loss phenomena is less important than the other perturbative effects and thus, the non-principal axis state can be an asymptotic state, even if this contribution is taken into account. On the contrary, with a

large angular momentum, the dissipation of energy could dominate the other perturbative effects.

At this point, all the considered perturbative phenomena have ben defined, and it is possible to compute the net toque due to perturbations:

$$\mathbf{m} = \mathbf{m}_{GG} + \mathbf{m}_{SRP} + \mathbf{m}_{YORP} + \mathbf{m}_{D}. \tag{2.86}$$

The previous can be inserted in equation (2.63) and the dynamical model is thus completed.

Chapter 3

Gravity Field Models

An irregularly-shaped body influences the surrounding space according to the same Newton's law that is valid for any massive body. Notwithstanding, its irregular shape is reflected in the generated gravitational field, which is not spherically symmetric like the one produced by a centrobaric body. This characteristic is probably the one that influences most the dynamical environment in the vicinity of Solar System's smaller bodies, in fact, the orbits that exist in these situations are extremely different from the Keplerian ones.

In this chapter the gravitational influence of the selected reference celestial objects are discussed and analysed. Moreover, the different enhanced modelling techniques are compared in order to illustrate and examine their advantages and disadvantages. Furthermore, the optimized version of the mascons approach is presented and compared with the standard technique.

The gravitational field around an irregular shape body can be computed with different levels of accuracy, according to the fidelity of the modelling technique that is used. One of the main problems in evaluating the exact field is the required computational time, which could be acceptable on the Earth with a multi-processor computer, but it is not tolerable if the computations have to be performed with the on-board computer of a space probe that is flying around an asteroid or a comet. For this reason, it is necessary to study and analyse the so-called Lo-Fi models, which are less accurate but they do not require a high computational burden. The results of the aforementioned investigation are shown and discussed in this chapter.

3.1 Gravitational Influence of Selected Objects

The bodies that are analysed in this research work are representative of different classes of shape for real celestial bodies. In particular, the comet Churyumov-Gerasimenko is representative for bodies with two relevant bulges, the asteroid Kleopatra for objects that have a dog-bone shape, Toutatis and Eros represents those bodies that have one dimension longer than the other two, and Betulia characterize the asteroids that are more similar to a usual spherical shape. These characteristics are evident also in the resulting gravitational field that is here computed with the polyhedron or the mascons approach.

The field is computed in a 3D grid of $50 \times 50 \times 50$ points along the axes of the body-fixed reference frame. The dimensions of the analysed space are relative to the selected body, indeed the grid is 5 times the dimension of the body in each coordinate direction.

However, the visualization of the relevant quantities is more insightful with a 2D projection onto one of the coordinate planes. For this reason, the use of these projections is very frequent in this thesis, and the associated plane will be specified from time to time.

3.1.1 67P Churyumov-Gerasimenko

The comet 67P Churyumov-Gerasimenko has an interesting shape composed by two lobes: the large one has dimensions $4.10 \times 3.30 \times 1.80\mathrm{km}$ and the small $2.60 \times 2.30 \times 1.80\mathrm{km}$. This two-masses geometry is very useful for the purposes of this work, since it can be compared with a simplified two mascons model. This could be exploited to describe the dynamics around the comet with the techniques typically available in the restricted three-body problem.

The model available for this body is highly detailed thanks to the European Space Agency's Rosetta mission. In fact, the Rosetta mission was launched on 2 March 2004, then rendezvoused and entered in a close orbit with the comet on 10 September 2014. The cameras on-board of this spacecraft captured several images from a reduced distance, and consequently the available data are numerous and accurate. The obtained shape model is surprisingly irregular, and according to the first hypothesis, it could be the result of a contact binary formed by low-speed accretion between two separate objects, or the consequence of uneven erosion due to ice sublimating from its surface during previous Sun flybys. This body has relatively small size and shows to have a low

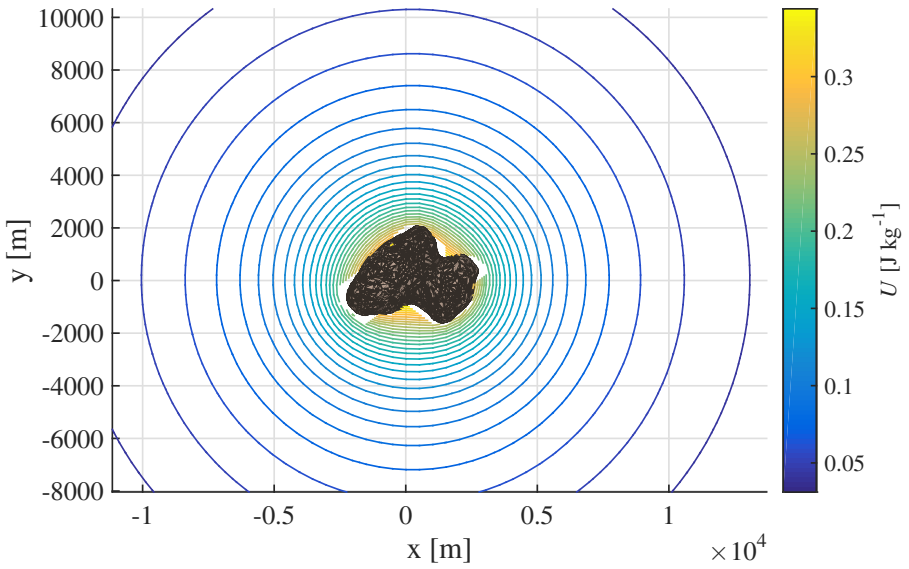

(a) Gravitational Potential, U.

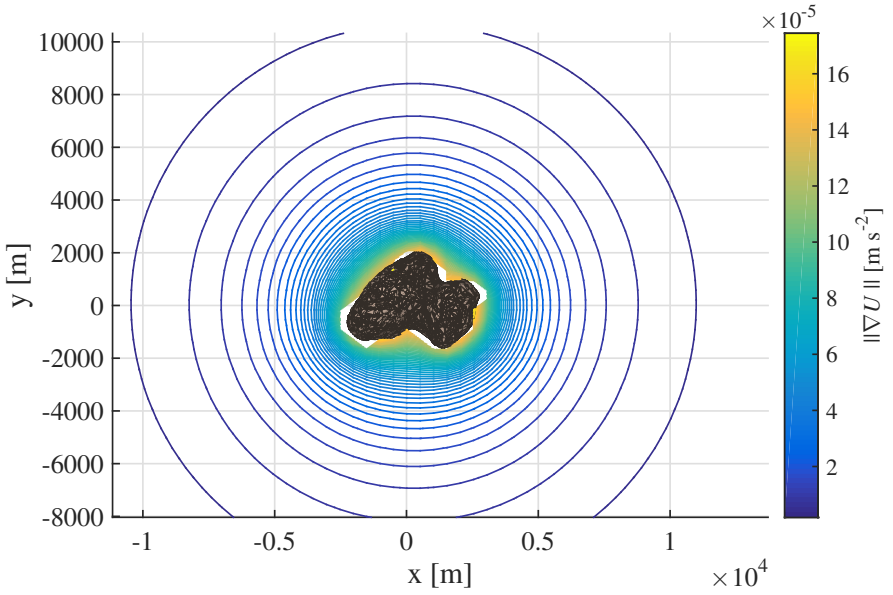

(b) Gravitational Attraction, $\|\nabla U\|$.

Figure 3.1: 67P Churyumov-Gerasimenko Gravity Field with $\sim 10^4$ faces Polyhedron Model.

density, $\sim 400\,\mathrm{kg/m^3}$, and a high level of porosity, $\sim 70 - 80\%$; therefore, a limited gravitational attraction is expected.

In figure 3.1, the potential and the gravitational attraction of the comet 67P are shown. In these images the quantities are projected onto

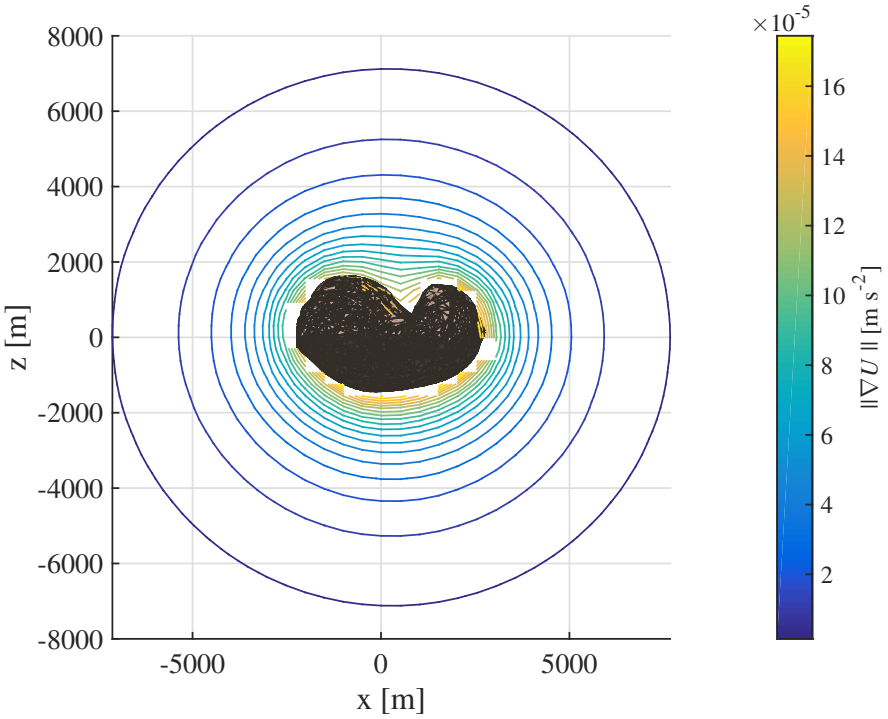

Figure 3.2: 67P Gravitational Attraction, $\|\nabla U\|$, on $xz-$plane.

the $xy-$plane of the body-fixed reference frame. This 2D view has been chosen because it shows the two characteristic bulges of the objects and it is the most significant in this case. The first thing that can be noted is the irregularities of the field close to the surface of the body, and obviously, it reflects the actual shape of the object. Then, both the potential and the gravitational attraction tend to be more regular as the field point moves away from the main attractor. This is reasonable because, if the distance from the body increases, its shape becomes negligible and the field approaches the one generated by a point particle. However, in figures 3.1a and 3.1b the field is still elongated at the borders of the grid. The resulting elongation is correctly oriented, with the x axis that is longer than the y one, in agreement with the shape of the body.

The gravitational acceleration, even close to the surface, is confirmed to be particularly low, with a maximum value equal to $a_{max} = 1.74 \times 10^{-4}\,\mathrm{m\,s^{-2}}$. In practice the attraction on the comet 67P Churyumov-Gerasimenko is more than a hundred thousand times weaker than on Earth.

The same plot can be repeated on different planes in order to understand the field evolution, with a three-dimensional point of view. In fact,

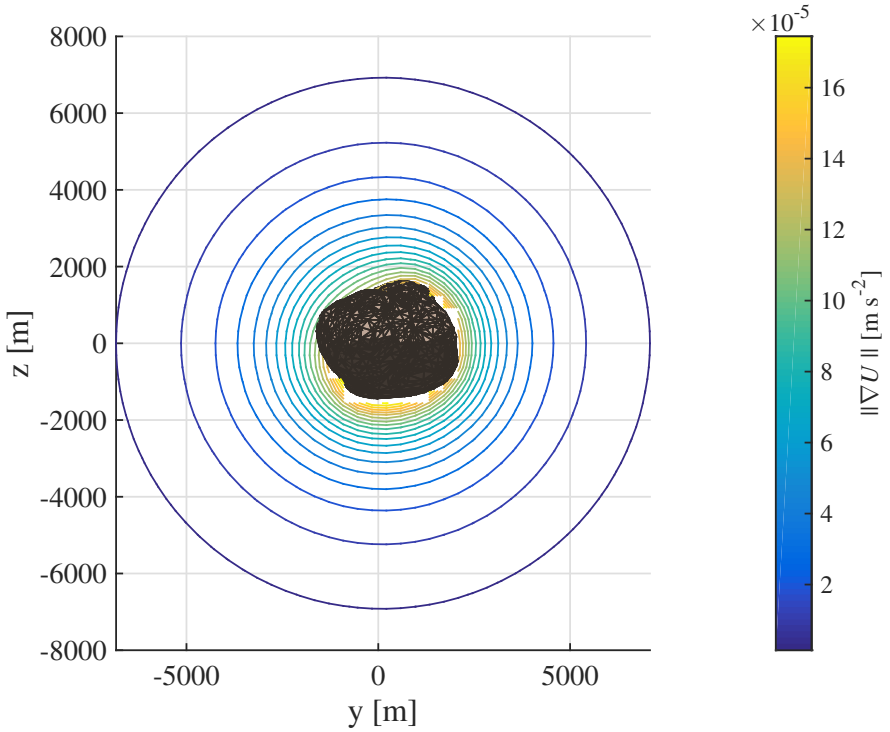

Figure 3.3: 67P Gravitational Attraction, $\|\nabla U\|$, on $yz-$plane.

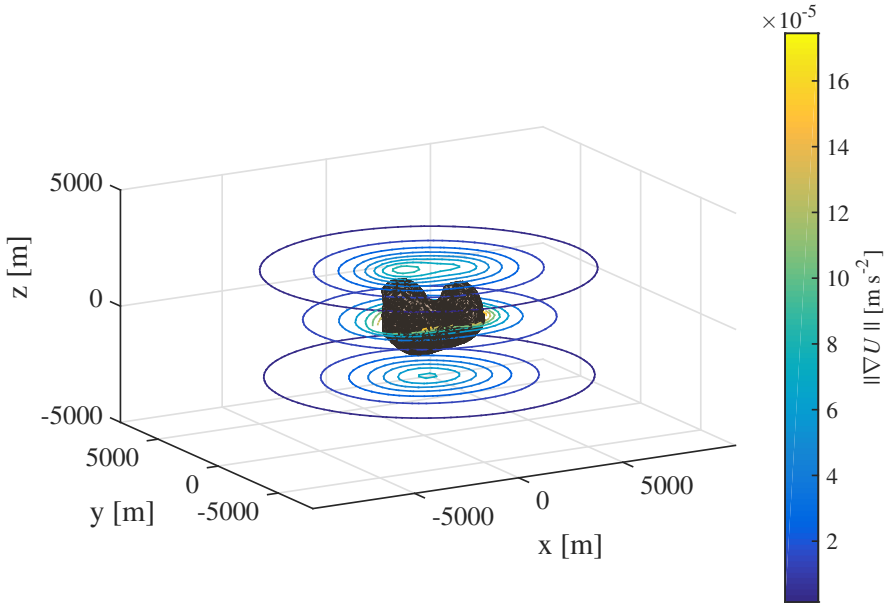

Figure 3.4: 67P Gravitational Attraction, $\|\nabla U\|$, on $xy-$planes.

figures 3.2 to 3.4 show the gravitational attraction from different angles, and the relative viewpoint is indicated in the captions of each figure. It is interesting to note that, as seen from the $yz-$plane, the comet 67P has a certain circular symmetry and this feature is obviously reflected in the gravitational field, as can be observed in figure 3.3. Instead, in figure 3.2 the elongation of the body, and accordingly, of the gravitational field, is significant, and the differences with the gravitational environment generated by a centrobaric body are evident even at a great distance from the comet.

All these plots share the already noted characteristic of the gravitational field to be highly irregular close to the surface, and more regular far from the object. This is a universal feature that characterizes the gravity field of all the analysed body and hence, in general, of all the existing objects. Having in mind this concept, any lower fidelity model has higher errors close to the surface of the body, and becomes more accurate farther from the asteroid or the comet. This aspect will be analysed in the following sections, but it is already reasonable to expect this kind of result.

3.1.2 216 Kleopatra

The asteroid 216 Kleopatra, discovered at the end of 19$^{\text{th}}$ century, is a main belt asteroid with relatively large dimensions: $217 \times 94 \times 81\text{km}$. According to [11], Kleopatra is a contact binary and the two lobes would separate from each other, creating a true binary system, if it were spinning faster. Its shape model has been obtained from ground observations, but it is still quite detailed, showing clearly its characteristic dog-bone shape.

First of all, from the $xy-$plane in figure 3.5, it can be noted that Kleopatra generates a strong gravitational field with respect to 67P Churyumov-Gerasimenko, and this is reasonable since its dimensions are remarkably larger than the ones of the comet, and being an asteroid, it has a higher bulk density. The maximum acceleration value at the surface is $a_{max} = 0.0487\text{m}\,\text{s}^{-2}$, which is only ~ 200 times smaller than the value on Earth.

Then, even in this gravity field, some analogies with a two-masses system exist; however, the high elongation is more relevant. Indeed, in the case of Kleopatra, the field is still noticeably elongated at a very large distance from the body. This feature helps to highlight an important concept, which is related with the approximation of any gravitational

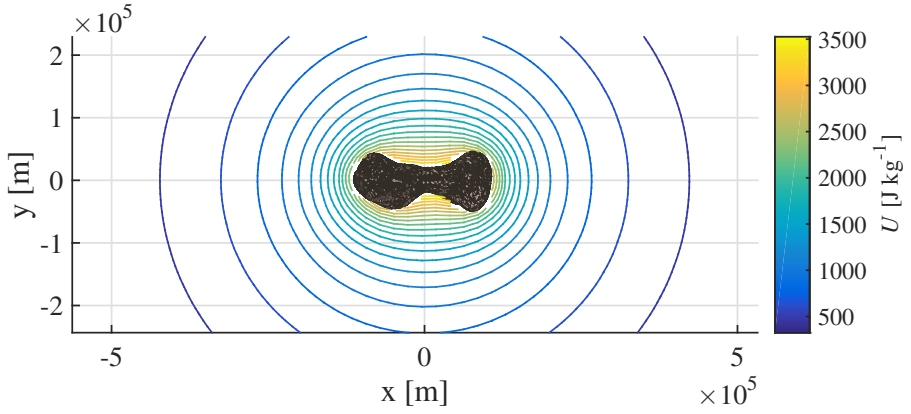

(a) Gravitational Potential, U.

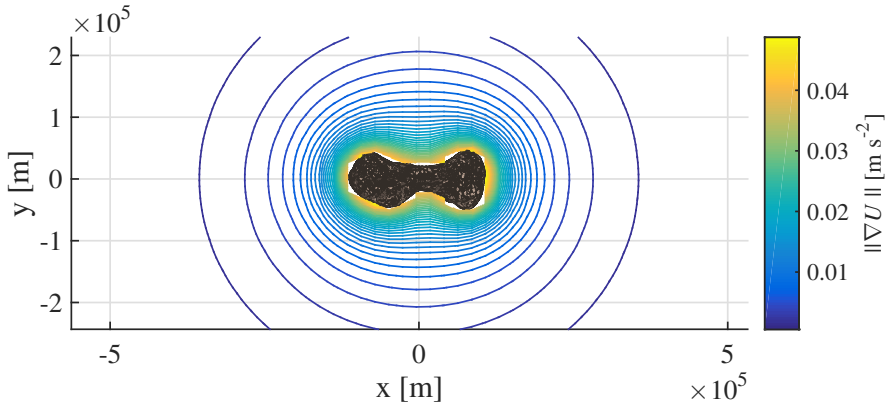

(b) Gravitational Attraction, $\|\nabla U\|$.

Figure 3.5: 216 Kleopatra Gravity Field with $\sim 5 \times 10^3$ faces Polyhedron Model.

field with the spherically symmetric one, if the point is far enough from the attractor. In fact, as already mentioned before, as the distance increases from the main body, all the irregularities become negligible and the object can be approximated with a point particle. Nevertheless, the elongation of a body is one feature that can be noticed even from a great distance, for this reason, the elongated bodies tend to have a field that is more different from the centrobaric one in a larger portion of space. This aspect will be considered again, when the field of elongated bodies will be approximated with a lower fidelity model.

3.1.3 4179 Toutatis

4179 Toutatis is a Mars-Earth crosser asteroid with a chaotic orbit generated by a resonance with Jupiter. It is classified as a potentially hazardous

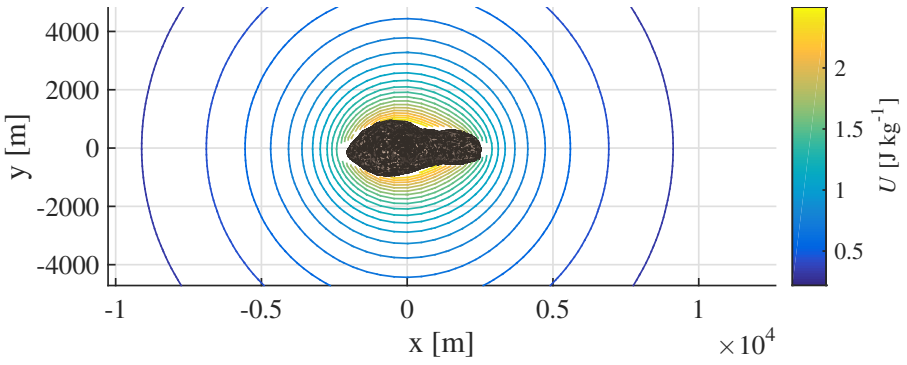

(a) Gravitational Potential, U.

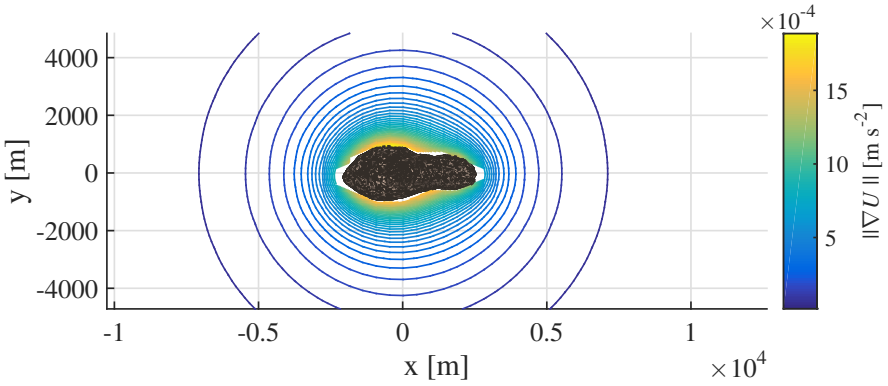

(b) Gravitational Attraction, $\|\nabla U\|$.

Figure 3.6: 4179 Toutatis Gravity Field with $\sim 5 \times 10^3$ faces Polyhedron Model.

object, since it makes close approaches to the Earth. Its shape model is quite detailed, because it has been obtained from ground observations during the asteroid's Earth flybys, and from images captured by the Chinese unmanned lunar probe, Chang'e 2, which flew close to this celestial object in 2012. Toutatis dimensions are $4.75 \times 2.4 \times 1.95\text{km}$ and its maximum gravitational attraction at the surface is $a_{max} = 0.00188\text{m}\,\text{s}^{-2}$, i.e. ~ 5000 times weaker than on the Earth. It can be noted that its dimensions are comparable to those of 67P, but its gravitational attraction is significantly higher. This is reasonable because the density of Toutatis is much higher than the one of the comet Churyumov-Gerasimenko. In figure 3.6, the gravitational potential and attraction of Toutatis are shown projected onto the $xy-$plane. From these images, the features of an elongated object can be recognized, and similar considerations to those for Kleopatra can be made. The large bulge that Toutatis has on the negative side of the $x-$axis generates a gravitational attraction that is quite large, if compared with the part of the body that is lying on the

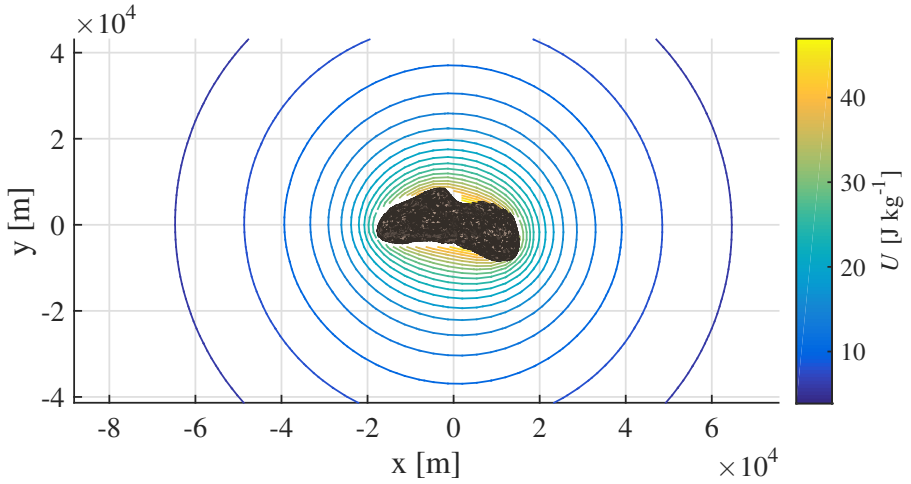

(a) Gravitational Potential, U.

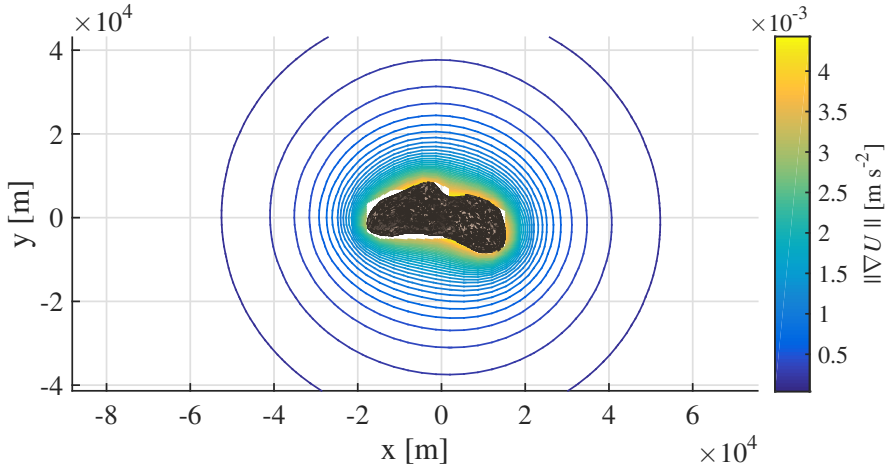

(b) Gravitational Attraction, $\|\nabla U\|$.

Figure 3.7: 433 Eros Gravity Field with $\sim 10^4$ faces Polyhedron Model.

positive half of the same axis. This feature is positive for the stability of orbits around that side of the asteroid, and it is interesting to design missions around that celestial object, as will be highlighted with some simulations in chapter 5.

3.1.4 433 Eros

433 Eros is a Mars crosser asteroid approximately $34.4 \times 11.2 \times 11.2\text{km}$ in size that was discovered at the end of the 19$^{\text{th}}$ century. It is recognized as a potential Earth impactor, and it is one of the most observed Solar

System's objects in its range of dimensions. It was accurately studied by the APL-Nasa's space probe, NEAR-Shoemekar, at beginning of the new millennium. The mission was supposed to rendezvous with the asteroid, orbit it several times and land on its surface. The mission was successful and Eros was the first asteroid orbited by an Earth probe. Consequently, the available shape model of this object is highly detailed, and also the physical characteristics are well defined.

The obtained gravitational field is shown in figure 3.7 with a projection onto the $xy-$plane. The field of Eros shows features that are similar to those of the previous bodies: the elongation is still evident quite far from the surface of the body, the gravitational attraction is particularly strong close to the main lobes of the body and it is pretty irregular in vicinity of the surface. The maximum gravitational attraction at the surface is $a_{max} = 0.00442\mathrm{m\,s^{-2}}$, approximately 2000 times weaker than on the Earth's surface.

This is the only shape model, among the selected bodies, which is not aligned with the principal inertia reference frame. Indeed, there is a small deviation angle, around the $\hat{\mathbf{z}}$ axis, between the shape model reference and the B reference that is used in this work. This is not a problem for the present purposes, but the shape model will be rotated, to be correctly used in the equations of motion.

3.1.5 1580 Betulia

The asteroid 1580 Betulia is an Amor asteroid that was discovered in the mid of the 20$^{\text{th}}$ century. Its shape has been determined from light curves obtained with ground observations. According to [27], it could be an extinct comet nucleus, because of its unusually high orbital inclination and its carbonaceous composition. Moreover, the derivation of its shape model was quite interesting because of the uniqueness of its triple-peaked light curve.

From the most recent data available, the field shown in figure 3.8 was obtained. Betulia dimensions are $6.29 \times 6.59 \times 4.12\mathrm{km}$ and its maximum gravitational acceleration at the surface is $a_{max} = 0.00341\mathrm{m\,s^{-2}}$, which is ~ 3000 times lower than the Earth's gravitational acceleration.

This asteroid is not completely spherical, since it has one flat side and its polar diameter is lower than its equatorial one. However, compared to the other bodies that are currently analysed, it can be used as a reference for the class of the spherical asteroids. Indeed, its elongation is limited in all the three main dimensions, and this is confirmed also from the

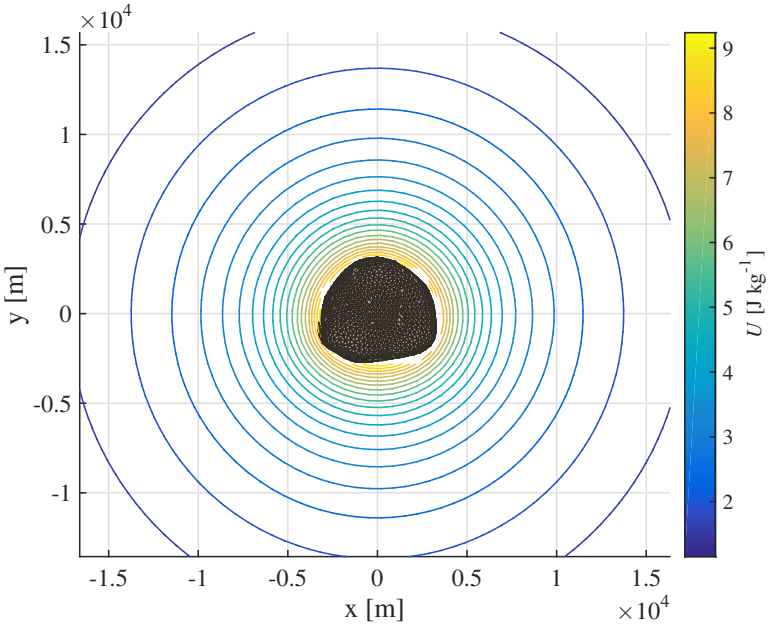

(a) Gravitational Potential, U.

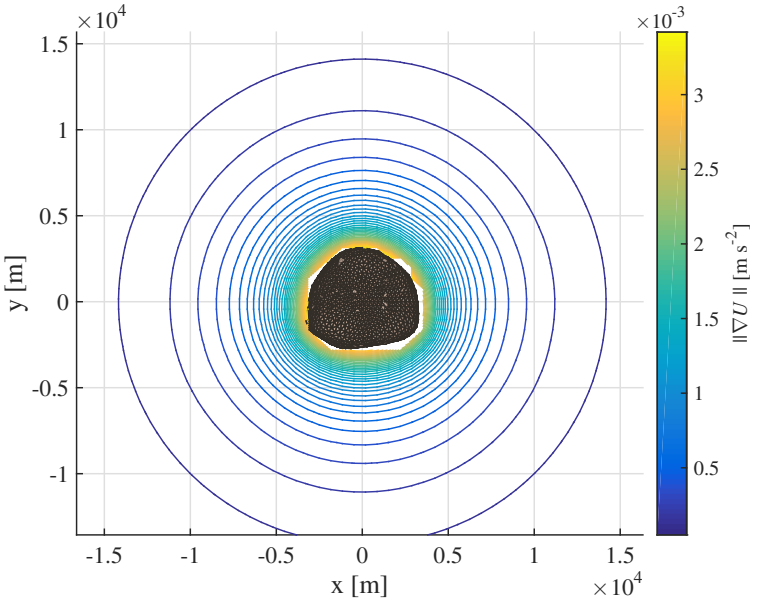

(b) Gravitational Attraction, $\|\nabla U\|$.

Figure 3.8: 1580 Betulia Gravity Field with $\sim 5 \times 10^3$ faces Polyhedron Model.

almost circular symmetry of the gravitational potential projected onto the $xy-$plane, as shown in figure 3.8a. Furthermore, looking at the same figure, the triple-peaked light curve can be explained considering

the triangular deformation of Betulia along its equator; obviously, this is reflected in the gravity field and determines some features of the dynamical environment in the vicinity of this body.

3.2 Gravity Models Comparison

In the previous section the gravitational fields were all computed by means of the polyhedron approach, and it is reasonable to wonder what are the differences with the results obtained exploiting the other modelling technique: the mascons approach.

Moreover, it is extremely interesting and important to understand the validity and the accuracy of different methods. The importance of this comparison can be easily explained having in mind that the absolute best technique does not exist. In fact, each procedure can have positive aspects and drawbacks, and it is more valuable to delineate the limits of validity and the range of application of a method. In this way, the best modelling approach, according to the current problem requirements, can be selected. For example, the convergence problems of the spherical harmonic expansion close to the surface of the irregular body restrict the usage of this technique for the purposes of this thesis, and thus it is not used in this work. Nevertheless, the analytical analyses that can be carried out with the series expansion could be extremely useful for other applications.

First, to have a preliminary and insightful overview on the differences between the polyhedron and the mascons approach, their results can be compared using geometries that are simpler than the real ones.

3.2.1 Sphere and Ellipsoid Analysis

The two gravitational modelling techniques are now compared on a sphere and on two axially symmetric ellipsoids. The study of these simple geometries allows focusing the analysis on the general differences between the two different approaches, with the goal to define some guidelines that are valid for all the particular real situations.

The sphere has radius equal to $10\,\mathrm{m}$ and its field is computed using a ~ 3000 faces polyhedron and ~ 5000 mascons on an evenly spaced grid. The overall mass of the spherical body is maintained as constant between the two different techniques. The potential and the gravitational attraction are evaluated in a 3D grid with 125000 points around the central body, and then the relative error between the two techniques is

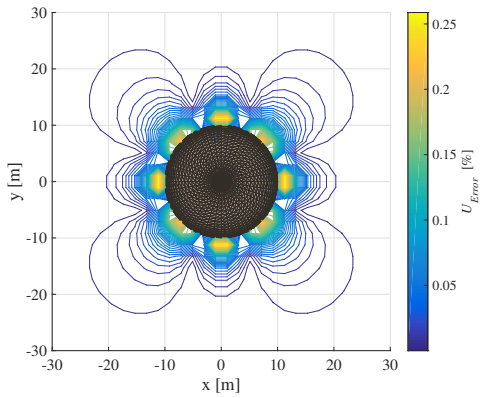

(a) Percent error on gravitational potential.

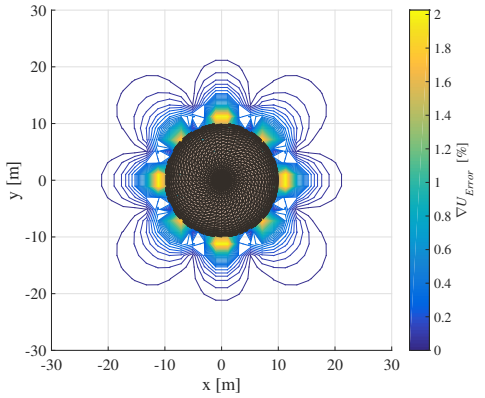

(b) Percent error on gravitational attraction.

Figure 3.9: 5000 Mascons and 3000 faces Polyhedron approach comparison on a 10 m Sphere.

computed. The polyhedron model is assumed to be more accurate than the mascons one, since its fidelity depends only on the shape approximation of the body. In this case, the sphere is very well reproduced with the chosen number of faces, and therefore the polyhedron model is taken as a reference to estimate the relative error of the mascons approach. As example, the relative error on the gravitational potential is computed, in percentage, as:

$$U_{Error} = 100 \times \left| \frac{U_{Poly} - U_{Mascons}}{U_{Poly}} \right|, \tag{3.1}$$

and in a similar manner the error on the attraction is available.

The result obtained, on the $xy-$plane, is reported in figure 3.9. As a first remark, the error is high close to the surface and decreases at a greater distance from the body. This can be explained considering than the real solid body is replaced with a discrete number of point masses, and close to the surface, this difference is more evident. Then, the lobed shape of the error can be noted, and it can be explained assuming that the point masses are represented as spheres that fill the volume of the body, and that they touch without overlap. In this way, a cubic differential volume of the real continuous body can be replaced with its inscribed sphere, but each sphere occupies only 52% of the original volume of the cube, and its density is twice the original. So, if the gravitational field of a unit mass cube is compared with the field of a unit mass inscribed sphere a lobed error pattern is obtained. Hence, the lobed shape of the

error is the typical result for the mascons approach, and the obtained pattern depends on the distribution of the point masses inside the body.

In figure 3.9a, the maximum error of the mascons approach is around 0.25%, while in figure 3.9b the error is one order of magnitude higher, and its maximum value is approximately equal to 2%. This is another general feature of the comparison of the mascons approach with the polyhedron model; in fact, the acceleration field is normally less accurate than the potential field. In the mascons approach, the source of the field is a point mass, which is a singularity, and the differentiation process enhance this problem. Thus, the mascons gravitational attraction has a large error with respect to the potential, and the region in which the error is still relevant extends well away from the body.

Obviously, the modelling error is proportional to the mascons resolution, and with a larger number of point masses, the error can be further reduced. However, according to [55], the number of mascons needed is inversely proportional to the cube of the size of each mascon. As a consequence, to reduce the error of the mascons model of one order of magnitude, the number of point masses has to be increased, in general, of three orders of magnitude.

The same analysis can be repeated also with simple elongated bodies; in this case two axially symmetric ellipsoids. These bodies are assumed to have the same density and transversal dimensions of the sphere presented before. So, the semi-axes along $\hat{\mathbf{y}}$ and $\hat{\mathbf{z}}$ are equal to $10\,\mathrm{m}$. The ellipsoids have been discretized with a ~ 3000 faces polyhedron and ~ 5000 gridded mascons. The $\hat{\mathbf{x}}$ dimension characterizes the two different cases with two different elongation levels: one ellipsoid has the third semi-axis equal to $20\,\mathrm{m}$, while the other has that semi-axis equal to $50\,\mathrm{m}$. They will be referred to as $2/1/1$ and $5/1/1$ ellipsoids, respectively. The relative errors between the mascons and the polyhedron attraction are reported in figure 3.10.

Some considerations on these plots are the same to the ones discussed before with the spherical case, showing that these features are related with the mascons approach and are independent from the geometry of the object that is being considered. Nevertheless, looking at the two different ellipsoids, another important characteristic of this modelling technique can be highlighted. The maximum error in figure 3.10a is in the order of 3%, and in figure 3.10b is around 8%. For the spherical case, it was $\sim 2\%$. This is not casual, and in general, the mascons approach produces less accurate results when working with elongated bodies. The spherical symmetry of the field generated by a point mass works better with bodies that maintain this symmetry also in the mascons

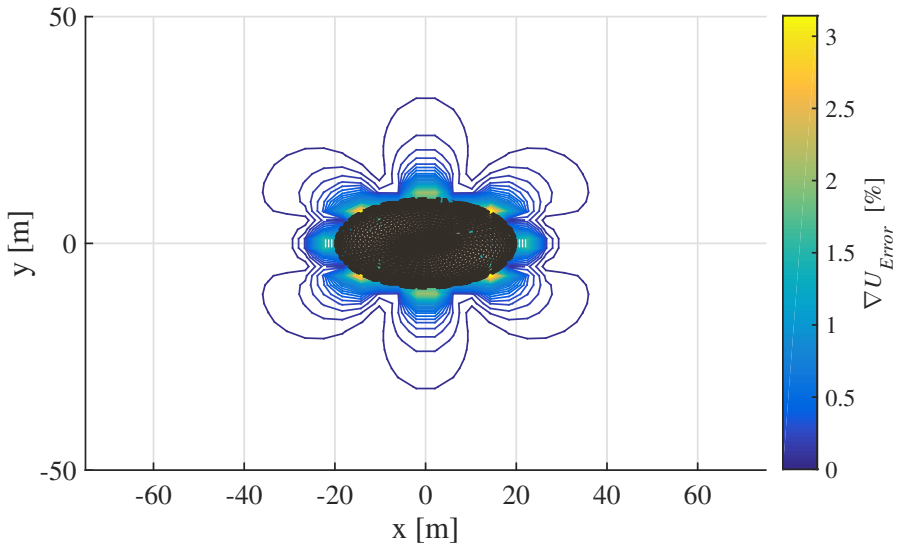

(a) Percent error on gravitational attraction, $2/1/1$ ellipsoid.

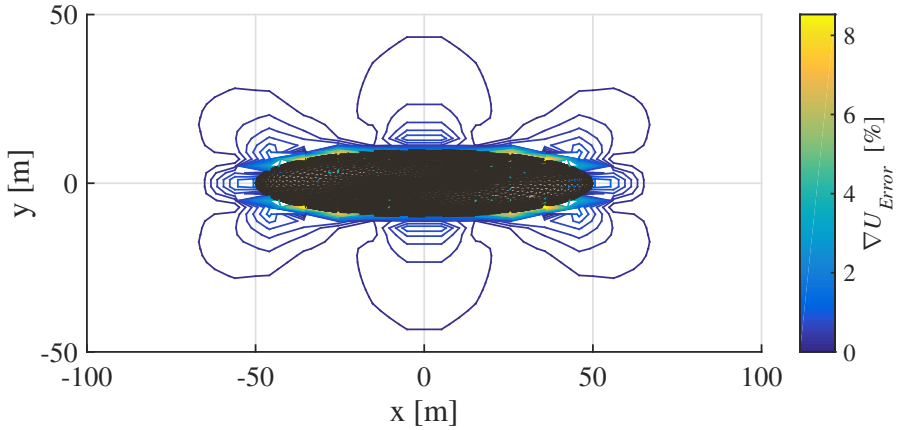

(b) Percent error on gravitational attraction, $5/1/1$ ellipsoid.

Figure 3.10: 5000 Mascons and 3000 faces Polyhedron approach comparison on $20\,\mathrm{m}$ and $50\,\mathrm{m}$ ellipsoids.

distribution. With oblong geometries, several spherical fields must be aligned to produce the elongated shape of the overall contribution; this leads to a higher error on the longer side of the object. In fact, the error close to the shortest side of the ellipsoid is lower than the one along the $x-$axis, as can be seen from the small lobes on the left and the right side of the body. The mascons approach is more suitable for computing the field close to quasi-spherical and not elongated geometries.

The comparison between polyhedron and mascon approach can be carried out also on the real geometries of the selected celestial bodies.

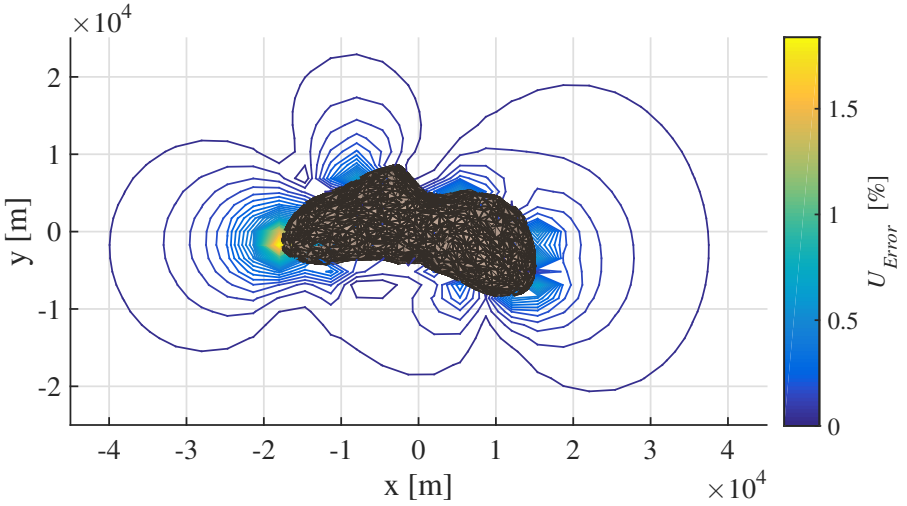

(a) Percent error on gravitational potential.

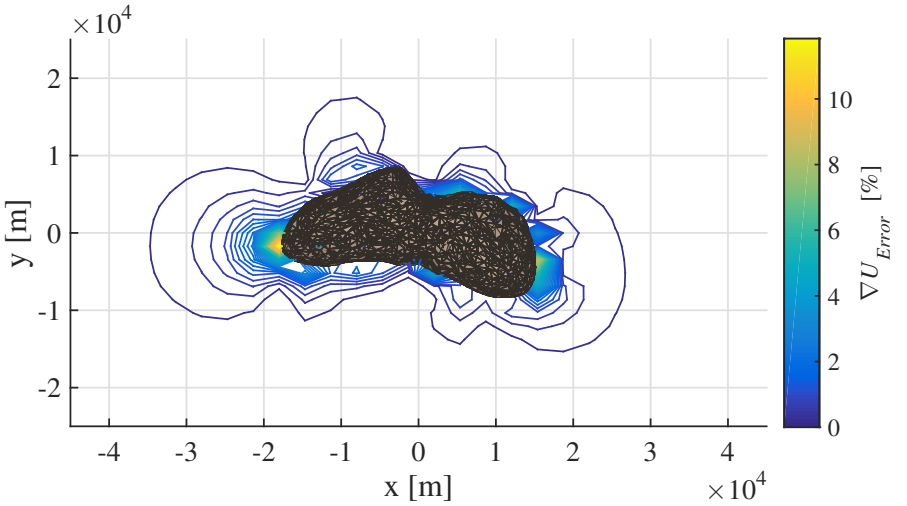

(b) Percent error on gravitational attraction.

Figure 3.11: ~ 2500 mascons and $\sim 10^4$ faces polyhedron approach comparison on 433 Eros.

As an example, the Eros case in reported in figure 3.11. Here, the error is higher and less intuitive to understand, because of the several irregularities that are present on the real asteroid. However, some characteristics that have been described before are still present and evident; this is in general true for all the real geometries that can be analysed with this method.

As a general remark for the gridded mascons approach, the shape of the error is dependent from the number of point masses that are

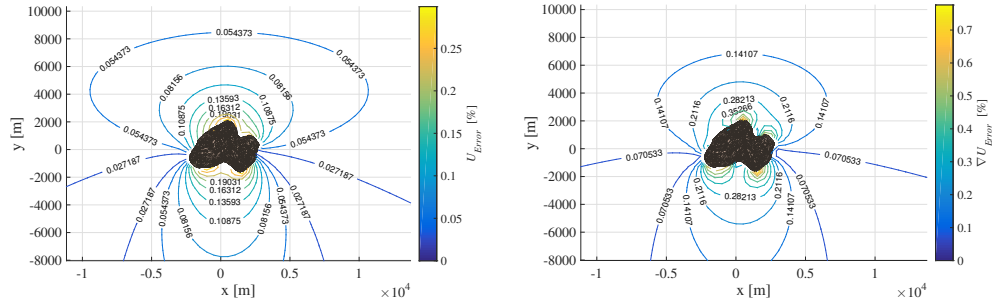

(a) Percent error on gravitational potential.

(b) Percent error on gravitational attraction.

Figure 3.12: Percent error on gravitational potential and attraction of 15000 faces polyhedron on 67P with respect to the Hi-Fi polyhedron model.

used. This is because the distribution of mascons in a grid changes for a different number of masses, and these different arrangements are not determined by the shape of the body, but just from a simple subdivision of the internal volume. In this way, some characteristics of the field of the object can be accurately represented with a certain resolution of the grid and not with a different one. So, even if the magnitude of the inaccuracy normally decreases if the number of mascons is increased, the shape of the error does not follow a well defined trend and the error analysis should be performed from case to case.

All these aspects will be discussed in section 3.2.3. Now it is useful to understand the influence of the number of faces on the results of the polyhedron shape approach.

3.2.2 Polyhedron Shape Approach Analysis

The polyhedron shape approach gives results with an accuracy determined by the resolution of the shape discretization. For this reason, different results of this modelling technique have been compared for different number of faces of the polyhedron shape model. The Delaunay triangulation, which is used in this thesis, allows rescaling the original shape model and obtaining a new one with an arbitrary number of faces. Obviously, the geometry of the body is slightly modified and the models with a low number of polyhedra lose several surface details. Notwithstanding, the scaling algorithm tries to preserve the overall shape and volume of the body, and if a reasonably low number of faces is employed, the model drops only the finer details on the surface of the object. In the following analysis, the Hi-Fi polyhedron model, $\sim 2 \times 10^4$ faces, is the

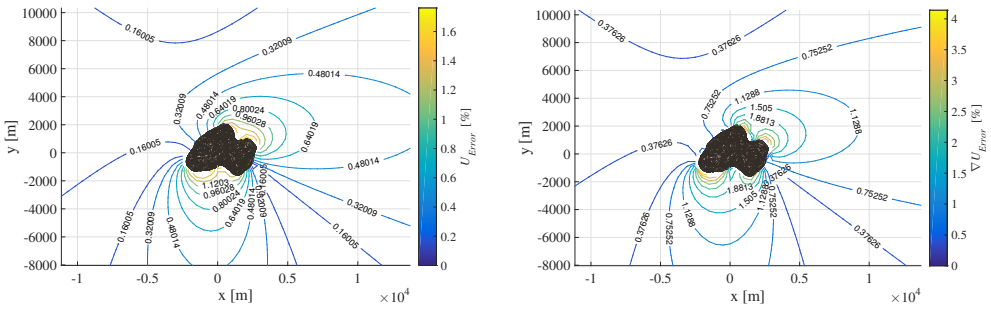

(a) Percent error on gravitational potential.

(b) Percent error on gravitational attraction.

Figure 3.13: Percent error on gravitational potential and attraction of 1000 faces polyhedron on 67P with respect to the Hi-Fi polyhedron model.

reference to estimate the relative error of the different Lo-Fi models. The strategy to perform the comparison is the same that has been presented in section 3.2.1, and the only difference lies in the involved quantities. Now, indeed, is not the mascons approach to be compared with the Hi-Fi polyhedron model, but several Lo-Fi polyhedron models are compared with a higher fidelity field obtained with the same technique.

In figure 3.12, the Hi-Fi model is compared with a very similar Lo-Fi model composed by $N = 15000$ faces. While, in figure 3.13, the Lo-Fi model has $N = 1000$ faces and the difference with the reference field is more noticeable. As expected, the error is higher when a lower fidelity model is used, and the gravitational attraction has a large error if compared with the potential. However, in this case, the difference is not as apparent as in the mascons case, since the polyhedron has not dimensionless elements and the differentiation process operates on smooth quantities. Even in this example, the error is higher close to the surface, mainly because the details on the surface are different or not present anymore when a lower number of faces is used.

At this point, in order to have a general trend of the error, as a function of the number of employed faces, several Lo-Fi models are compared with the Hi-Fi polyhedron model. Nevertheless, a more intuitive understanding of the behaviour is possible if the error data are reduced in a handy form.

The error data contained in the 3D grid around the body are statistically analysed in order to obtain some quantities that can be easily compared. In the present situation, involving different resolution polyhedron models, the mean and the maximum values of the error in the field are evaluated and compared. They are sufficient to describe the

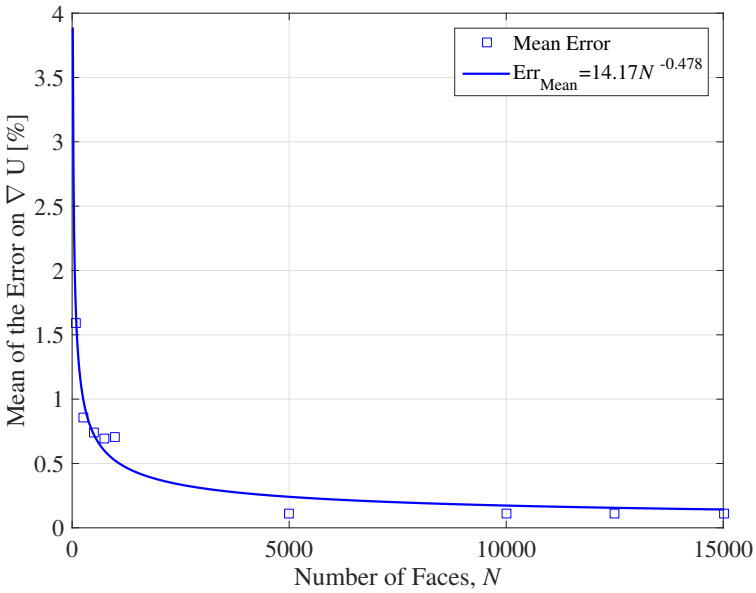

(a) Mean of the Error on ∇U.

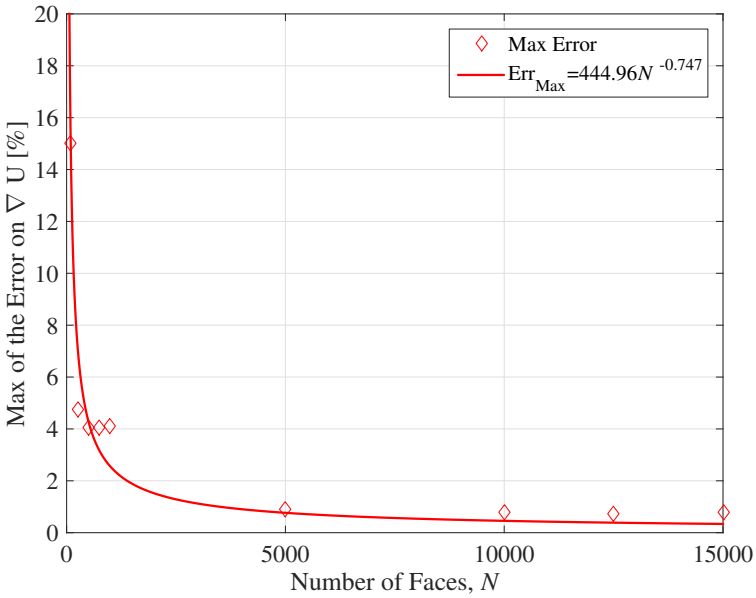

(b) Maximum Error on ∇U.

Figure 3.14: Percent error on gravitational attraction of N faces polyhedron on 67P with respect to the Hi-Fi polyhedron model.

different instances, since the obtained results have approximately the same variance and the error distribution is well defined using these two parameters. Actually, only the mean of the error is necessary to

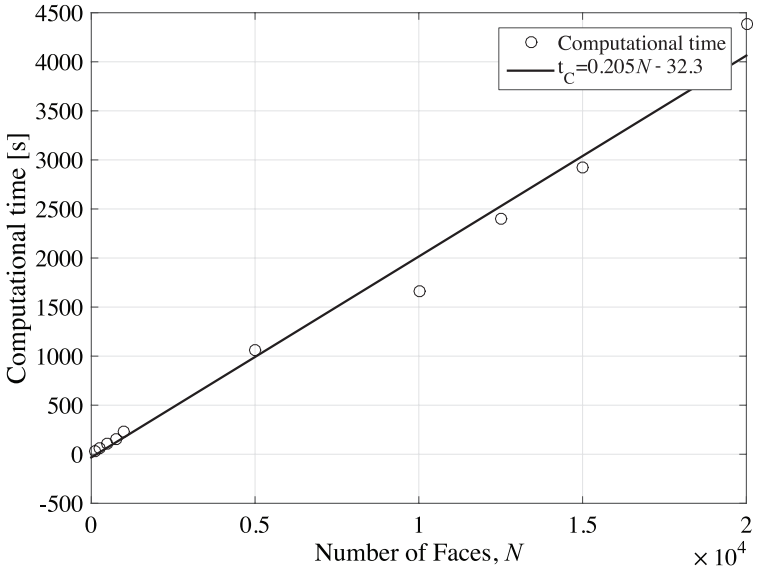

Figure 3.15: Required computational time with N faces polyhedron model on a 50×50 2D grid, with parallel computing techniques on a quad-core $2.50\,\mathrm{GHz}$ processor.

characterize the error field, but the maximum value is useful anyway to know the bounds of the resulting accuracy. Figure 3.14 shows the evolution of these two quantities for different values of N on the comet 67P Churyumov-Gerasimenko.

The trends in figure 3.14a and figure 3.14b are the result of a nonlinear regression on the available data, the obtained best-fitting equations are presented in the legend of the plots. These particular relations have not general validity, since they are evaluated for a particular shape model. However, these trends are obtained also for other shapes, and in general, the mean of the error shows to approximately decrease with the inverse of the square root of N. This result can be used to estimate the increase in accuracy that can be obtained with a different number of faces with respect to an already known error field.

The increase in accuracy is not for free, and the drawback is the increase in the needed computational time. The threshold to define a tolerable time depends on the particular application; therefore, the optimal number of faces that balance a reasonable level of accuracy with an acceptable computational time cannot be univocally defined and the requirements must be stated from case to case. Anyway, the time required to evaluate the different polyhedron fields is shown in figure 3.15, and these values could be used as a reference for future works.

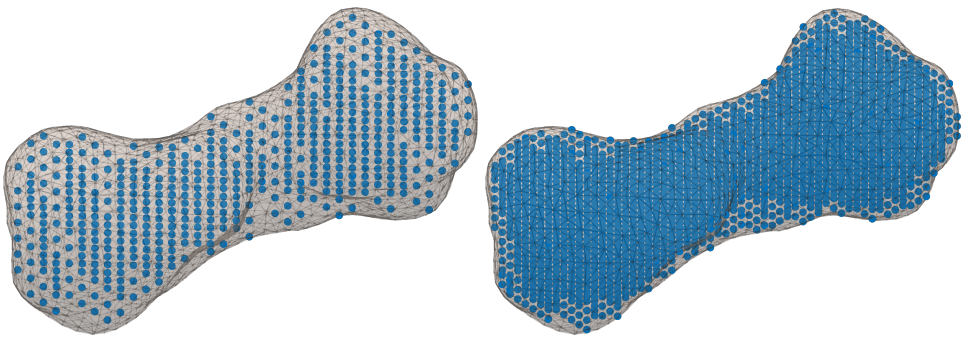

(a) ~ 500 point masses. (b) ~ 2500 point masses.

Figure 3.16: Gridded mascons approach on 216 Kleopatra.

In this analysis, the gravitational potential and attraction are computed using a MATLAB® code that makes use of parallel computing techniques on a quad-core $2.50\,\mathrm{GHz}$ processor. The code computes the field for a given z value on a 50×50 2D grid, thus the time to compute these quantities on a single field point is $\mathrm{t_C}/2500$. The obtained best-fitting equations show, as expected, a linear relation between the different values of N.

A similar analysis can be carried out for the gridded mascons approach, with the purpose to see how a different number of mascons affect the result if compared with the Hi-Fi polyhedron model.

3.2.3 Mascons Approach Analys

The gridded mascons approach fill the volume with point masses arranged in a grid that is obviously dependent from the number of used mascons, as can be seen in figure 3.16, for the asteroid 216 Kleopatra. In addition, the standard gridded mascons use N_m point masses of equal mass $m = M/N_m$. The resulting field is more accurate if a larger number of mascons is used, but as already said, also the shape of the error is dependent from N_m. A dissimilar distribution of masses can determine a better or worse representation of the particular body, and if the object is filled with a regular grid, the result can be particularly different even if a similar number of mascons is used. That is because the gridded approach creates the evenly spaced grid along $\hat{\mathbf{x}}$, $\hat{\mathbf{y}}$ and $\hat{\mathbf{z}}$ regardless of the actual shape of the body. This problem is notably relevant if N_m is low, since, with few masses, adding or subtracting only one element can determine a drastic change in the mass distribution, and as a consequence, in the obtained field.

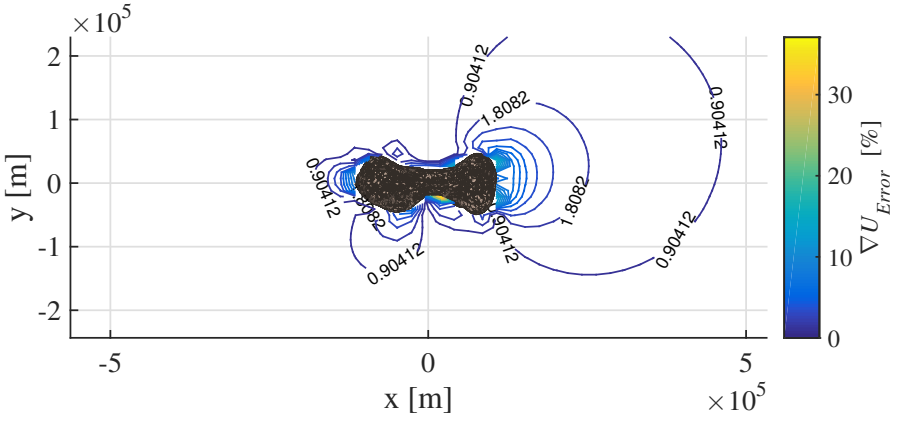

(a) $\sim$ 500 point masses.

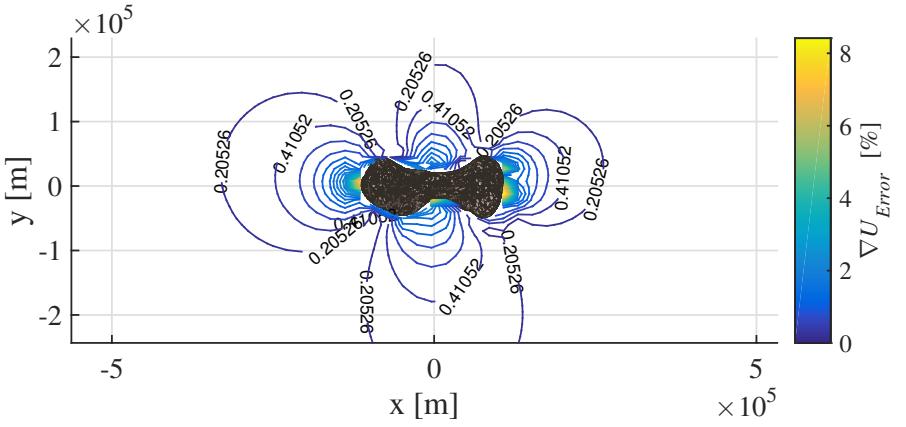

(b) $\sim$ 2500 point masses.

Figure 3.17: Percent error on gravitational attraction with gridded mascons on 216 Kleopatra.

This concept is more clear looking at figure 3.17, where the errors of the gravitational attraction are computed comparing two different mascons models and the Hi-Fi polyhedron. The maximum error for the ~ 2500 mascons, figure 3.17b, is obviously lower than the error for the model containing ~ 500 mascons, figure 3.17b, but there is no actual relation between the two shapes and distributions of error. This can be a problem, because there is not a deterministic evolution for the reduction of the error and each case must be analysed to understand the level of accuracy. For sure, the general rule to increase N_m in order to reduce the error is globally valid, but a not negligible level of randomness is still present. Moreover, it is reasonable to wonder if a better way to distribute the N_m mascons exist. Hence, an optimized version of the

mascons approach is developed and presented. Then, both the gridded and the optimized mascons are compared together, as a function of the number of used point masses.

3.3 Optimized Mascons Approach

The usual mascons approach fills the volume of the body distributing the point masses in an evenly spaced grid, and assumes that all the mascons have the same mass. This method can be reasonable if an extremely large number of elements is used, but with few masses the gridded distribution can be not effective, and the problem concerning the erratic reduction of the error can be tedious for certain applications. The developed optimized version of this modelling technique tries to improve the performances of the mascons approach distributing the point masses within the body according to certain optimization criteria.

The basic goal of the optimized mascons approach is to find a certain distribution of point masses recreating the field of the Hi-Fi polyhedron model, which in this work is assumed as the *model of reality*. It is worthwhile to point out that the desired optimum distribution of mass is not the real mass distribution of the actual body, which is usually unknown. Certainly, if the exact mass model were available, the optimum solution would be the one closest to the reality, with the purpose to obtain the most accurate gravitational field. Notwithstanding, the best model that is available here is the constant density Hi-Fi polyhedron, and for this reason, the optimization algorithm attempts to match the field generated by this reference model.

The first element that has to be defined to run the optimization process is the *objective function*. This is the function evaluated at each iteration step and it is needed to understand which is the best solution. In fact, the optimal solution is the one that minimizes the objective function. This aspect has to be accurately managed, since it determines the result of the optimization process, and a not appropriate objective function could lead the algorithm towards a wrong best solution. The aim of this research work is to find a good representation of the gravity field around an irregularly-shaped body to be used to describe the dynamics of a particle in its vicinity. Therefore, the goal of the optimization problem is to find the solution that minimizes the error in the gravitational contribution inside the equations of motion: the gradient of the potential, ∇U.

This optimization goal could be implemented in several ways, and for sure, there were other meaningful possibilities to find the best solution. For instance, the algorithm was also tested minimizing the error on the potential, U_{Error}, but the results were not satisfactory for the gravitational attraction. Then a combined objective function, involving both the potential and its gradient, was analysed, but even in this case the results were not as good as when only ∇U_{Error} is minimized. So, the best solutions to be used in the dynamical model are obtained minimizing the error on ∇U, which is anyway an upper bound for the error on the gravitational potential, and thus, U_{Error} is guaranteed not to diverge.

The implementation of the minimization of ∇U_{Error} is another important aspect to consider, indeed the optimization problem can be developed for a global quantity or a local one. In this work the mean of the error on the whole 3D grid is the global quantity to be minimized. This choice is supported from several tests using any possible estimator of the error on the gravitational attraction, but the best results were obtained using the mean value. As example, the minimization of the maximum performs well locally, close to the surface of the body, but in general, gives high errors and the obtained field accuracy is low. In addition, a combined minimization, e.g mean and maximum value or mean and variance, was tested, but the best global solutions is found when the minimum mean of the error is found.

Hence, the optimization algorithm find the best mascons distribution that minimizes the mean of error on the gravitational attraction computed on a 125000 points 3D grid surrounding the main irregular body. The error is computed as a percent value with respect to the Hi-Fi polyhedron model. The algorithm can move the mascons within the volume of the body and the mass is not constrained to be the same for each point mass. As long as the global mass of the body is maintained constant and no point mass is outside the physical boundaries of the celestial object, any position and any mass value for the single mascons are allowed. Consequently, this is a constrained optimization problem and it is implemented using a genetic algorithm. The genetic algorithm is a valid algorithm since both the objective function and the constraints are non-smooth, and there is no analytical and differentiable formulation of the problem. The output of the optimization process is a $N_m \times 4$ matrix containing the position and the mass value of each mascons.

3.3.1 Genetic Algorithm

The genetic algorithm is a method for solving both constrained and unconstrained optimization problems that is based on natural selection, the process that drives biological evolution [29]. The idea behind this kind of evolutionary algorithms is probably due to Alan Turing, who proposed the concept of a *learning machine* based on the principles of evolution in 1950. All the practical implementations were developed in the second half of the 20^{th} century for several and different applications.

The genetic algorithm begins by generating an initial population composed by a random set of individual solutions that satisfy the imposed constraints. Then, at each step, the population is modified and the best temporary solution is identified. As a result, over successive iterations, the population evolves towards an optimal solution, because the genetic algorithm selects different individuals from the i-th population to be parents, and uses them to produce the children for the $(i+1)$-th generation. The genetic algorithm allows solving problems, like the present one, which are not well suited for standard optimization algorithms.

The rules that are applied at each step to create the next generation from the current population are: *selection rules* to select the individual solutions, called parents, that contribute their *genes* to the population at the next generation, *crossover rules* to combine two parents to form children for the next generation, and *mutation rules* to apply random changes to individual solutions to form children. This algorithm differs from a classical optimization technique, because it works with an ensemble of solutions, and not with a single point, but the main difference is related with the large use of random number generators instead of deterministic schemes.

The genetic algorithm creates three types of children for the next generation: *elite children* representing a group of the best solutions that survive to the next generation, *crossover children* created by combining a pair of parents according to the crossover rules, and *mutation children* created by introducing random changes to a single solution, as specified by the mutation rules.

The constraints are enforced at each iteration step, and the individuals that do not satisfy the constraint equations are suppressed and eliminated from the next population; their genes are likely to disappear and they become extinct. This process is carried out by means of a penalty algorithm that finds feasible individuals among a certain population.

The algorithm converges to the optimum solution when the change in the objective function is less than a certain tolerance between two consecutive iterations.

3.3.2 Optimization Algorithm Definition

In this thesis, the algorithm is practically implemented using a discretized volume that is already constrained inside the body. The discretization of the domain of the possible solutions is negligible for practical applications, since there are more than $\sim 10^6$ available positions within the volume. Hence, the problem is an integer optimization problem, and the constraints are directly applied on the domain of the possible solution, i.e. all the individuals are feasible. The reason for this choice is the computational speed, and this procedure has been proved to be equivalent to a continuos standard genetic algorithm with constraints enforced between two consecutive generations.

The algorithm tries to find a global optimal solution, and thus the population diversity is as high as possible. The initial range to create the first random generation is particularly wide and tries to include the largest variety of genes. Moreover, the defined mutation and crossover rules allow spanning as much as possible the domain of all the feasible solutions. The tuning of the genetic algorithm parameters has been performed on simple model where the optimum solution was known. The robustness and the effectiveness of this procedure have been verified computing the best solution for a single case several times. Then, the consistence of this collection of optimal solutions is checked, and only if it is confirmed the optimum mascons distribution is saved.

3.3.3 Optimization Results

This modelling technique has been applied with all the selected bodies, but only two results are presented here. In figure 3.18, the optimized mascons approach is employed on 4179 Toutatis and in figure 3.19 on 67P Churyumov-Gerasimenko.

These plots are representative for the main advantages of the optimized mascons approach. In fact, as a first remark, the reduction of the error follows a reasonable trend, and it is almost possible to predict the evolution of the error shape. Moreover, there is logic in the distribution of the point masses inside the body and this determines, in general, low errors with respect to the gridded mascons approach. As a

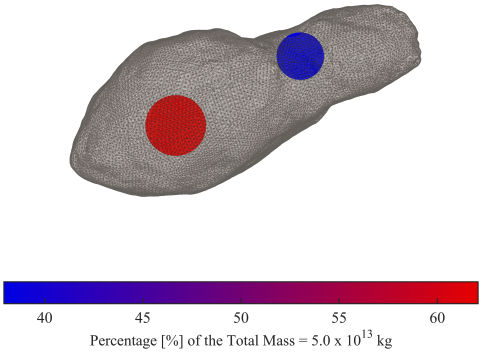

(a) Optimum mascons, $N_m = 2$

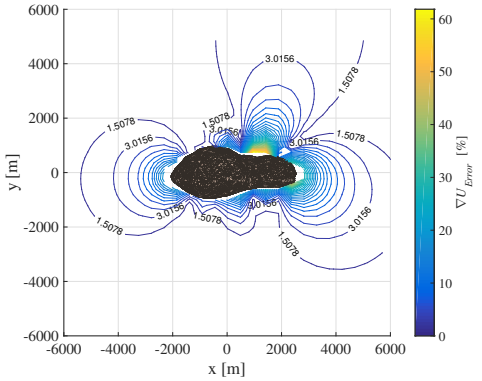

(b) Percent error on gravitational attraction, $N_m = 2$

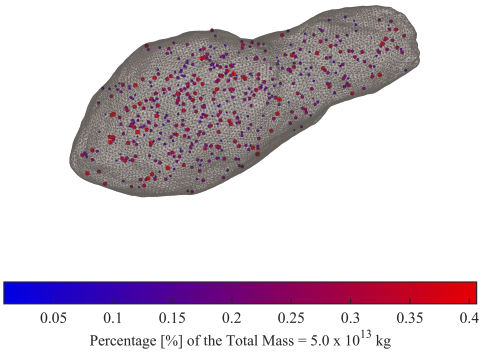

(c) Optimum mascons, $N_m = 500$

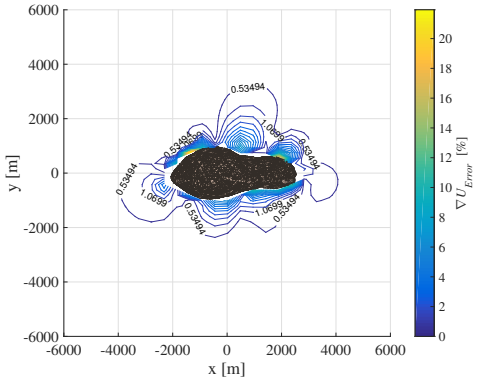

(d) Percent error on gravitational attraction, $N_m = 500$

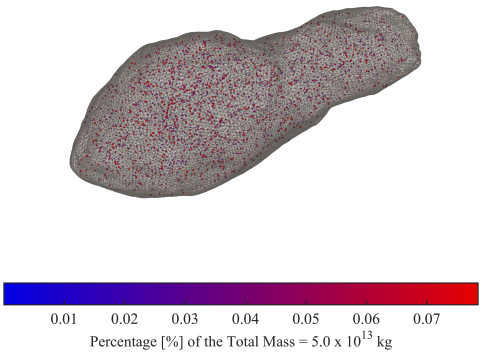

(e) Optimum mascons, $N_m = 2500$

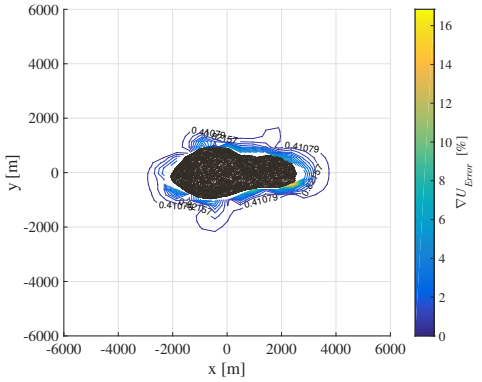

(f) Percent error on gravitational attraction, $N_m = 2500$

Figure 3.18: Optimized mascons approach on 4179 Toutatis.

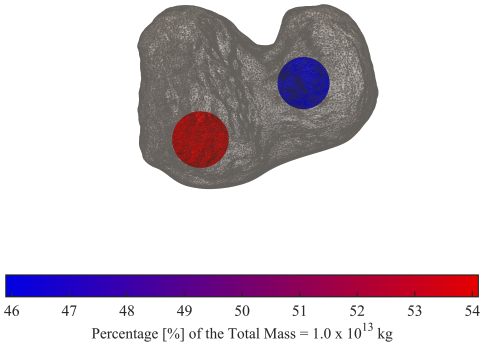

(a) Optimum mascons, $N_m = 2$

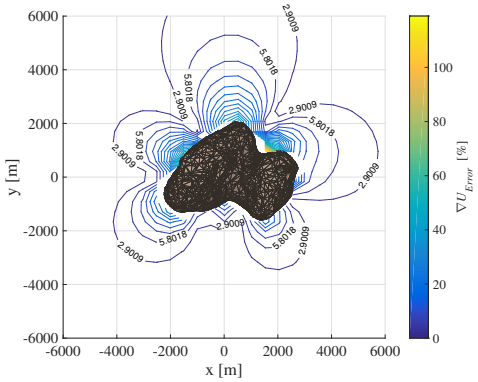

(b) Percent error on gravitational attraction, $N_m = 2$

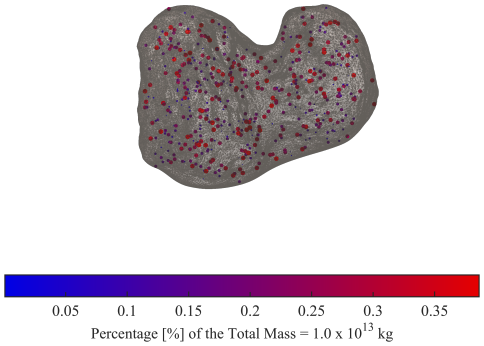

(c) Optimum mascons, $N_m = 500$

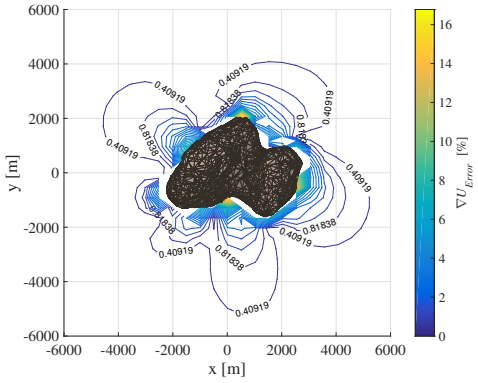

(d) Percent error on gravitational attraction, $N_m = 500$

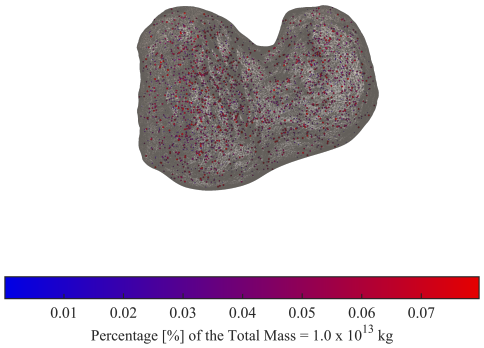

(e) Optimum mascons, $N_m = 2500$

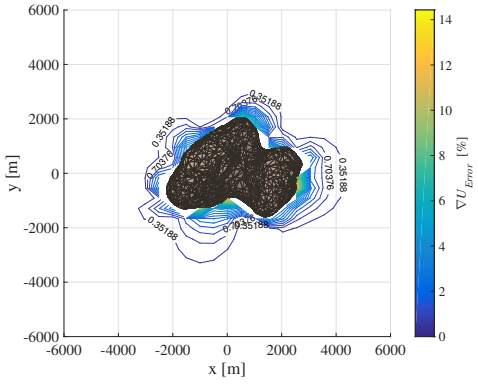

(f) Percent error on gravitational attraction, $N_m = 2500$

Figure 3.19: Optimized mascons approach on 67P.

consequence, the 2 mascons model now produces acceptable results that can be utilized for a preliminary study of the dynamical environment. Obviously the level of the error is high, close to the surface in particular, but this extremely simple model allow the usage of the circular restricted three-body problem equations. This formulation has several advantaged, since it is extensively studied and allows an insightful overview of the environment in the vicinity of these celestial objects [14, 15].

The error clearly decreases for an increasing number of masses, but in order to have a better understanding about the relation between the number of mascons and the error, a statistical analysis, similar to the one presented in section 3.2.2, is performed.

3.4 Mascons Models Comparison

The gridded and the optimized mascons approaches are here compared exploiting the mean value of the error on the gravitational attraction around the irregular body. This quantity is used to characterize the error field, and in addition, it is the objective function in the optimization problem to find the best mascons distribution. Therefore, this section helps also to directly understand the improvement of the optimized approach over the gridded one. Figure 3.20 shows the relation between the mean value of the error and the number of point masses, N_m, on the comet 67P Churyumov-Gerasimenko. It is worth remembering that the computed relative error is with respect to the Hi-Fi polyhedron model.

A nonlinear regression is accomplished on the available data and the obtained best-fitting equations are presented in the legend of the plot. These relations are quite interesting since they both agree with the 3-to-1 order of magnitude rule, already described in section 3.2.1. However, the optimized mascons results are very well represented by this trend, while the gridded approach has the already mentioned component of randomness. The 3-to-1 trend is generally followed also by the standard approach but to completely know the level of accuracy each single case must be analysed.

The good agreement of the optimized technique with this trend means that the optimization process improves the performances of the mascons approach up to its theoretical limit. Hence, to reduce the error of the optimized mascons model of one order of magnitude, N_m has to be increased by three orders of magnitude. In this way, the accuracy of an optimized mascons model can be precisely estimated knowing the accuracy of a certain reference field. Indeed, the particular fitting

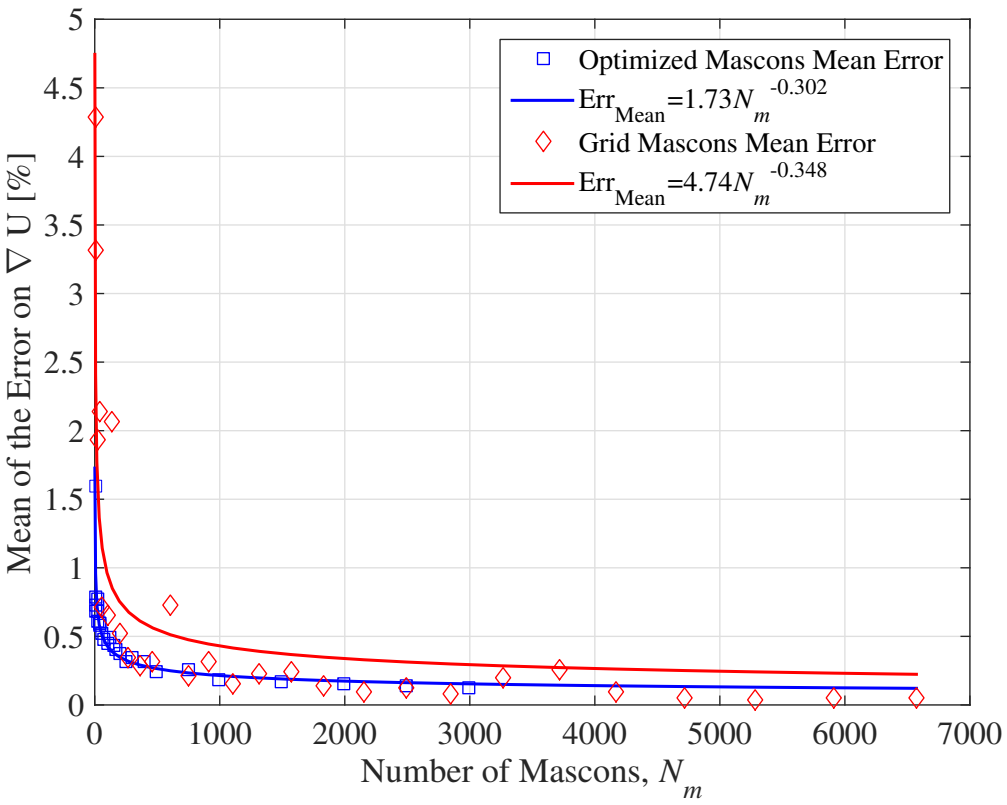

Figure 3.20: Percent error on gravitational attraction with N_m mascons on 67P.

equations shown in figure 3.20 are valid for the analysed case of the comet 67P, but they can be easily scaled for another body once the error for one N_m value is computed.

As already said, with few masses the gridded mascons is extremely dependent from the exact number of employed masses, and furthermore, the improvement due to the optimization process is remarkable. Consequently, for low N_m the optimized approach is extremely valuable and must be preferred to the standard modelling technique. On the other hand, for numerous point masses this difference tends to be small, or in practice, unreal. So, if N_m is large enough, the effort to optimize the mass distribution is not worth. This is reasonable since, when many masses are employed, the differences between distinct mass allocations are very limited.

A large number of mascons requires a longer computational time. Anyway, in this case, the needed time is always tolerable and there is no practical necessity to find a balance between accuracy and computational burden. In the current analysis, the gravitational potential and attraction

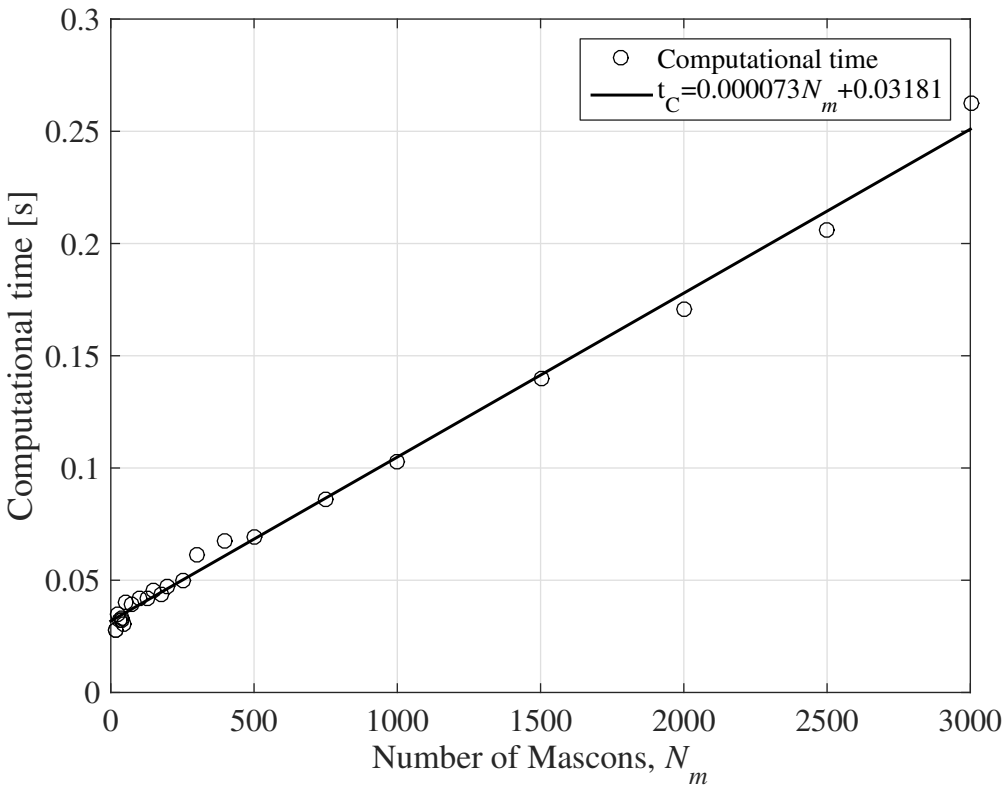

Figure 3.21: Required computational time with N_m mascons model on a 50×50 2D grid, with parallel computing techniques on a quad-core $2.50\,\mathrm{GHz}$ processor.

are computed using a MATLAB® algorithm that makes use of parallel computing techniques on a quad-core $2.50\,\mathrm{GHz}$ processor. The field is computed for a given z value on a 50×50 2D grid, thus the time to obtain these quantities on a single field point is $\mathrm{t_C}/2500$. Similarly to the polyhedron approach, there is an obvious linear relation between N_m and $\mathrm{t_C}$, which is shown in figure 3.21. These results could be used as a reference for future studies.

3.5 Optimum Lo-Fi Model

The analysis of the different gravity field models can be concluded comparing the different modelling techniques on the shape of the selected celestial bodies. In this way the optimum Lo-Fi model can be defined; it has a low fidelity with respect to the assumed Hi-Fi model, but it allows saving computational resources. For certain applications, this could be a decisive feature, and therefore, the introduction of this concept is ex-

tremely important. In practice, the optimum Lo-Fi model has an optimal balance between level of accuracy and required computational effort.

This study is carried out comparing a polyhedron model with a low number of faces, two gridded mascon models and their relative optimized versions. Actually, also an additional 2 mascons model was considered as a separate technique. However, its performances are poor and it cannot be properly compared with the other Lo-Fi models. Its range of applications is well delineated, but it is limited and out of the targets of this research work. Hence, the obtained results with $N_m = 2$ are not presented here.

In figure 3.22, the obtained data are shown by means of two different convenient statistical quantities and a useful bounding parameter. In fact, the mean and the standard deviation define the error distribution, and the maximum establishes the limits of the model accuracy, close to the surface of the body in particular. It is important to note that the error is not guaranteed to be distributed according to a *folded normal distribution*, and the actual probability density function is often unknown. Nevertheless, the mean and the standard deviation can be used to characterize the distribution of the error field independently from this information.

As a first remark, the optimization process increases the performances of the ~ 500 mascons model, while the ~ 2500 optimized mascons is not better than the equivalent gridded model. This was already pointed out in section 3.4, but is here confirmed for all the different shape models. In addition, looking at the mean and maximum values in figures 3.22a and 3.22b, the optimization algorithm works at its best with the mean of the error, in agreement with the definition of the objective function to be minimized. Furthermore, both gridded and optimized mascons approaches produce good results for non-elongated bodies, and are less effective with the oblong ones. Then, focusing on the mean of the error, the mascons approach with a large N_m produces satisfactory results, while the optimized version should be preferred if few masses are employed.

The polyhedron model with 1000 faces has higher mean values of the error, and this can be explained considering the slight shape alteration produced by a coarse discretization of the body. However, the Lo-Fi polyhedron approach performs dramatically better when the maximum value of the error is considered, and this is due to the good results of the polyhedron model in the vicinity of the surface of the body. On the contrary, the mascons approach has several problems in representing the gravitational attraction close to the singularities introduced by the

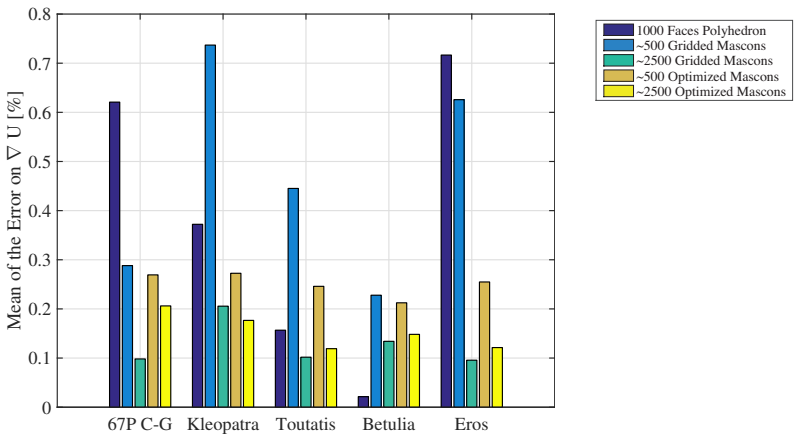

(a) Mean of the Error on ∇U.

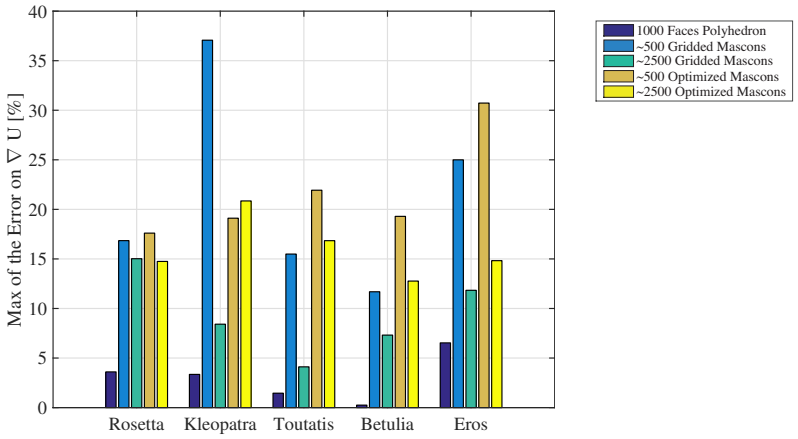

(b) Maximum of the Error on ∇U.

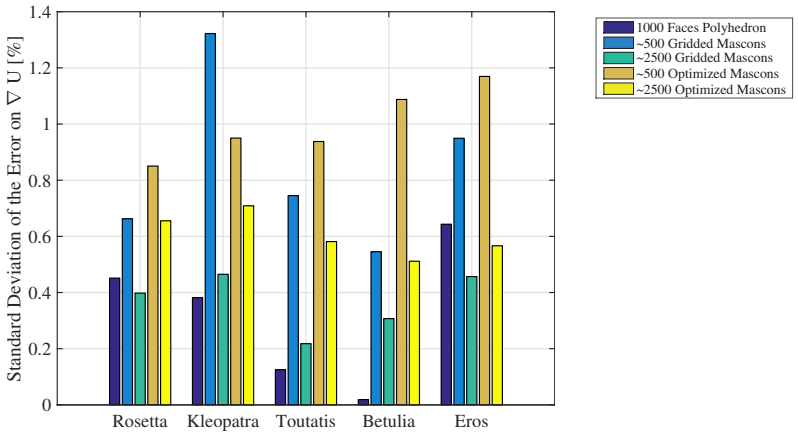

(c) Standard Deviation of the Error on ∇U.

Figure 3.22: Optimum Lo-Fi model: Statistical Analysis.

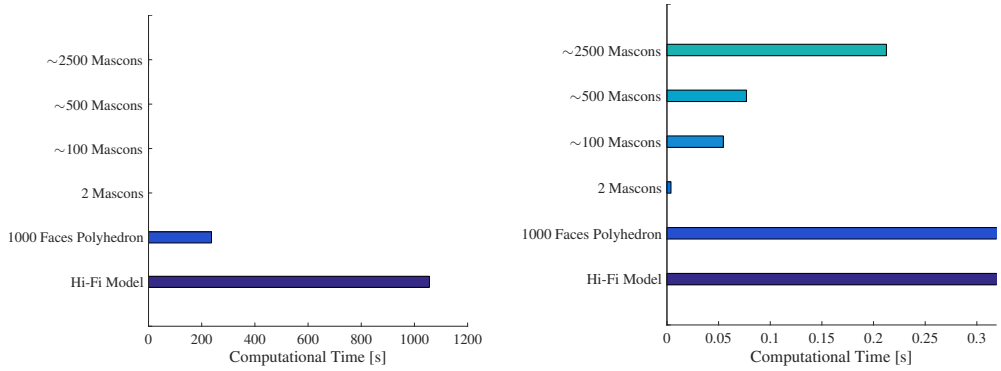

(a) Global view. (b) Detail.

Figure 3.23: Optimum Lo-Fi model: Required Computational Time on a 50×50 2D grid, with parallel computing techniques on a quad-core $2.50\,\mathrm{GHz}$ processor.

point masses. Accordingly, it produces high errors in proximity of the body. In general, if the shape of the body is not particularly modified by the scaling algorithm, the polyhedron approach with a reduced number of faces is by far the best Lo-Fi model: the asteroid 1580 Betulia is an example of this situation.

The standard deviation, in figure 3.22c, is a measure of the dispersion of the error and it is consequently influenced by the maximum value in the field, which can be considered as an outlier in the error distribution. Hence, the behaviour of the standard deviation is similar to the one in figure 3.22b, and the Lo-Fi polyhedron is the best performer in this regard. The standard deviation is anyway not large; the errors are concentrated close to the mean value and normally 90% of them is below 1%.

At this point, assuming that the shape of the body is fairly modified by the scaling algorithm, the best Lo-Fi model is a combination of a polyhedron model with few faces and an optimized mascons with a small N_m, or in alternative, a gridded mascons with many point masses. The first should be utilized close to the surface of the body and one of the latter when the distance from the centre of mass is large enough.

In figure 3.23, the computational times required by the different enhanced modelling techniques are shown and compared. They are related to MATLAB ® codes running in parallel on a quad-core $2.50\,\mathrm{GHz}$ processor. As usual, the time to obtain the different gravitational quantities on a single field point is $\mathrm{t_C}/2500$. These plots demonstrate the huge difference between the polyhedron and the mascons approach in terms of needed computational resources. However, the Lo-Fi polyhedron

model requires a tolerable time, $\mathrm{t_C} \simeq 0.10\,\mathrm{s}$, to be evaluated on single point. So, even if it is slower than the mascons approach, it is anyway preferred when the field point is in proximity of the surface of the body

The results and conclusions obtained in this chapter are then used to effectively and efficiently implement the dynamical model around an irregularly-shaped body.

Chapter 4

Rotational Dynamics of Irregularly-Shaped Bodies

The rotational state of an irregular celestial body is important to completely describe the dynamical environment in its vicinity, because of the coupling between its rotational motion and the associated close proximity orbital dynamics, which has been extensively described in section 2.4. Moreover, the understanding of the spin-vector evolution of small celestial bodies could be applied to study the formation and the chaotic events that created the Solar System. For instance, according to [25], the rotation rates distribution of near-Earth asteroids is noticeably different from the analogous distribution of Main Belt asteroids, in consequence of an excesses of fast and slow rotators, which are not so conspicuous in the distribution for the bodies in the Main Belt. Furthermore, the accurate determination of the rotational state of Potentially Hazardous asteroids could be exploited to accurately propagate their heliocentric orbital path, with the result of being more precise in the impact risk determination and related uncertainty containment. All these analyses can be performed with a model that is able to describe and simulate the rotational dynamics of an asteroid or a comet.

This model is presented in the current chapter, together with the validation of the algorithms to propagate the dynamics and to compute the external perturbations. In addition, some simulations are shown and discussed, and a sensitivity analysis to evaluate the robustness of the entire research work is considered.

At this point, it is worthwhile to note that the perturbative effect are important in the framework of this thesis, since it deals with small irregular bodies whose dynamics can be significantly perturbed by non-

gravitational torques and gravitational phenomena generated by a third body on short timescales.

4.1 Model Implementation

The developed dynamical model is based on the Euler's rotation vectorial equation (2.63). But, in order to facilitate the numerical integration, a set of three scalar ordinary differential equations is written in the rotating body-fixed reference frame, B, obtaining:

$$I_x\dot{\omega}_x + (I_z - I_y)\omega_y\omega_z = \mathrm{m}_x \tag{4.1a}$$

$$I_y\dot{\omega}_y + (I_x - I_z)\omega_x\omega_z = \mathrm{m}_y \tag{4.1b}$$

$$I_z\dot{\omega}_z + (I_y - I_x)\omega_x\omega_y = \mathrm{m}_z, \tag{4.1c}$$

where all the quantities are defined in chapter 2.

The initial conditions are specified in term of $\boldsymbol{\omega}_0 = [\omega_{0_x}, \omega_{0_y}, \omega_{0_z}]$. The rotational kinematics is propagated at the same time using equation (2.49) with initial condition expressed by $\mathbf{A}_0$ equal to the identity matrix, $\mathbb{I}^{3\times3}$, since the inertial and the body-fixed reference frames are assumed to coincide for $t = 0$.

Equations (4.1a) to (4.1c) are integrated with a variable order Adams-Bashforth-Moulton PECE solver. This is a multistep solver and it normally needs the solutions at several preceding time points to compute the solution at the current time step. The error tolerances are very stringent and the accuracy of the integration procedure is always monitored with some reference quantities.

At each iteration step of the differential equation solver the Sun-Body direction is evaluated in the inertial frame, and then rotated in the body-fixed coordinate system. Next, all the external perturbing torques are computed knowing the orientation of the body in B, and their overall contribution is represented by the vector $\mathbf{m}$. This is substituted in the set of equations (4.1), and the dynamics is propagated forward in time.

As already mentioned, the perturbations involving the interaction with the surface of the body are computed exploiting the polyhedron shape discretization. In this way, the only approximation that is made is the one of discretizing the actual shape with a polyhedron, and the obtained value is a good estimation of the real one. Moreover, the self-shadowing phenomenon can be considered with a simple analysis of the geometry of the problem. For this particular purpose, the Sun is considered at an infinite distance from the body and dimensionless.

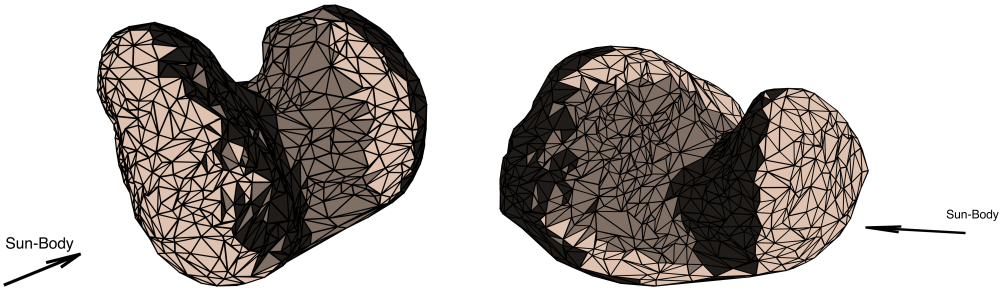

(a) Sun-Body direction along $\hat{\mathbf{x}}$. (b) Sun-Body direction along $-\hat{\mathbf{x}}$.

Figure 4.1: Shadowing algorithm output. (The illuminated faces are pale brown, the self-shadow faces are dark brown and the shadow faces are almost black. The Sun-Body direction is indicated in the figure.)

As a consequence, the shadow, being generated by a point source, is composed only by the *umbra*.

The shadowing algorithm begins detecting all the triangular faces that are not directly facing the Sun: the *shadow faces*. These are directly eliminated by the list of the possible self-shadowing region, and for them the quantity $\cos(\alpha_i)_{Sh}$, defined in section 2.5.2, is equal to 0. Then all the remaining faces are analysed; they are indicated as *self-shadow faces* if the semi-infinite vector from the centre of the face, parallel to the Body-Sun direction in the rotating frame, intersect the shape model. This is made possible with a query on the Delaunay triangulation, which is able to find the intersections between a vector and the mesh of a body. $\cos(\alpha_i)_{Sh}$ is equal to 0 also for the self-shadow faces. Only the remaining *illuminated faces* are then used to compute the resulting solar radiation pressure and YORP torques using equations (2.81) and (2.82). This algorithm is executed at each integration step and it makes use of parallel computing techniques improving the computational speed of the whole model. An example of the shadowing algorithm output is shown in figure 4.1.

The other two perturbative effects, third body gravitational effect and dissipation of energy, depends from the inertia properties of the body. These are constant quantities and their assumed values were presented in section 2.3.2.

4.1.1 Dynamic Quantities

The results of the dynamical simulations are contained in a matrix composed by the rotational state vector, $\boldsymbol{V}_{Rot}(t) = [\bar{\mathbf{A}}(t), \boldsymbol{\omega}(t)]^{\mathrm{T}}$, evaluated

at each integration step. Here, $\bar{\mathbf{A}}$ is a row vector containing all the 9 components of the rotation matrix, $\mathbf{A}$. Thus, the time evolution of the Euler angles, $\phi(t)$, $\theta(t)$ and $\psi(t)$, and of the angular velocity, $\omega_x(t)$, $\omega_y(t)$ and $\omega_z(t)$, is immediately available. However, to have a better insight on the rotational dynamics of irregularly-shaped bodies, some derived dynamic quantities are introduced and described.

Angular momentum, $\mathbf{h}$, and kinetic energy, T, are the first and the simplest to be analysed. If there is no dissipation of energy and no torque is applied these two quantities must be constant, and in the inertial reference frame I, the angular momentum is a fixed vector. This is extremely helpful, since it can be used to verify the accuracy of the model in the torque-free motion, or to better understand the energy and dynamic effect of the perturbations when they are applied. They can be easily obtained from the angular velocity vector as:

$$\mathbf{h} = \mathbf{I}\boldsymbol{\omega}, \tag{4.2}$$

and

$$T = \frac{1}{2}\boldsymbol{\omega}\mathbf{I}\boldsymbol{\omega}. \tag{4.3}$$

The angular momentum vector can be easily evaluated in the inertial frame by means of the rotation matrix, $\mathbf{A}$.

Yet, two other quantities can defined: the obliquity δ and the dynamic inertia I_D. The former describes the direction of the angular momentum vector in the inertial reference: it is the angle between the normal to the orbital plane, $\hat{\mathbf{z}}_I$, and the angular momentum, $\mathbf{h}_I$. The latter is another constant of the unperturbed motion and it can be related with the non-principal rotation mode of the body.

The obliquity δ can be obtained with simple geometrical considerations on the angular momentum vector expressed in the inertial frame and $\delta \in [0, \pi]$.

The dynamic inertia I_D can be computed from equation (4.2) and (4.3) as:

$$I_D = \frac{\|\mathbf{h}\|^2}{2T}, \tag{4.4}$$

it has the physical dimensions of a moment of inertia, and if the body is in principal axis rotation state, the dynamic inertia is equal to the related principal moment of inertia. I_D is an important quantity because it illustrates the actual rotational state of the body.

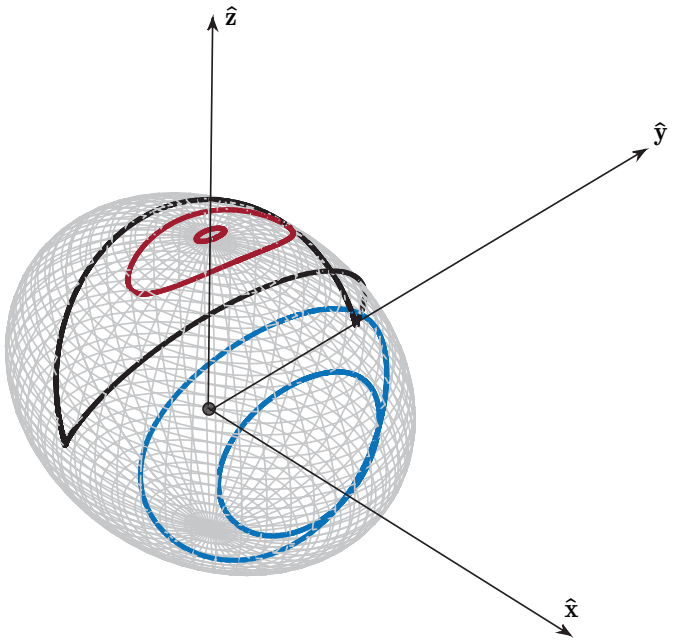

Figure 4.2: Polhodes on Poinsot's ellipsoid for a torque-free motion.

4.2 Model Validation

The reliability and the accuracy of the solutions obtained with the developed dynamical model is an important aspect that has to be assessed. Several validation tests are here presented and compared with simple and known results. Each perturbative contribution is taken into account individually, and its results are computed using the dynamical model that includes only the specific perturbation considered.

4.2.1 Torque-Free Motion

The first and simplest condition that can be simulated to verify the accuracy of the whole dynamical model is the rotational motion without external torques applied. In this case, the geometrical Poinsot's construction can be exploited to validate the equations of motion and integration algorithm. In addition, the angular momentum and the kinetic energy must be constant and their values are monitored throughout the integration process.

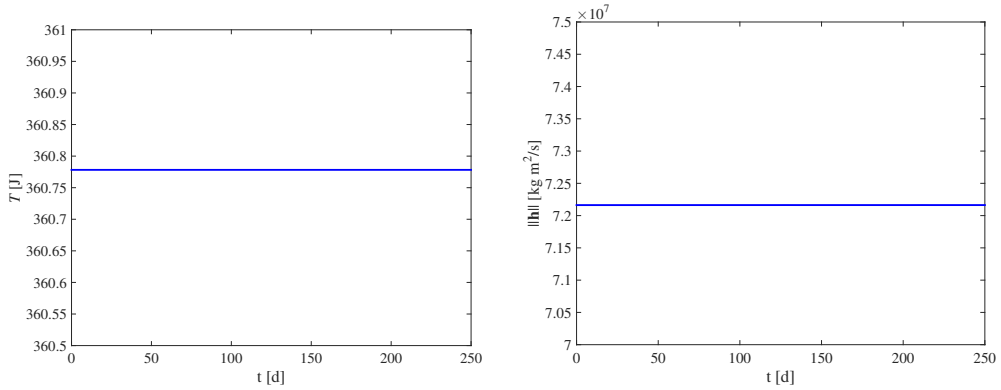

(a) Kinetic Energy, T.

(b) Angular Momentum, $\|\mathbf{h}\|$.

Figure 4.3: Kinetic energy and angular momentum for a torque-free motion.

In figure 4.2, the Poinsot's Ellipsoid is shown with some polhodes related to different initial conditions for the angular velocity. In fact, the polhode is the curve produced by the angular velocity vector on the inertia ellipsoid, and in this case, the blue curves are for motion closer to the minimum inertia axis, $\hat{\mathbf{x}}$, while the red ones are connected with the dynamics in the vicinity of the maximum inertia axis, $\hat{\mathbf{z}}$. Instead, when the angular velocity is initially very close to the intermediate inertia axis, $\hat{\mathbf{y}}$, the black polhode is obtained. It is here confirmed the stable rotation state in the region of the minimum and maximum inertia axes, whereas a minor deviation from the $y-$axis would cause a dramatic departure from the original condition. In figure 4.3, the magnitude of the angular momentum and the kinetic energy are correctly constant for a $250\,\mathrm{d}$ simulation without external perturbations. Obviously, also the components of the angular momentum vector in the inertial reference frame are constant.

The dynamical model is correctly working, but now all the perturbative effects have to be validated, to prove the correctness of the whole algorithm.

4.2.2 Third Body Gravitation

The third body gravitational effect is influenced by the relative orientation of the irregular body with respect to the Sun. As already said, this perturbation is null if one principal inertia axis is aligned with the Sun-Body direction. Hence, to validate this perturbative contribution the rotation of the body is controlled in order to have insightful results. For

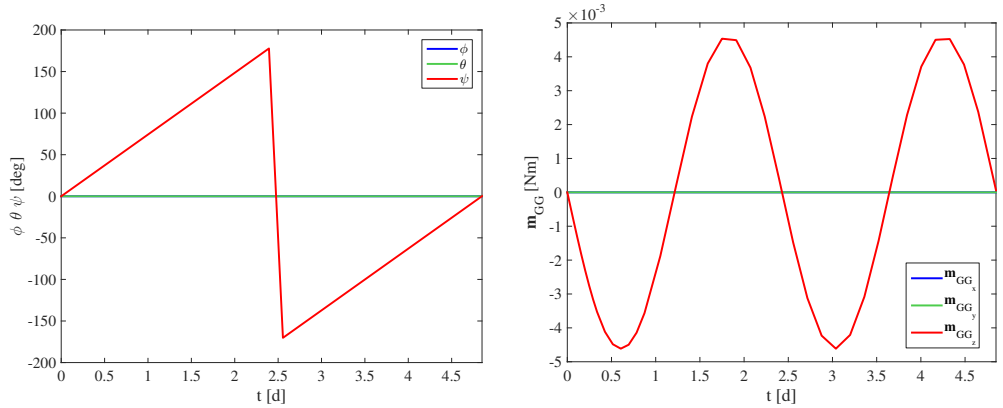

(a) Euler Angles.

(b) Gravity gradient torque, $\mathbf{m}_{GG}$.

Figure 4.4: Validation of third body gravitational effect.

example, if the rotation period is equal to the revolution period of the celestial object around the Sun, and at the initial time, one principal inertia axis is directed towards the Sun, the gravity gradient torque is always equal to zero. This condition has been tested and the resulting torque was practically null, with a numerical value below $1.50 \times 10^{-11}\,\mathrm{Nm}$ for a $250\,\mathrm{d}$ simulation.

The torque due to the presence of the third body was also computed and it was averaged over one full rotation of the comet 67P on its axis and over one full revolution as it orbits the Sun. This was repeated for different initial obliquity values, and in all these cases, the averaged perturbing torque had a value below $1 \times 10^{-12}\,\mathrm{Nm}$, confirming what has been said in section 2.5.1.

In figure 4.4, the rotational dynamics of 67P has been integrated for one rotation period, starting with the minimum inertia axis aligned towards the Sun. The spin axis is assumed to be aligned with the maximum inertia axis, and consequently, the body makes one full rotation around $\hat{\mathbf{z}}$, figure 4.4a. As expected, the gravity gradient torque acts only on the spin axis and it is equal to zero for $\psi = [0°, 90°, 180°, 270°, \dots]$, i.e. when a principal inertia axis is aligned with the Sun-Body direction.

4.2.3 Solar Radiation Pressure and YORP

The solar radiation pressure and the YORP effect are validated together, since their effect can be compared. They can also be considered as two different appearances of the same physical phenomenon due to the solar irradiation. The YORP effect and the reflected solar radiation pressure

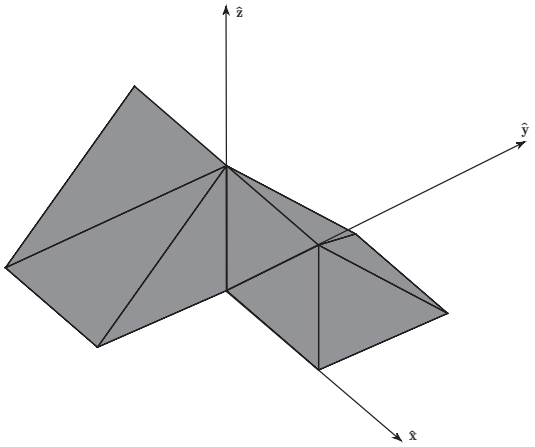

Figure 4.5: Rubincam's Wedges.

acts normally to the surface direction, while the absorbed radiation generates a force in the Sun-Body direction. As a first assessment, these torques can be applied on simple geometries as spheres and ellipsoids.

On the sphere, there is no radiative torque because the components in the normal direction point to the centre of mass: they have no lever arm. The components in the Sun-Body direction are symmetric: their global contribution is equal to zero. In this case the algorithm produces meaningful results with a torque always below $1 \times 10^{-16}\,\mathrm{Nm}$.

The ellipsoids were also employed to test the code, similarly to what has been done to validate the third body gravitational effect. In one case, the ellipsoid had its longest axis aligned with the Sun-Body direction for one revolution period; the obtained torque was correctly equal to zero, $\sim 1 \times 10^{-15}\,\mathrm{Nm}$, for symmetry reasons. In another test, the rotational dynamics of the axially symmetric ellipsoid has been integrated for one rotation period around the $z-$axis. Even if the physical reason is totally different, the result had the same trend of the analysis shown in figure 4.4, which can be explained considering the symmetrical shape of the ellipsoid.

The validation procedure was then continued exploiting the averaged quantities over one full rotation and over one full revolution of the body. The results are shown in figure 4.6 for the YORP effect and in figure 4.7 for the solar radiation pressure. They are obtained evaluating the perturbing torque for every 10° of rotation and revolution; these values are then averaged and saved for different values of obliquity. Two particular components of the torque, $\mathbf{m}_z$ and $\mathbf{m}_\delta$, are used to display

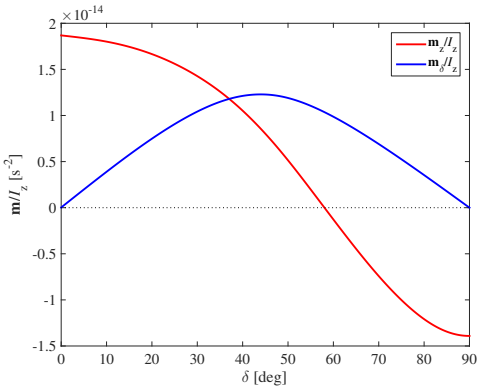

(a) Rubincam's Wedges, $(0° - 90°)$.

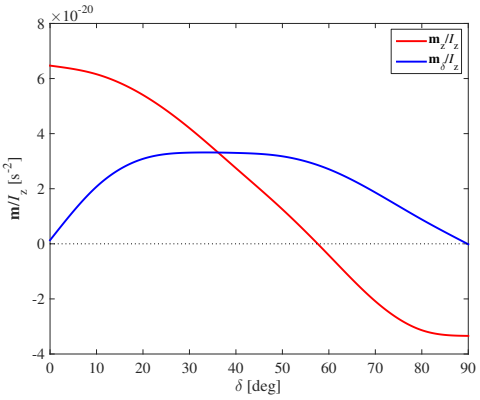

(b) 433 Eros, $(0° - 90°)$.

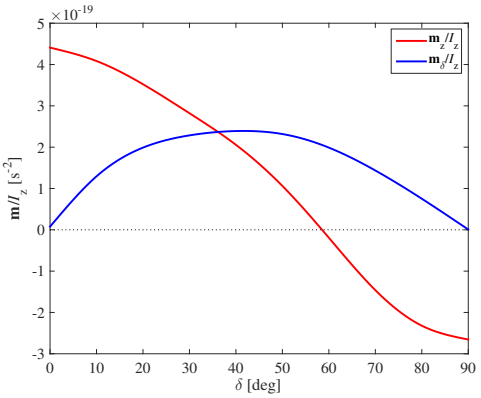

(c) 1580 Betulia, $(0° - 90°)$.

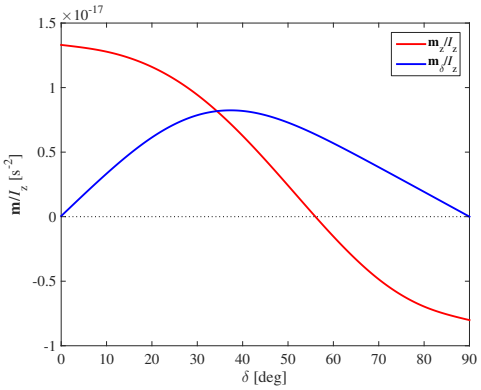

(d) 4179 Toutatis, $(0° - 90°)$.

Figure 4.6: Validation of YORP effect.

the outcomes. $\mathbf{m}_z$ is the torque along the spin axis which changes the rotation rate, while $\mathbf{m}_\delta$ acts to change the obliquity. For the current analysis the spin axis is assumed to coincide with the axis of maximum inertia, $\hat{\mathbf{z}}$. The torques are normalized with respect to the maximum moment of inertia, I_z.

The behaviour of the YORP effect is very similar for all the asteroids; it is almost independently from the shape of the body. Moreover, all the bodies are influenced by this perturbing torque similarly to the *Rubincam's wedges*, shown in figure 4.5. This simple but insightful shape was introduced by David Rubincam to explain the radiative torques on irregular celestial bodies. This object has the "windmill" asymmetry that is needed in order to see the effect of the YORP torque; axisymmetric figures are not influenced by this perturbation on a long period of time.

The component in the direction of the normal to the surface of the solar radiation pressure obviously behaves like the YORP effect, but

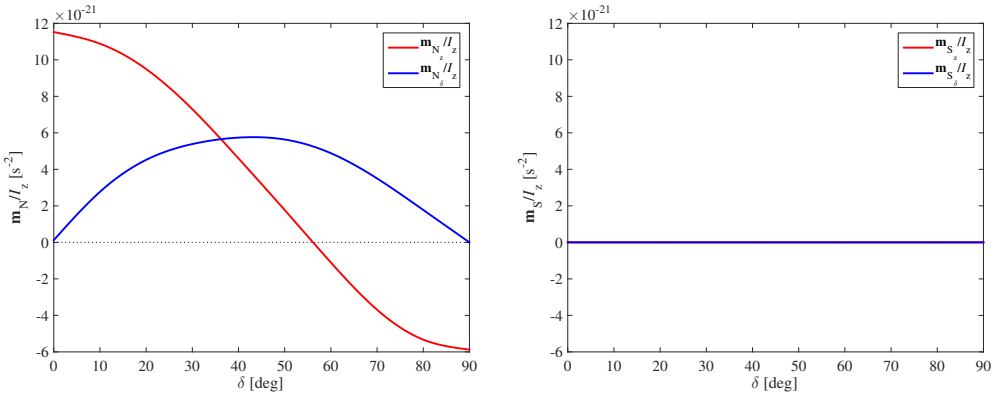

(a) Normal Direction, $\hat{\mathbf{n}}$. (b) Sun-Body Direction, $\hat{\mathbf{s}}$.

Figure 4.7: Validation of Solar Radiation Pressure effect for 433 Eros, $(0° - 90°)$.

the component along the Sun-Body radius vector averages to zero, as explained in section 2.5.3.

These results agree with the theoretical formulation of this phenomenon, and hence, the algorithm is validated. However, it is interesting to discuss a bit more in detail about all these conclusions.

The first thing that can be noted is the small contribution of these perturbing torques, due to the small amount of momentum carried by photons. In spite of that, the outcome must be considered coherently with the astronomical time scales, and in this perspective, the body's rotation rate can be substantially perturbed by these radiative effects. Certainly, the Rubincam's wedges are the most influenced by the thermal torques, because of their shape to enhance the contribution of these perturbations. The value of the perturbing accelerations indicates the amount "radiative-windmill" asymmetry of each shape.

Then, comparing figure 4.7a and figure 4.6b, the secular contribution of the YORP is larger than the one of the solar pressure. The reason is that the majority of the incident solar radiation is absorbed by the celestial bodies, since they are usually dark. However, the absorbed radiation has effect along $\hat{\mathbf{s}}$; thus, it perturbs the body only with a non-secular contribution. The emitted thermal photons are connected with the incident absorbed energy, and as a consequence, the low albedo of the actual celestial bodies determine the prevalence of the YORP effect over the solar radiation pressure for long time scales.

It is worth noting that these torques are independent of the sense of rotation and revolution of the celestial object. Furthermore, for all the bodies $\mathbf{m}_z$ is at its maximum when the obliquity is $\delta = 0$, i.e. the

body's angular velocity is perpendicular to the orbital plane. Later, the spinning torque decreases as δ increases, and for $\delta >\sim 55^\circ$ the torque becomes negative. Hence these objects spins up when the Sun lies in the equator, but spins down when the Sun-Body direction tends to be parallel to the rotation axis. $\mathbf{m}_\delta$ is positive between 0° and 90° and it is null at the endpoints of this interval. Therefore, this radiative torque tends to increase the rotational speed and the obliquity of the object; then, when $\delta \simeq 55^\circ$, it starts to slow it down. Consequently, irregular celestial objects may be constantly speeding up and slowing down with the YORP cycle, or tumbling.

When $\delta \in [90^\circ, 180^\circ]$, according to [39], $\mathbf{m}_z$ is positive for $\delta <\sim 135^\circ$, but becomes negative and the body spins down for δ greater than 135°.

4.2.4 Energy Loss

The dissipation of energy influences only non-principal rotation states, which must be simulated to validate this contribution. The motion in presence of this effect tends to the condition of minimum energy, with the body rotating around the maximum inertia axis. Nevertheless, the analysed torque is extremely small, and to perform the validation test, its value has been arbitrarily multiplied by the constant value 1×10^{18}. This assumption does not affect the meaning of the simulations but allows running them in a reasonable time. The obtained results are shown in figure 4.8.

These images prove the tremendously small contribution of the energy loss effect that, despite the arbitrary coefficient that is used in this simulation, need more than 3000 years to completely damp the nutational motion. This value is compatible with the expression for the nutational damping time in [48], which estimate a value in the order of $1 \times 10^3\,\mathrm{y}$, taking into account the scaling constant currently employed. In this simulation, the energy loss is remarkably slow because the angular velocity is small. This perturbation have a stronger effect on fast-spinning celestial objects, which have a real damping time in the order of $1 \times 10^7\,\mathrm{y}$.

In figure 4.8c, it is evident the dissipation of the nutational dynamics. In fact, the motion begins where is the green dot and slowly tends to the principal axis rotation state around $\hat{\mathbf{z}}$, red dot in the plot. Moreover, the Poinsot's ellipsoid tangent to the polhode is evidently shrunk between the initial and the final time of the simulation; this is representing the decrease of the Kinetic energy, clearly shown in figure 4.8d. Also the

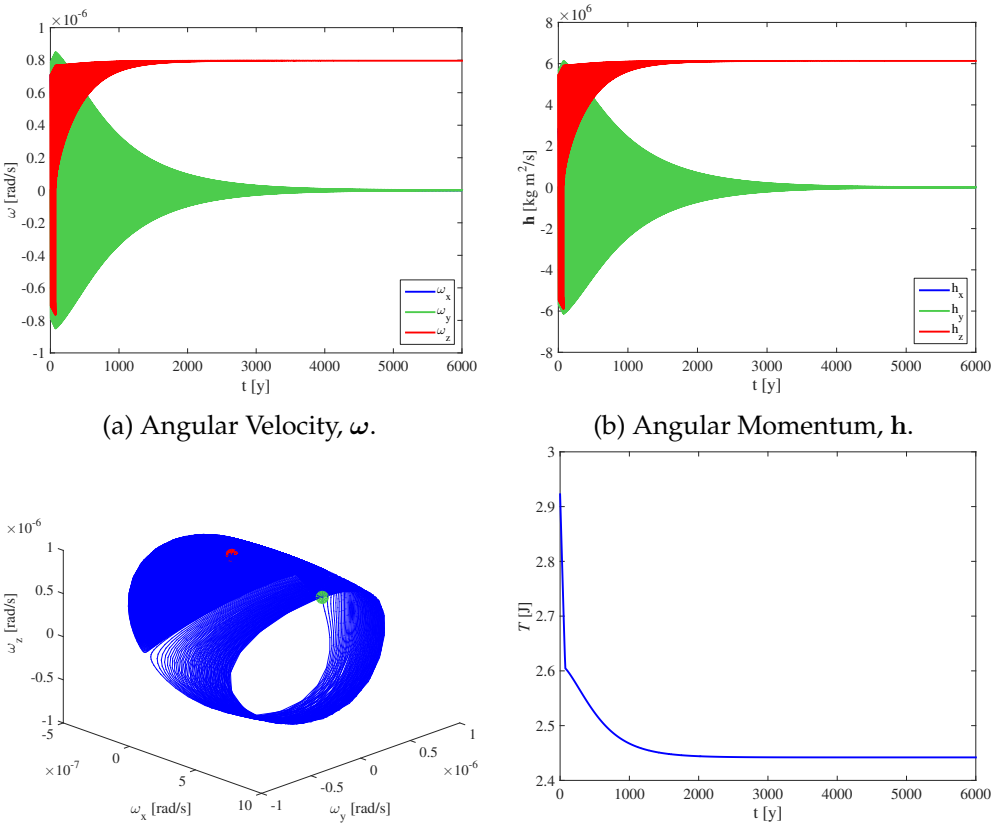

(a) Angular Velocity, $\boldsymbol{\omega}$.

(b) Angular Momentum, $\mathbf{h}$.

(c) Evolution of the Polhode.

(d) Kinetic Energy, T.

Figure 4.8: Validation of dissipation of energy effect.

angular velocity and the angular momentum, evaluated in the body-fixed frame B, display the correct behaviour of this perturbative effect.

When the pure spin state is reached the dissipation of energy does not influence the motion anymore and the dynamics is stable. With these results, the algorithm is validated.

The whole rotational dynamics model has been validated and the accuracy of the simulations has been assessed. In addition, the values of the dynamic quantities are always monitored to guarantee the fidelity of the results.

4.3 Sensitivity Analysis

The physical interactions of a small irregular celestial object with the environment are dependent on its shape and inertia properties, which

must be as accurate as possible, in order to correctly simulate the real dynamics. However, sometimes they are not available with the desired level of uncertainty, and it is reasonable to wonder if the models can still be used to study and understand the motion of these not well known astronomical objects. For this reason, a sensitivity analysis has been carried out, in such a way that the uncertainties in the input data are correlated to the uncertainties in the output of the model and the robustness of the model can be rationally estimated.

The study that is here presented is applied to uncertainties in the mass determination, in the shape model and in the rotational state of the selected celestial body. Basically, the real values that are used in this thesis, reported in sections 2.3.2 and 2.4.7, are arbitrarily modified according to the some tolerance intervals. Then, fixing all the other conditions, different simulations are executed and compared. The dynamics is integrated for one orbital period of the irregular object around the Sun and the results are confronted exploiting simple and effective quantities, like the dynamic inertia, I_D, and the obliquity, δ.

Realistic values for typical uncertainty intervals are present in the literature, even though a unique characterization does not exist. For example, in [20], the inertia properties are usually determined within 5% and 40% of accuracy; here the mass is assumed to have a tolerance of $\pm 30\%$. For what concern the shape model, the typical error is about $10 - 50\%$, according to [20, 36]; in the current analysis, the polyhedron model is reshaped between an extremely Lo-Fi model, ~ 250 faces, and the Hi-Fi model, with a resulting uncertainty on the shape related quantities of $\pm \sim 15\%$. Finally, considering the rotational state, the rotation period is commonly determined with a good accuracy, while the orientation of the spin axis has often a tolerance of some degrees [1]. Hence, in this sensitivity analysis, the magnitude of the angular velocity is maintained constant and the initial spin axis direction is allowed to vary within $\pm 5^\circ$.

4.3.1 Uncertainty in Mass Determination

The sensitivity analysis on the mass of the body is shown in figure 4.9, where the obliquity and the dynamic inertia are normalized with respect to their respective values computed at $t = 0$. This is necessary since each simulation has a different dynamic inertia, and the absolute results would be difficult to compare. The object that is used in this study is the asteroid 433 Eros.

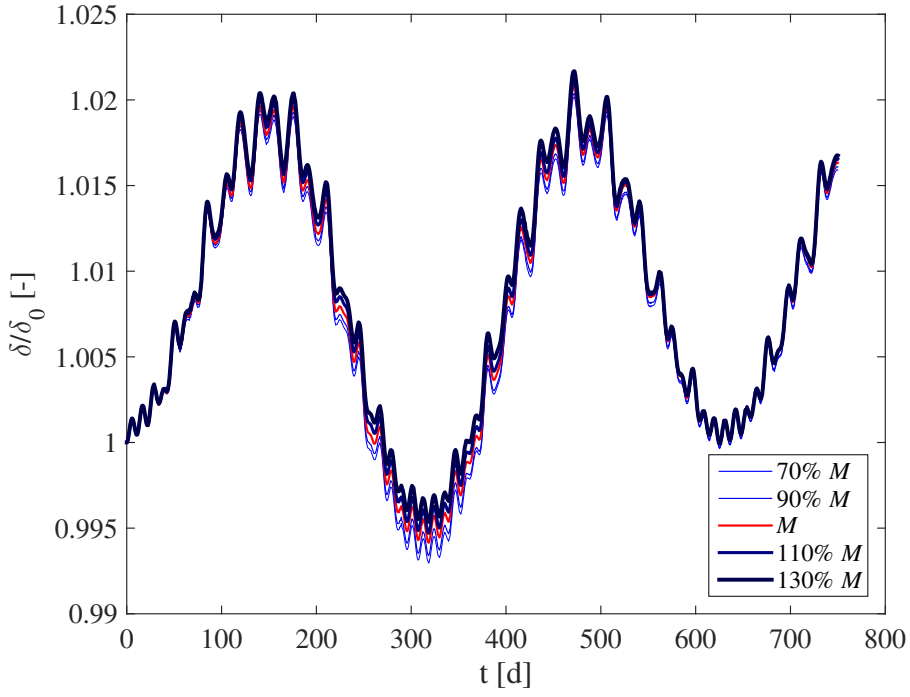

(a) Obliquity, δ/δ_0.

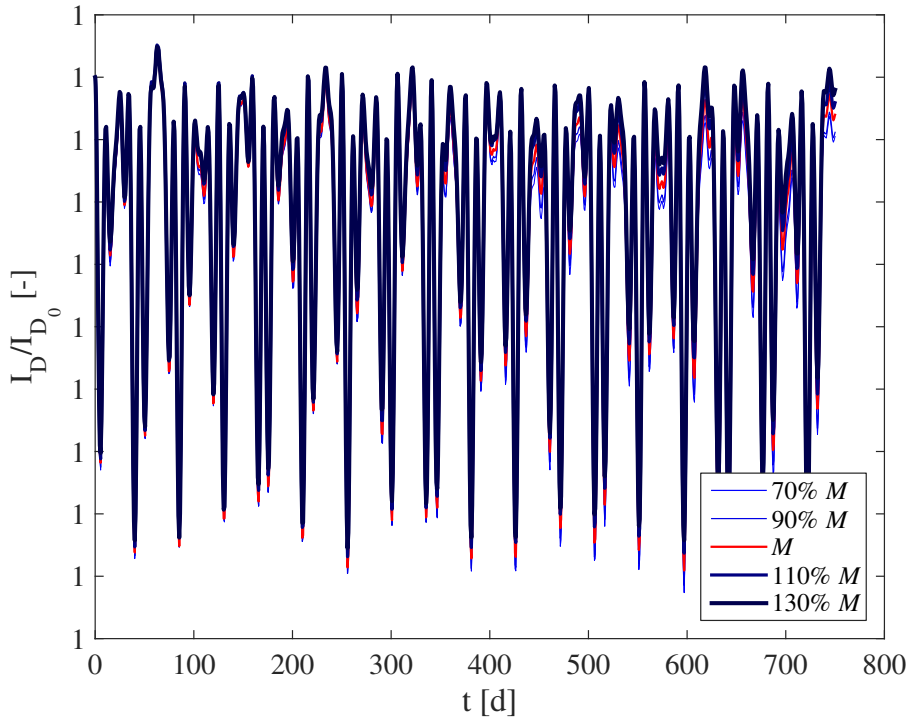

(b) Dynamic Inertia, I_D/I_{D_0}.

Figure 4.9: Sensitivity analysis with uncertainty on the mass value for 433 Eros.

From these plots is evident that the uncertainties in mass determination do not significantly affect the propagation of the perturbed rotational dynamics for an irregular celestial body. In fact, in all the different simulations the motion remain very close to the real one, red line, and the evolution of the represented quantities always follows the same trend. This result makes sense, since the perturbative effects are identical for all the tested mass values, and obviously, only the acceleration levels are different. Accordingly, the behaviour of the heavier asteroids is opposite to the one of the objects with a smaller mass, with the real case bounded between the two opposite scenarios.

4.3.2 Uncertainty in Shape Determination

The sensitivity analysis for the different shapes is performed for 216 Kleopatra and the results for the relative values of the dynamic quantities are shown in figure 4.10.

In this case, the differences between the different analysed resolutions are larger than those in the previous section for the mass. Here, the different shapes have different interactions with the perturbations, and thus, the dynamical evolutions follow slightly separate trends. However, this gap is not so wide and the propagation of the rotational motion is robust enough with respect to the errors in the shape determination. Clearly, the results are more similar to the Hi-Fi model, pale blue line, if a large number of faces is employed, black thick curve. Nevertheless, even the extremely Lo-Fi model, red thin curve, stays in the vicinity of the general behaviour, proving that a rough estimation of the perturbative effects can be accomplished with a coarse shape discretization.

It is worthwhile to point out that, in this analysis, only the perturbation acting on the surface, e.g. YORP and solar radiation pressure, are influenced by the shape model. This is true if the inertia properties are assumed to remain unchanged between the different simulations, but honestly, mass and moments of inertia are often derived from the shape of the object, and a broad tolerance interval on the geometry could determine a large uncertainty on the mass. So, it is probably that the results presented in figures 4.9 and 4.10 should be considered together; anyhow, the model is still able to produce acceptable results with the errors on both shape and inertia.

This aspect is very important, because numerous minor celestial objects are still poorly described and the techniques to characterize a body are far from being completely reliable, despite their performances have

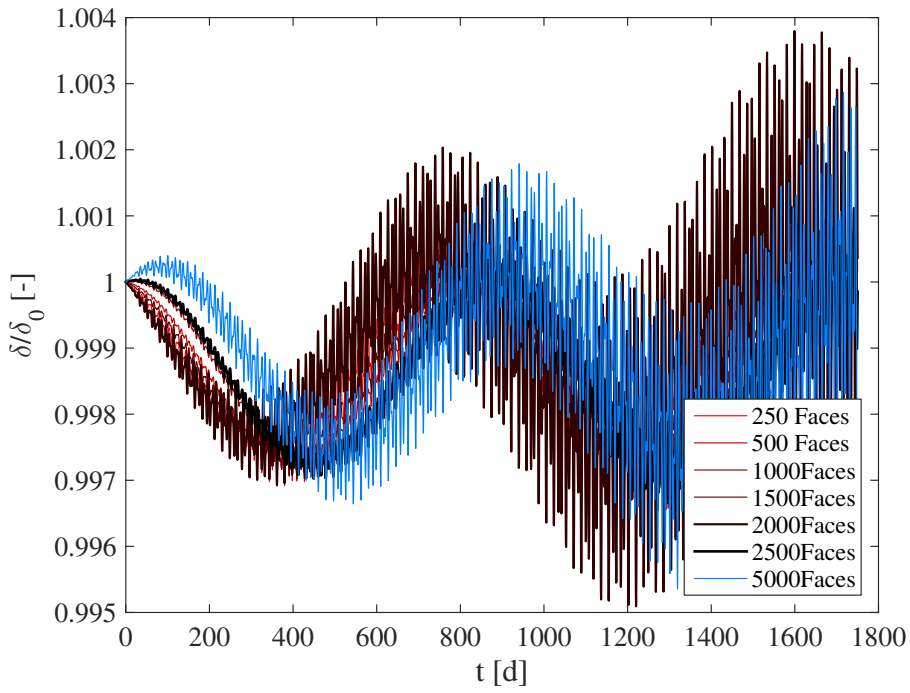

(a) Obliquity, δ/δ_0.

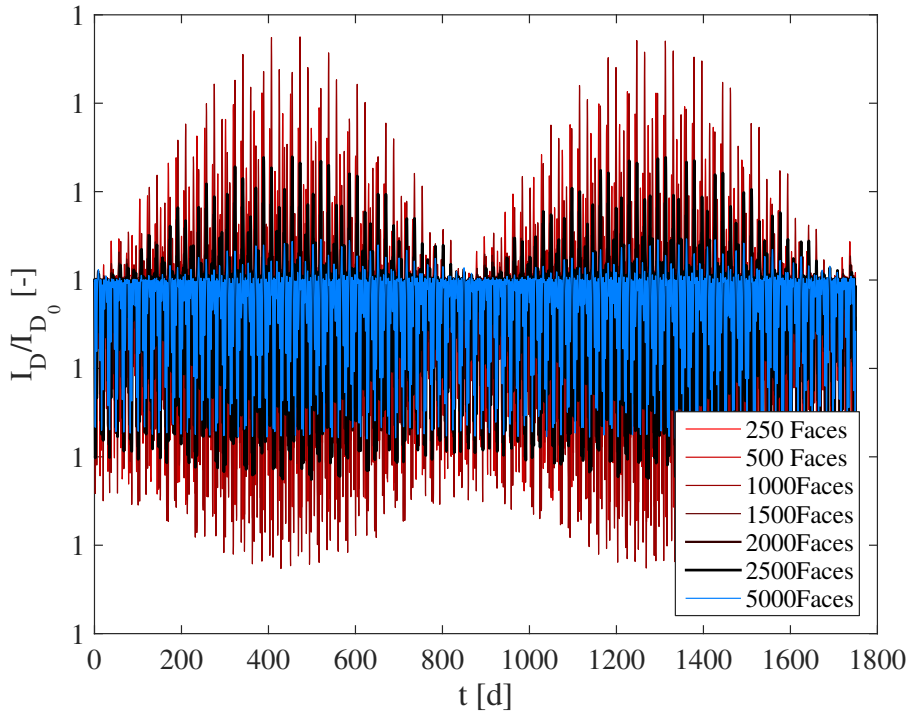

(b) Dynamic Inertia, I_D/I_{D_0}.

Figure 4.10: Sensitivity analysis with uncertainty on the shape model for 216 Kleopatra.

improved in recent years. Consequently, it is possible to have a global overview of the rotational dynamics for an asteroid or a comet using only a preliminary estimation of its inertia and shape properties. For certain practical applications, e.g. preliminary dynamics determination and propagation, the error remains below a tolerability threshold and the results can be effectively exploited.

4.3.3 Uncertainty in Rotational State Determination

The rotational state of the asteroid 4179 Toutatis is well known but variable in time, since this body is in a complex non-principal rotation state and the angle between the angular velocity vector and the minimum inertia axis varies between $21.90°$ and $20.16°$. This sensitivity analysis is applied to this object and can have a dual meaning. In fact, the uncertainty in the direction of the spinning axis can be interpreted as: the possible error in the rotation state determination for a generic asteroid; the possible dynamical evolution of Toutatis if a space probe rendezvouses with it at a certain $t = \bar{t}$, which is different from the scheduled time, and thus, the mission must be correspondingly modified.

The outcomes are presented in figure 4.11, where the reference spinning axis direction is $21°$ tilted with respect to $\hat{\mathbf{x}}$, corresponding to $40°$ of initial obliquity δ_0. It is important to remember that the assumed uncertainty value is $\pm 5°$.

Comparing the effects on the propagation of the dynamics, the ones due to the errors on the rotation axis direction are stronger than those related with the inaccuracies on mass and shape determination. Nevertheless, the gap between the different simulations is still limited and the trends of the analysed quantities are remarkably similar.

For $t = 0$ one principal axis is aligned with the Sun, i.e. there is no gravity gradient torque, and the dissipation of energy can be neglected. So, taking into account only the radiative perturbations, the examples with a lower obliquity experiences a larger spin torque, $\mathbf{m}_z$, and their dynamics is faster; then their evolution is shifted on the left in figures 4.11a and 4.11b.

Now, focusing on the initial behaviour of the obliquity, the different simulations are very similar. The explanation is easy, considering that $\delta_0 \sim 40°$ and remembering the averaged trend of $\mathbf{m}_\delta$ in figure 4.6. In fact, around that obliquity value, the tilting torque has a stationary point and the differences between the different cases are limited. However, as can

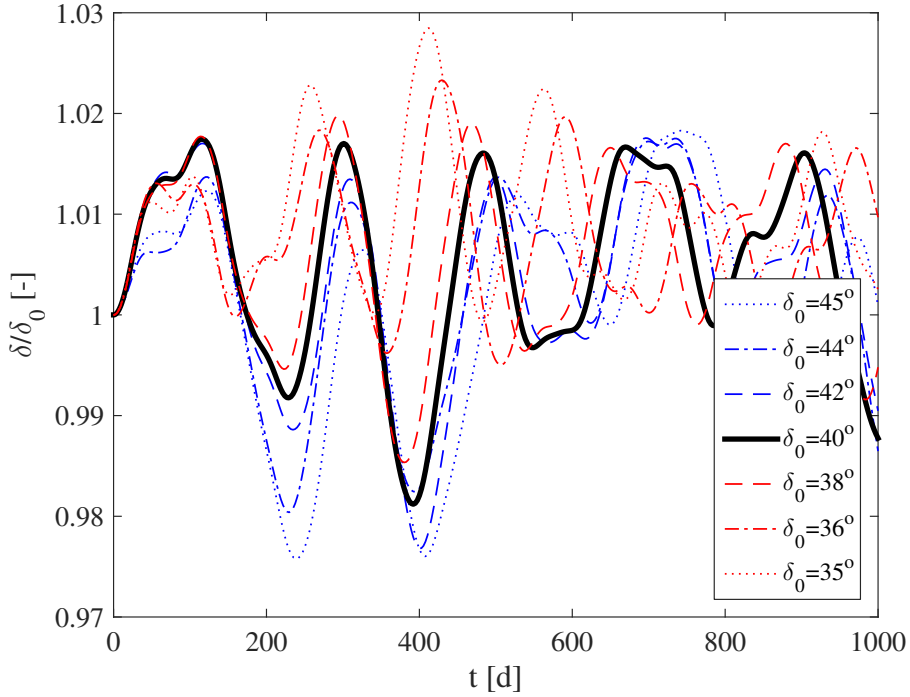

(a) Obliquity, δ/δ_0.

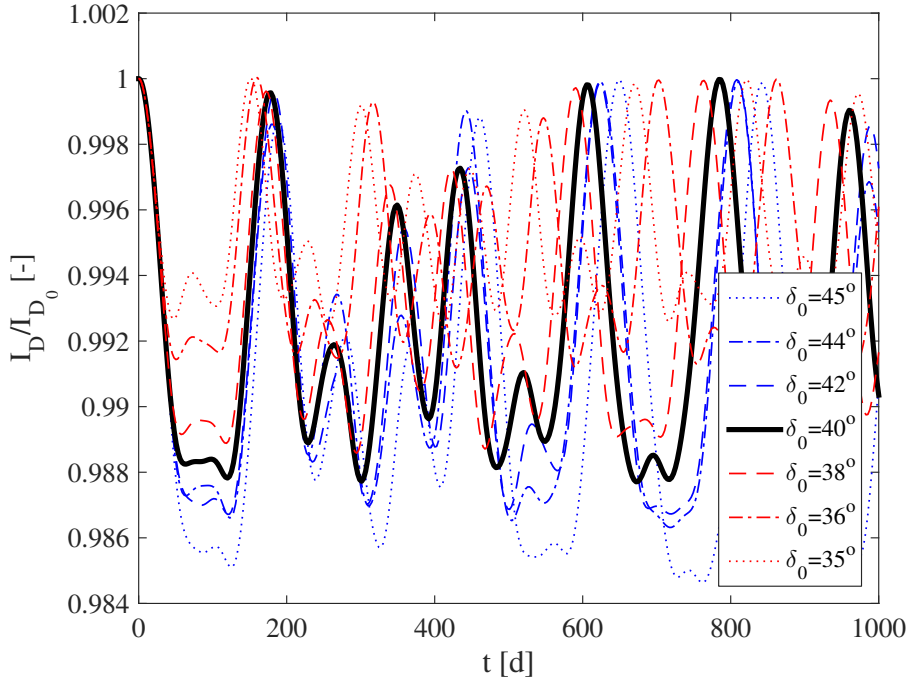

(b) Dynamic Inertia, I_D/I_{D_0}.

Figure 4.11: Sensitivity analysis with uncertainty on the rotational state for 4179 Toutatis.

be understood examining figure 4.11a, for $\delta_0 = 45$, $\mathbf{m}_\delta$ is smaller than the same torque component evaluated for $\delta_0 = 38$.

These are the only direct considerations that can be done on the direct influence of the perturbations on the dynamics of the body because, as soon as the motion evolves, all the perturbative effects act together, and it is difficult to have additional conclusions.

In general, also in the case of uncertainties in the rotational state determination, the model is robust enough, and the dynamic quantities are bounded in the vicinity of the reference solution, without any chaotic divergence. As already said, the errors are larger than those obtained in the previous two sensitivity analyses, but they are still tolerable and preliminary studies can be conducted with the necessary margins of safety.

The conclusions and the results discussed in this section are only related with the particular conditions that have been considered. Notwithstanding, they allow having a better overview on the rotational dynamics of irregularly-shaped bodies and they provide some reference values to assess the robustness of this dynamical model. Globally, with the assumed values for the tolerance intervals and with the examined initial conditions, the algorithm is reliable and produces acceptable results even if the physical model of the body is not well known.

4.4 Magnitude of Perturbing Torques

The algorithm that propagate the rotational dynamics of the selected bodies evaluates the perturbing external torques and use their values in the equation of motion (4.1). These phenomena characterize the rotational dynamics with their particular behaviour, yet the magnitude of these torques is another important aspect that was not discussed. The magnitudes of the different perturbation are listed in table 4.1 for the reference irregular celestial objects. These values are obtained computing the norm of the root mean squares of the torques components, evaluated along one orbital period. The simulations are performed using the real rotation state of the selected objects as initial condition.

The gravity gradient torque is the largest perturbative effect, but as already said, it has not a secular effect. The periodic fluctuations in the dynamics of the body are mainly due to this component. The dissipation of energy is the least influencing term and its contribution is practically negligible in the short period. The big and fast spinning asteroids

Table 4.1: Magnitude of perturbing torques.

(a) Third body gravitation and solar radiation pressure.

		$\|\mathbf{m}_{GG}\|$ [N m]	$\|\mathbf{m}_{SRP}\|$ [N m]
67P	C-G	7.87×10^{3}	7.86×10^{2}
216	Kleopatra	3.11×10^{13}	2.30×10^{7}
4179	Toutatis	7.25×10^{4}	3.90×10^{2}
433	Eros	4.68×10^{9}	5.62×10^{5}
1580	Betulia	3.29×10^{5}	3.12×10^{3}

(b) YORP and dissipation of energy.

		$\|\mathbf{m}_{YORP}\|$ [N m]	$\|\mathbf{m}_{D}\|$ [N m]
67P	C-G	5.06×10^{2}	3.35×10^{-2}
216	Kleopatra	2.16×10^{7}	7.44×10^{12}
4179	Toutatis	2.48×10^{2}	2.20×10^{-3}
433	Eros	5.58×10^{5}	2.26×10^{6}
1580	Betulia	2.12×10^{3}	8.44×10^{2}

Kleopatra and Eros are the only exceptions to this last consideration. In fact, the large inertia properties and the rotation state of these two bodies determine a considerable torque due to the internal friction. In addition, the two perturbations due to solar radiation affect mainly the rotation rate of asteroids a few kilometers in diameter [4]. Therefore, Kleopatra and Eros have a frictional torque that is some order of magnitudes larger than the YORP and the solar radiation pressure effects.

The magnitude of the two radiative torques is comparable, since the emitted and the incident radiations are connected by the thermal balance of the body. The emitted energy is a fraction of the whole incident flux, and consequently, the YORP produces a torque that is slightly smaller than the one due to the solar radiation pressure. However, the secular effect is principally related with the YORP effect, as explained in section 4.2.3.

In figure 4.12, the evolution of the perturbing torques for one rotation period of the asteroid 1580 Betulia is plotted. In this simulation the actual rotational state of the asteroid is propagated; so, the angular velocity is $\|\boldsymbol{\omega}\| \simeq 2.84 \times 10^{-4}\,\mathrm{rad/s}$ and it is almost aligned with the maximum inertia axis. The rotation period is $\mathrm{T}_{2\pi} \simeq 6\,\mathrm{h}$ and the root mean square values presented in table 4.1 agree with these figures.

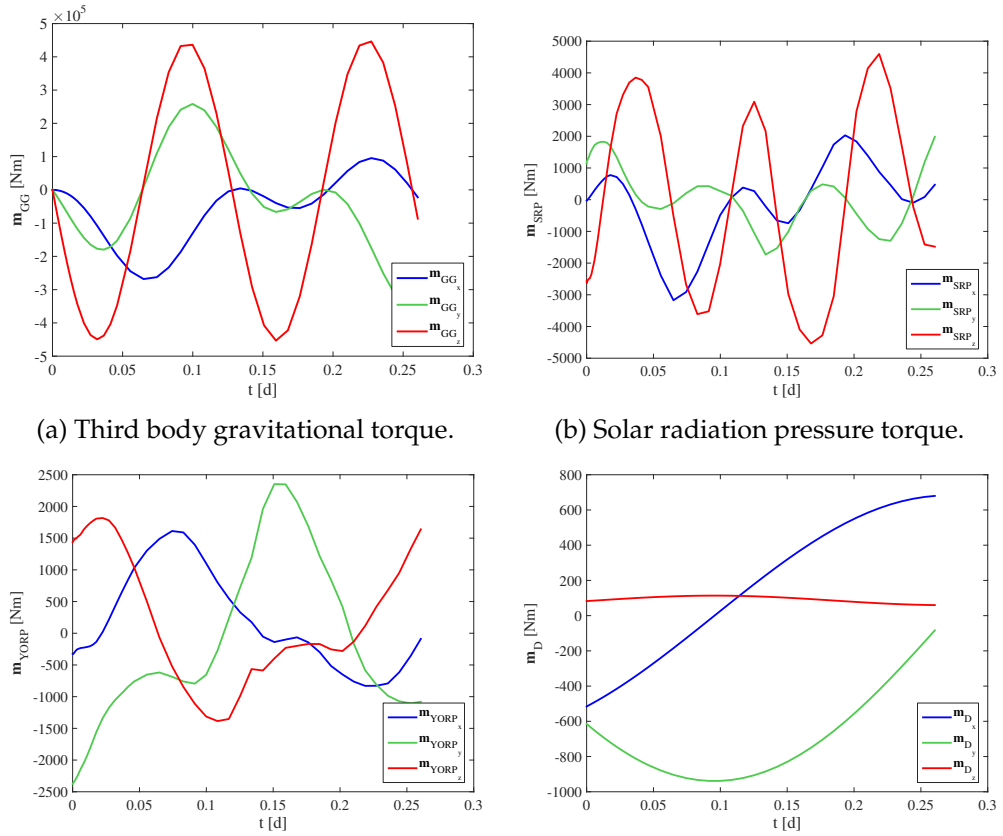

(a) Third body gravitational torque.

(b) Solar radiation pressure torque.

(c) YORP torque.

(d) Dissipation of energy effect.

Figure 4.12: Perturbing torques for 1580 Betulia.

The symmetry of the curves in figure 4.12a highlight the non-secularity contribution of the gravity gradient effect. Moreover, as expected, the larger component of this torque is around $\hat{\mathbf{z}}$, since the spinning direction is almost parallel to the maximum inertia axis. Even figure 4.12b shows a pretty symmetric trend, considering that the majority of the incident radiation acts in the Sun-Body direction and averages to zero. The contribution of the dissipation of energy, figure 4.12d, is obviously the smallest and the components act in a way to reduce the kinetic energy of the body and to have the spinning axis as close as possible to the largest moment of inertia direction. In figure 4.12c, the action of the YORP torque on both the spinning and the obliquity direction is existing. This is common because $\mathbf{m}_\delta$ is an inevitable accompaniment of $\mathbf{m}_z$, and even if $\delta = 0°$ or $\delta = 90°$, the state is unstable and a small perturbation determines the departure of the spinning axis from equilibrium.

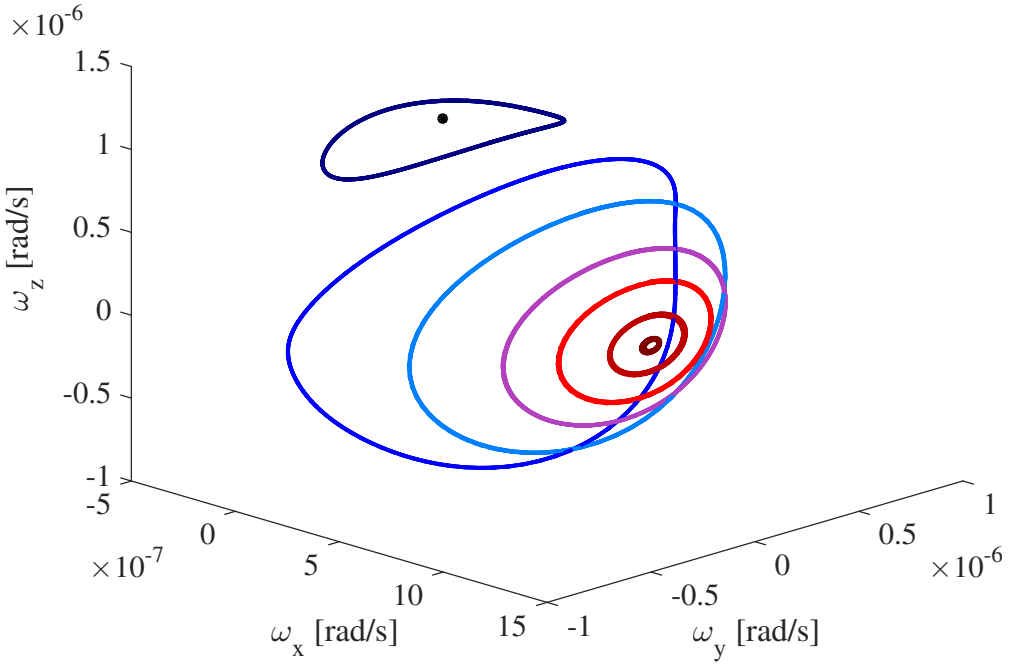

Figure 4.13: Polhodes for different initial conditions on 4179 Toutatis.

4.5 Applications to Selected Environments

The applications for the developed dynamical mode are plentiful and in this thesis only some of them are presented, still they provide a useful insight into the topic that is being analysed in this chapter.

4179 Toutatis Different initial conditions in the rotation state of 4179 Toutatis are simulated and the results presented in figures 4.13 and 4.14. The initial obliquity is chosen arbitrarily, while the magnitude of the angular velocity vector is assumed to be $\|\boldsymbol{\omega}\| = 1 \times 10^{-6}\,\mathrm{rad/s}$. The dynamics is propagated for one orbital period of the asteroid around the Sun, $t_{Sim} \simeq 1000\,\mathrm{d}$. The trajectories of the angular velocity vector on the Poinsot's ellipsoid are not significantly different from the ones that could be obtained simulating the unperturbed motion; the differences do exist, but they are limited and periodic, especially if a short simulation period is considered. The time scale to obtain evident secular variations is at least in the order of 10^3 years.

Figure 4.14 allows to draw more interesting conclusions, focusing only on four different values of initial obliquity: $\delta_0 = [0°, 10°, 20°, 30°]$,

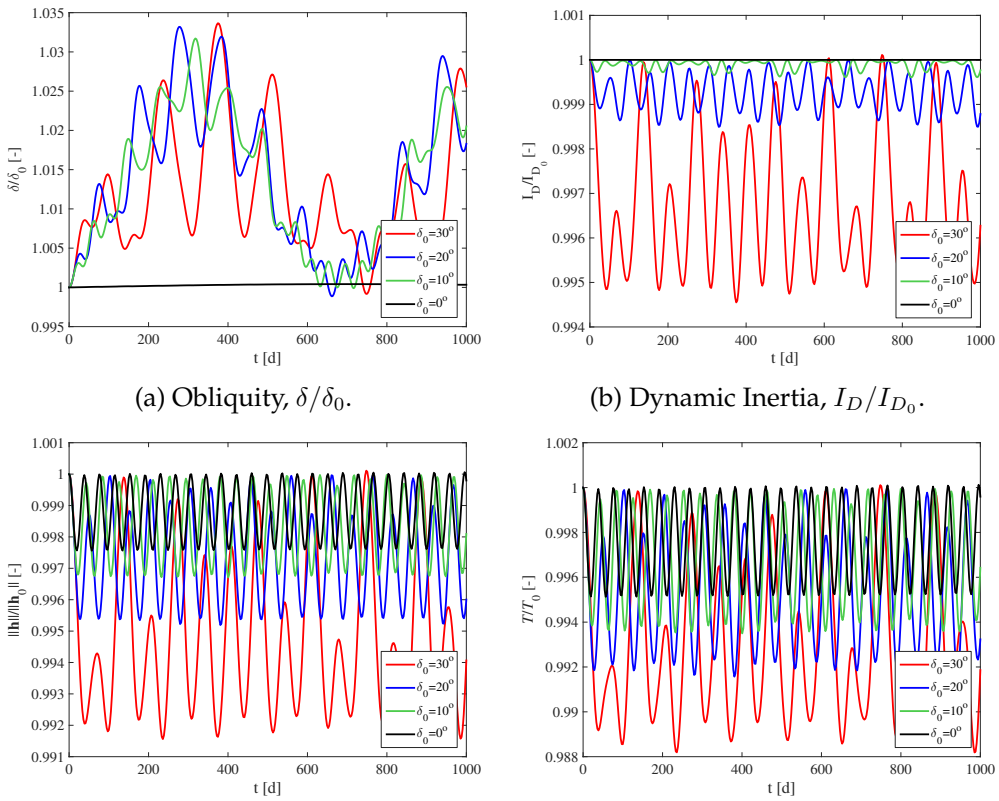

(a) Obliquity, δ/δ_0.

(b) Dynamic Inertia, I_D/I_{D_0}.

(c) Angular Momentum, $\|\mathbf{h}\| \,/\, \|\mathbf{h}_0\|$.

(d) Kinetic Energy, T/T_0.

Figure 4.14: Dynamic quantities for different initial conditions on 4179 Toutatis.

which are also represented with their relative polhodes in figure 4.13. There, they correspond to the blue-toned curves, with $\delta_0 = 0°$ relative to the rotation of the body around the maximum inertia axis, $\hat{\mathbf{z}}$. In this latter case, the rotation of the body is highly stable and the fluctuations of δ and I_D are two orders of magnitude smaller than in the other examples. There are periodic variations in the magnitude of the angular velocity, which are revealed looking at the evolution of angular momentum and kinetic energy, figures 4.14c and 4.14d. So, when the body is in principal rotation state around the maximum inertia axis and the obliquity is equal to $0°$, there are no perturbations able to significantly tilt the spinning axis. In fact, in this case, the dissipation of energy is not present, the gravity gradient produces periodic torques around the rotation axis and the radiative effects have no secular $\delta-$component, $\mathbf{m}_\delta$.

In general, for this particular test, the dynamics with initial condition $\delta_0 = 30°$ is the most affected by the perturbative effects, even though the relative variations of the dynamical quantities are still limited. The

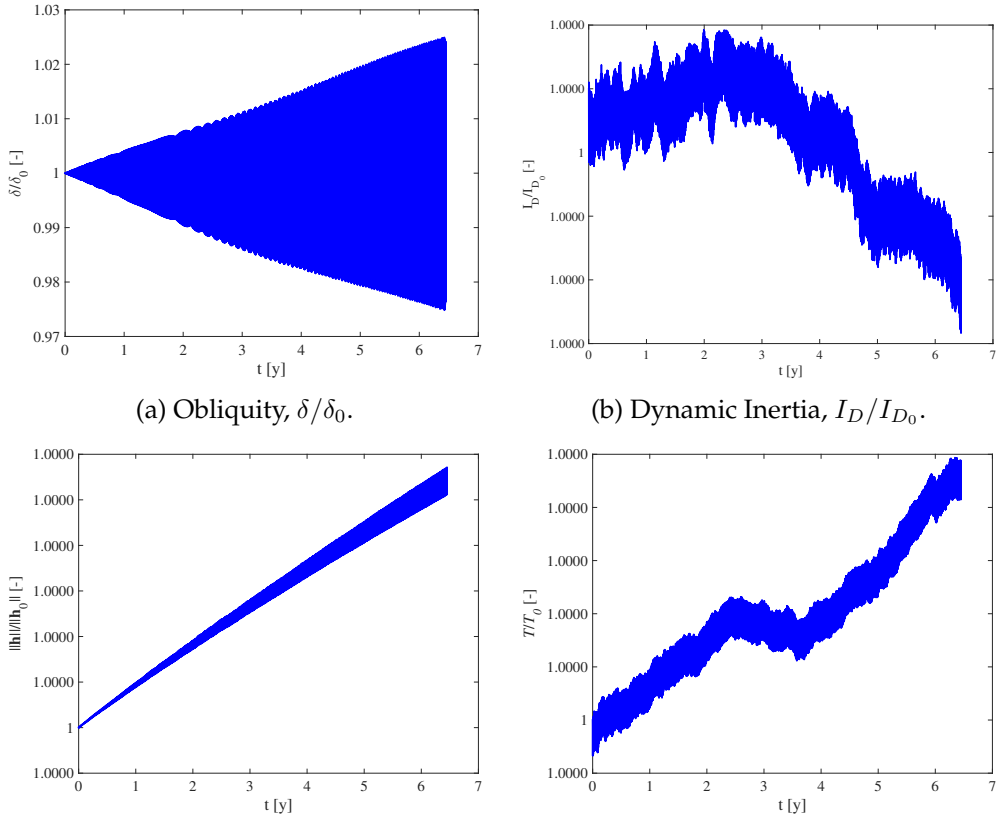

(a) Obliquity, δ/δ_0.

(b) Dynamic Inertia, I_D/I_{D_0}.

(c) Angular Momentum, $\|\mathbf{h}\| \,/\, \|\mathbf{h}_0\|$.

(d) Kinetic Energy, T/T_0.

Figure 4.15: Dynamic quantities for 67P Churyumov-Gerasimenko, real dynamics.

frequency in the oscillations of the analysed quantities is related with the rotation period of the asteroid, which in this case is $\sim 70\,\mathrm{d}$. Another remarkable feature, which can observed in these results, is the similar evolution of δ for $\delta_0 = [10°, 20°, 30°]$ in figure 4.14a. A possible explanation for this is the small difference between the different values of obliquity, determining a similar global influence of the perturbative effect on the rotational dynamics of the asteroid. The frequency in this last trend is comparable with the revolution period, but as expected, it is not exactly the same, remembering that for $\delta \neq 0°$ the YORP and the solar radiation pressure contributions have a not-null average.

67P Churyumov-Gerasimenko The real dynamical state of the comet 67 Churyumov-Gerasimenko has been simulated to have an idea of the actual propagation of its motion. This object has a rotation period of

$\sim 12\,\mathrm{d}$, corresponding to $\|\boldsymbol{\omega}\| \simeq 1.40 \times 10^{-4}\,\mathrm{rad/s}$, and since no multiple periodicities are found in light curves, it is in a simple rotation state around its axis of largest moment of inertia [32]. These data refer to the present rotation state of the body, as measured in 2014 by the European Space Agency's Rosetta mission and they are different from those acquired during the 2009 perihelion passage. This change in the rotation rate of 67P was probably due to sublimation-induced torques, which are not considered in this work, and thus, the present analysis is valid when the object is far from the Sun and the comet activity is low enough. The assumption to have the orbital motion in a circular orbit with radius equal to $3.46\,\mathrm{AU}$ is compatible with this requirement. The dynamics has been simulated for one orbital period of the comet around the Sun, which is equal to $\sim 6.50\,\mathrm{y}$ or $\sim 2400\,\mathrm{d}$. The results are shown in figure 4.15 by means of the usual dynamic quantities.

In this case, the rotation state of the comet 67P is evidently in a stable condition: the secular variation of the considered quantities, in the simulated period, is extremely small. In addition, the periodic oscillations are also limited and the rotation state can be practically considered constant in time. This fact is not surprising, since the simulation tries to represent the reality with a good level of accuracy, and certainly, the actual motion of the comet is now dynamically stable. However, in the plots some trends can be clearly detected: the increase in the kinetic energy and angular momentum and the decrease of dynamic inertia. The reduction in the dynamic inertia is representing the spinning axis that is slowly departing from the maximum inertia axis, as can be similarly understood from the increase in the oscillation of the obliquity. This means that the nutation motion is becoming more important, because of the perturbation that progressively tilts the rotation axis. In the meantime, the kinetic energy and the angular momentum increase, and the only compatible solution is determined by the increase in the magnitude of the angular velocity. In order to explain this point, the secular effect of the radiative perturbations should be considered. According to section 4.2.3, the YORP and the solar radiation pressure spin-up the small Solar System's bodies for $\delta <\sim 55^\circ$, and so, the angular velocity of 67P correctly has a raising trend. The effect of the dissipation of energy is negligible since the rotational dynamics of the body has a small nutation component and a not sufficiently fast spinning rate. It is worth noting that, in the real case, the orbital eccentricity of the comet is different from zero, and in $\sim 6.50\,\mathrm{y}$ the object has one perihelion passage; there, this model is not valid anymore, on account of the existence of an intense comet activity.

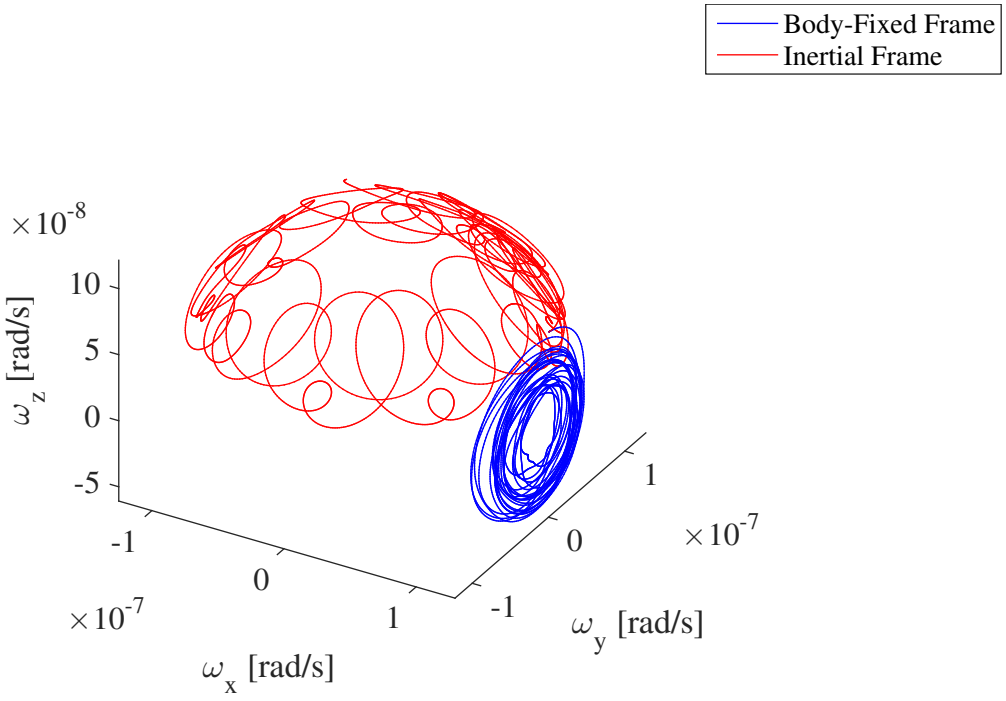

Figure 4.16: Angular velocity trajectories for 67P Churyumov-Gerasimenko, assumed dynamics.

An interesting solution is obtained propagating the dynamics of 67P Churyumov-Gerasimenko for 100 years. In this example the initial conditions for the rotational motion are arbitrarily assumed, with the spinning axis inclined of $30°$ with respect to $\hat{\mathrm{x}}$ and a rotation period of 1 year. These values are totally unrealistic, but they are employed to highlight the effect of the perturbations, because the rotational dynamics is less stiff if the body has a slow spinning rate. So, since the evolution of the dynamic quantities is completely fictional, it is better to have just an overall discussion on the angular velocity trajectories in both the inertial and the body-fixed reference frames. These are plotted in figure 4.16 using a single coordinate system, but it is important to remember that they are computed in two different reference frames that coincide only for $t = 0$. As expected, in this simulation the motion is particularly affected by the perturbations and the secular variation is evident. In fact, the polhode in the body-fixed frame, blue curve, is markedly different from the one related with the torque-free motion. In spite of that, there is not diverging chaotic component of the motion and the trajectory is bounded in a region close to the initial conditions. The perturbative

effects do not destabilize the rotational dynamics of the considered object. This conclusion is globally valid, and the perturbations have always a small impact on the motion of the system, and do not modify the stability of the dynamics. The same trajectory of the angular velocity, evaluated in the inertial space, is interesting to understand the relation between the two systems of reference. Moreover, precession and nutation motions are particularly clear in this perspective, showing the complex dynamical evolution of a perturbed slow spinning body in non-principal rotation state.

This chapter presented some important features of the rotational dynamics of irregular celestial bodies, and it allowed gathering some insightful results and conclusions that will be used, together with those about the gravitational field models, to analyse the dynamics of a particle in the vicinity of irregularly-shaped bodies.

Chapter 5

Dynamics around Irregularly-Shaped Bodies

The dynamics of a body in the vicinity of an irregular Solar System's object is an interesting research topic that has different applications. In fact, the study of this dynamical environment can be employed in designing a space mission around an asteroid or a comet, because the evolution of the motion when the spacecraft is near the target is fundamental during pre-flight navigation and mission planning.

The orbits about these objects are highly non-Keplerian due to the irregular gravitational field, the complex rotation state and the perturbations that exist in this scenario. However, this knowledge can also be employed in the analysis of the unknown properties of these minor space bodies, like the reaccretion and escape of ejecta from the surface after impact, or the evolution of binary asteroid systems. Thus, the outcomes of this research could be applied to solve space engineering or celestial mechanics and planetary science problems, which in the last years are becoming increasingly interesting for the scientific community. Indeed, current space exploration goals for space agencies have missions to asteroids or comets, with rendezvous and orbiting phase. One recent example was the European Space Agency's Rosetta mission that was the first mission to rendezvous, orbit and land a probe on the surface of a comet. Moreover, in the next future, the NASA's Asteroid Redirect and OSIRIS-REx missions, or the JAXA's Hayabusa 2 spacecraft will have to fly in proximity of asteroids. In all these situations, the trajectories are very close to the irregular surface of the interested body, and as a consequence, the dynamics tools must be capable to accurately propagate orbits in these complex dynamical environments.

In this chapter, the algorithm that has been used to propagate the dynamics of a particle around irregularly-shaped bodies is presented. All the aspects that were described in chapters 3 and 4 are now included in the dynamical model to perform some different simulations that show particular features of this problem. The model with perturbation is also compared to a simpler model including only the torque-free rotational motion of the irregular object. In addition, the existence of equilibrium points for simple rotational state is discussed together with the evolution of the Zero Velocity Surfaces.

It is worth remembering that the presented model consider a massless particle, which does not affect the motion of the main body, and the perturbative effects act only indirectly on the motion of the particle through their action on the rotational state of the main body.

5.1 Model Implementation

The dynamical model is bases on a set of 18 different first order scalar differential equations (2.65), which are expressed in the body-fixed reference frame, B. They derive from the vectorial form of the equations of dynamics and kinematics, (2.49), (2.54) and (2.63) described in section 2.4.4, and they are coupled by the terms due to the non-inertial reference system. For numerical integration, they can be written as:

$$\dot{\boldsymbol{V}} = \begin{bmatrix} \dot{\bar{\mathbf{A}}}^{\mathrm{T}} \\ \dot{\omega}_x \\ \dot{\omega}_y \\ \dot{\omega}_z \\ \dot{x} \\ \dot{y} \\ \dot{z} \\ \ddot{x} \\ \ddot{y} \\ \ddot{z} \end{bmatrix} = \boldsymbol{f}(\boldsymbol{V}) = \begin{bmatrix} \boldsymbol{f}_{\dot{\bar{\mathbf{A}}}}(\boldsymbol{\omega}, \bar{\mathbf{A}})^{\mathrm{T}} \\ f_{\dot{\omega}_x}(\boldsymbol{\omega}, \mathbf{I}, \mathbf{m}) \\ f_{\dot{\omega}_y}(\boldsymbol{\omega}, \mathbf{I}, \mathbf{m}) \\ f_{\dot{\omega}_z}(\boldsymbol{\omega}, \mathbf{I}, \mathbf{m}) \\ \dot{x} \\ \dot{y} \\ \dot{z} \\ f_{\ddot{x}}(\mathbf{p}, \dot{\mathbf{p}}, \boldsymbol{\omega}, \dot{\boldsymbol{\omega}}, \nabla U) \\ f_{\ddot{y}}(\mathbf{p}, \dot{\mathbf{p}}, \boldsymbol{\omega}, \dot{\boldsymbol{\omega}}, \nabla U) \\ f_{\ddot{z}}(\mathbf{p}, \dot{\mathbf{p}}, \boldsymbol{\omega}, \dot{\boldsymbol{\omega}}, \nabla U) \end{bmatrix}, \tag{5.1}$$

where $\boldsymbol{f}_{\dot{\bar{\mathbf{A}}}}$ represents the equations of rotational kinematics; $f_{\dot{\omega}_x}$, $f_{\dot{\omega}_y}$ and $f_{\dot{\omega}_z}$ the Euler's rotation equations; $f_{\ddot{x}}$, $f_{\ddot{y}}$ and $f_{\ddot{z}}$ the equations of motion of the particle, in the B system. The notation $\bar{\mathbf{A}}$ symbolize a row vector containing all the 9 components of the rotation matrix, $\mathbf{A}$.

The initial conditions are contained in $\boldsymbol{V}_0 = [\bar{\mathbf{A}}_0, \boldsymbol{\omega}_0, \mathbf{p}_0, \dot{\mathbf{p}}_0]^{\mathrm{T}}$, where all the quantities are evaluated at $t = 0$.

The system of coupled equations (5.1) is integrated with an explicit Runge-Kutta solver. This is a single step solver, and in order to compute the solution at $t = t_n$, it needs only the solution at the immediately preceding time point, $t = t_{n-1}$. The tolerances in the error are stringent and the accuracy of the integration procedure is always monitored with some reference quantities.

At each integration step, the differential equation solver evaluates the gravitational field in the current field point, and then it computes the Sun-Body direction in the inertial frame, which is suddenly rotated in the body-fixed coordinate system. All the external perturbing torques are evaluated as described in chapter 4, and they are included in the vector $\mathbf{m}$. Next, all these quantities are substituted in equation (5.1) and the coupled dynamics is propagated forward in time.

The algorithm verifies at each time step the Laplacian of the gravitational potential; if it is equal to 4π the field point is inside the body and the integration is terminated, since the particle crashed on the main attractor.

The discussion that has been carried out in chapter 3 is here used to implement the most effective and efficient integration algorithm. In fact the optimum Lo-Fi model is employed, and it is a combination of a polyhedron model with and an optimized mascons. The former is used in proximity of the surface and it is implemented with a number of faces in the order of $\sim 10^3$, while the latter is active when the field point is far enough from the centre of mass of the main attractor and it has $N_m \simeq 500$. In this way, according to the results of section 3.5, the error on the gravitational attraction is guaranteed to be below 5% even on the surface, with a mean value of $\sim 0.35 \pm 0.05\%$. The switch between the two different models happens at a distance of ~ 7.5 averaged radii of the body from the centre of mass; there the gap between the two models is practically negligible, and thus, there is no sensible discontinuity in the field.

The algorithm requires a tolerable computational time to operate, and with a MATLAB® code running in parallel on a quad-core 2.50 GHz processor, a simulation of $30\,\mathrm{d}$ needs approximately 24 hours to complete. Usually the code was launched on a multi-core server, with computational times in the order of few hours. The most consuming activities are the evaluation of the gravitational field and the computation of the surface disturbing torques, with the self-shadowing effect, at each integration step. The speed of the algorithm could be improved reducing access to these functions exploiting some interpolation techniques or some further approximations. A huge boost in the computational speed

could be obtained if the numerical integration is performed with algorithms that are written in a simpler and lighter language than MATLAB®, such as C or Fortran.

5.1.1 Orbital Elements

The differential equation solver produces an output that is composed by the state vector, $\boldsymbol{V}(t)$, computed at each integration step. Hence, the time evolution of the kinematics and the dynamics of particle and main body is described by the quantities contained in the matrix of state vectors:

$$\mathbf{D}(t) = [\boldsymbol{V}(t)^{\mathrm{T}}] = \begin{bmatrix} \boldsymbol{V}(0)^{\mathrm{T}} \\ \boldsymbol{V}(t_1)^{\mathrm{T}} \\ \cdots \\ \boldsymbol{V}(t_n)^{\mathrm{T}} \\ \cdots \\ \boldsymbol{V}(t_{Sim})^{\mathrm{T}} \end{bmatrix} = [\bar{\mathbf{A}}(t), \boldsymbol{\omega}(t), \mathbf{p}(t), \dot{\mathbf{p}}(t)], \tag{5.2}$$

where t_{Sim} is the simulation time.

From the data contained in $\mathbf{D}(t)$ the complete description of the analysed motion can be immediately obtained. Notwithstanding, in order to have an insightful overview on the dynamics of the particle, the exploitation of the orbital elements can be extremely helpful.

The orbital elements are six parameters required to uniquely identify a specific orbit in the three-dimensional space. The traditional orbital elements are the six Keplerian elements, after Johannes Kepler and his laws of planetary motion, and they are generally used in classical two-body systems, where a Keplerian motion is considered. In the mathematical approximation of the ideal two-body problem, these quantities are constant in time, but in a real orbit, they are time-varying parameters.

In the current analysis, the orbit of the particle is highly non-Keplerian because of the complex dynamical environment, and thus, the orbital elements usually show large and irregular fluctuations in time. Moreover, the gravitational potential is different from the classical one, and these parameters are here computed as if the asteroid or the comet were a centrobaric body with the same mass M.

The orbital parameters are evaluated in the inertial space. They are obtained from the state vector of the particle, $\boldsymbol{V}_P(t) = [\mathbf{p}(t), \dot{\mathbf{p}}(t)]^{\mathrm{T}}$, and from the *standard gravitational parameter*, $\mu = GM$. The state vector must be expressed in the inertial reference frame, as $\boldsymbol{V}_{P_I}$. So, from $\boldsymbol{V}_{P_I}(t)$ and

μ it is possible to compute all the six Keplerian elements at each integration step. They are: semi-major axis $a(t)$, eccentricity $e(t)$, inclination $i(t)$, longitude of ascending node $\Lambda(t)$, argument of periapsis $\lambda(t)$, and true anomaly $\nu(t)$. In order to simplify the computation, the reference plane to define the orientation of the orbit in the three-dimensional space, is assumed to be the orbital plane of the irregular object around the Sun. As a consequence, the normal vector to the reference plane is $\hat{\mathbf{z}}_I$. The reference is normally defined as the plane orthogonal to the rotation axis of the main attractor; however, this is not fixed in the inertial space and the other option was chosen. The reference axis to define the longitude of ascending node, Λ, is $\hat{\mathbf{x}}_I$.

The analyses that are presented in this chapter make use only of three Keplerian elements, since they are sufficient for the current purposes. They are semi-major axis, eccentricity and inclination of the orbit. In fact, they allow having an overview on shape and size of the trajectory and on the change in the 3D orientation of the orbit. Furthermore, they provide information that could be exploited to evaluate the approximated orbital period and energy content of the motion.

In the classical two-body problem the semi-major axis is computed as:

$$a = \frac{\|\mathbf{p}_I \times \mathbf{v}_I\|^2}{\mu(1-e^2)}, \tag{5.3}$$

where the eccentricity e is available from:

$$\mathbf{e} = \frac{\mathbf{v}_I \times (\mathbf{p}_I \times \mathbf{v}_I)}{\mu} - \frac{\mathbf{p}_I}{\|\mathbf{p}_I\|}, \tag{5.4}$$

and

$$e = \|\mathbf{e}\|. \tag{5.5}$$

The inclination is the angle between the orbital momentum vector and the normal vector to the reference plane, $\hat{\mathbf{z}}_I$. So, it can be computed as:

$$i = \arccos\left(\frac{(\mathbf{p}_I \times \mathbf{v}_I) \cdot \hat{\mathbf{z}}_I}{\|\mathbf{p}_I \times \mathbf{v}_I\|}\right). \tag{5.6}$$

It is important to consider that in this research work only closed orbits around the main attractor are considered. Therefore, the trajectory of the particle is instantaneously on a circular or an elliptic osculating orbit. The concept expressed by the word *instantaneously* is fundamental, because,

having a non-Keplerian motion, equations (5.3), (5.4) and (5.6) are valid only if evaluated at each instant of time with the made approximations.

The energy content of a Keplerian osculating orbit is expressed by the *specific mechanical energy*:

$$\varepsilon = -\frac{\mu}{2a}, \tag{5.7}$$

which depends only on the semi-major axis, a. For a closed orbit $\varepsilon < 0$ and the motion of the particle is bounded in a region close to the primary. Yet, it is important to remember that the complexity of the analysed environment creates other constraints for the dynamics of P, as discussed in section 2.4.5. The evaluation of this quantity is extremely simple and it provides a general estimation of the energy content in the particle dynamics. In addition, the Keplerian energy, ε, and the Jacobi constant, C, can be related by an equation derived and expressed in [42], which is used in the algorithm to check the validity of the integration process.

In a similar way, an approximation of the *orbital period* of the particle, T_P, is computed, at each instant of time, exploiting the result of the classical Keplerian dynamics:

$$\mathrm{T}_P = 2\pi\sqrt{\frac{a^3}{\mu}}. \tag{5.8}$$

Equation (5.8) can be used to adjust the simulation time, t_{Sim}, for a given set of initial conditions, according to the approximated orbital period at $t = 0$.

The complete derivation of these Keplerian relations can be found in [2, 9, 10].

5.2 Zero Velocity Surfaces and Equilibrium Points

The Jacobi integral of motion does not exist in general for the coupled dynamics of a particle around a rotating irregular body. However, as already explained in chapter 2, the integral of motion is conserved is if the main body is in a uniform unperturbed principal axis rotation. In this case, the Zero Velocity Surface is fixed, and thus, the equilibrium points, which are particular solutions of the Zero Velocity Surface, are fixed in space and time. Their analysis is useful, since if the motion of

the primary body is more complex they could be always defined at each instant of time. Moreover, they provide an interesting point of view of the dynamical environment and it is worth knowing their position. Furthermore, the evolution of the Zero Velocity Surface for different initial conditions of the particle, or for different rotational state of the irregular body, highlights the region of space where the motion of P is allowed. This is extremely helpful to have a preliminary understanding of the orbital dynamics, knowing only the initial conditions of the simulation.

The algorithm to locate the equilibrium solutions and the Zero Velocity Surfaces is based on the same optimum Lo-Fi model that has been described in section 5.1. The surfaces satisfy the equation $V(\mathbf{p}) = C$ and therefore, having available a 3D grid of V values around the main body, they are just the collection of the loci where the previous equality is satisfied. Instead, the computation of the position of the equilibrium solutions is trickier. Basically, the algorithm has to find the points where the gradient of V is equal to zero, but since no analytical expression of this function is available, a numerical method has been implemented to solve equation (2.75).

First, the pseudo-potential function is evaluated on a 3D grid of points that is then subdivided in 27 sub-grids. The minimum value of V in each sub-grid is detected and its position is provided as an initial guess for the equation solver. Then, a Levenberg-Marquardt based algorithm is started to find the zeros of the gradient of V; this numerical method has been chosen since it has the best performances among all the algorithms available. All the found solutions are then verified, and only if they satisfy some requirements they are listed as real equilibrium points. An actual solution is saved if the flag returned by the equation solver indicates the real convergence of the algorithm and if each component of $\nabla V(\mathbf{p})$ is below $10^{-8}\,\mathrm{m\,s^{-2}}$.

The number of equilibrium points is not predetermined and they are indicated by the symbol E_i, with $i = 1, \ldots, n_E$ and they are sorted by value of Jacobi constant. In a way that E_1 is the equilibrium point with the largest C value, or lowest energy level, and E_{n_E} is the one with the smallest Jacobi constant, or largest energy, i.e. $C(E_1) > C(E_2) > \cdots > C(E_{n_E})$. It is important to note that the positions and the energy levels of the equilibrium points depends on the particular gravitational model that is employed; hence, the results that are shown in this chapter are obtained with the already mentioned Lo-Fi model, under the assumptions that have been presented before.

Evolution of the Zero Velocity Surfaces All these concepts can be easily explained visualizing the evolution of the Zero Velocity Surfaces. This is shown in figures 5.1 and 5.2, both with a 3D view and with a 2D projection on the $xy-$plane for the asteroid 216 Kleopatra, which is assumed to be in principal rotation state around the $z-$axis with $\|\boldsymbol{\omega}\| \simeq 3.20 \times 10^{-4}\,\mathrm{rad/s}$. Therefore, in this case the integral of motion exists and the Zero Velocity Surfaces are fixed in time, bounding the motion of P in the same region of space for any $t > 0$, according to the given C value.

Looking at figures 5.1a and 5.2a, when the energy is lower than the one associated with the first equilibrium point E_1, there are three distinct regions: the inner region, between the surface of the body and the interior surface; the middle region, between the two surfaces, and the outer region outside the cylindrically-shaped Zero Velocity Surface. The first and the latter are allowed for the motion of the particle, while the space between the two surfaces is a forbidden region. Hence, for this energy level P cannot approach the body from the outer region or escape from its surface. If C is even higher than the one in figure 5.1a, the inner region is inside the volume of the body and the particle cannot fly close to the surface of the body: only the outer region is practically allowed.

Increasing the energy, at $C = C(E_1)$, the surface intersects the first equilibrium point, E_1, and it opens in figures 5.1b and 5.2b. Similarly for $C = C(E_2)$, figures 5.1c and 5.2c, the Zero Velocity Surface releases the second equilibrium point. These gap in the surface are called *gateways*, since they allow the motion between the inner and the outer regions. In fact, in figure 5.2c, the forbidden region is divided in two separate portions and the motion from the surface the body to the outer space is now allowed, through both gateways at E_1 and E_2.

Then, for lower value of the Jacobi constant, the inner region expands and intersects the third, and later, the fourth equilibrium point. In figures 5.1d and 5.2d, the forbidden region is just a point at E_3, while in figures 5.1e and 5.2e it is only around the E_4. At the end, when the energy is high, $C < C(E_4)$, the Zero Velocity Surface does not intersect the $xy-$plane anymore, but the bounds on the motion of the particle are still present in the three-dimensional space. For high enough energy, the limiting surfaces completely disappear and the dynamics of the particle has no more constraints.

In table 5.1, the positions of the equilibrium points, expressed in the body-fixed frame, with the relative Jacobi constants are reported. It

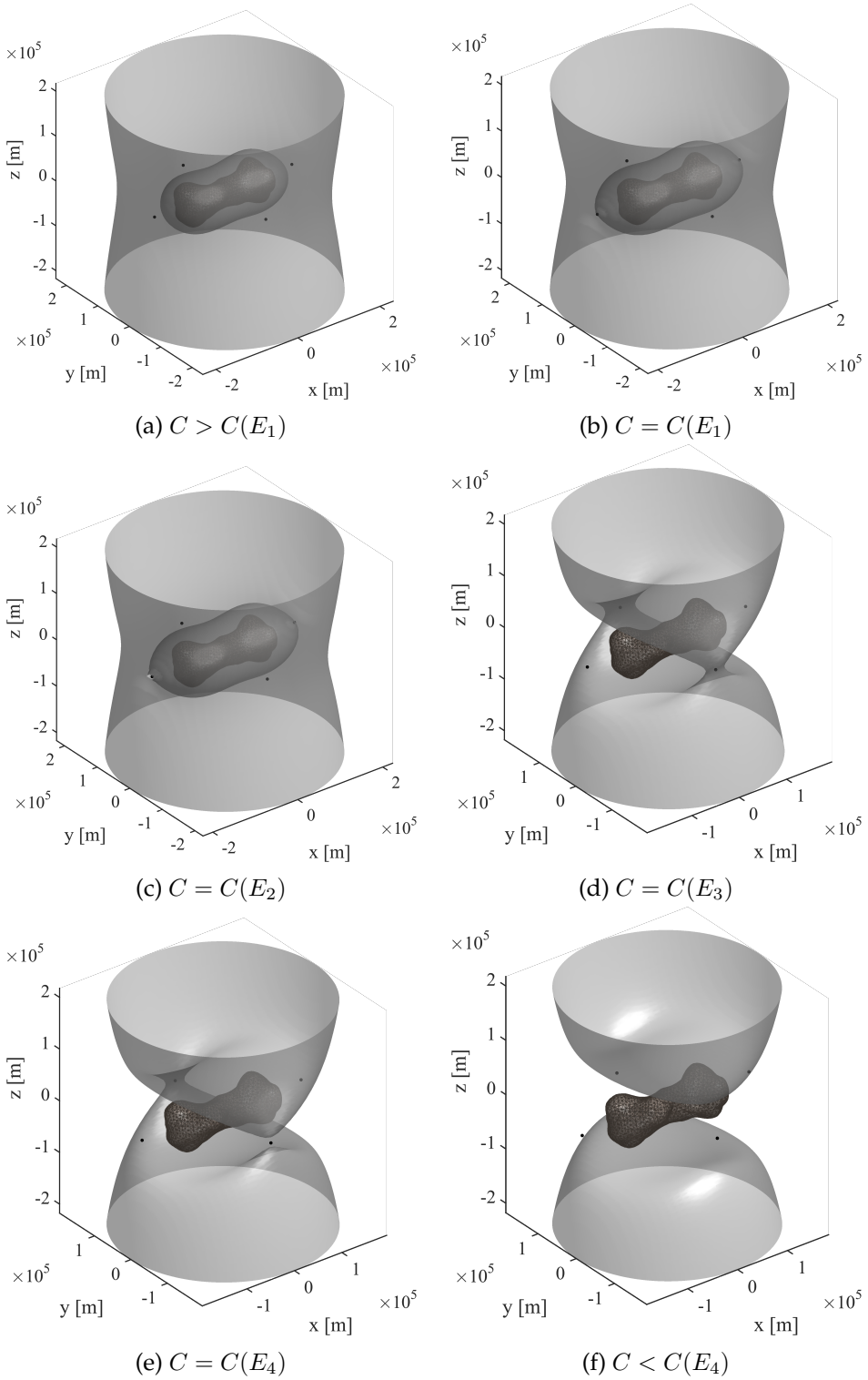

(a) $C > C(E_1)$ (b) $C = C(E_1)$

(c) $C = C(E_2)$ (d) $C = C(E_3)$

(e) $C = C(E_4)$ (f) $C < C(E_4)$

Figure 5.1: Evolution of the Zero Velocity Surfaces for 216 Kleopatra, 3D view.

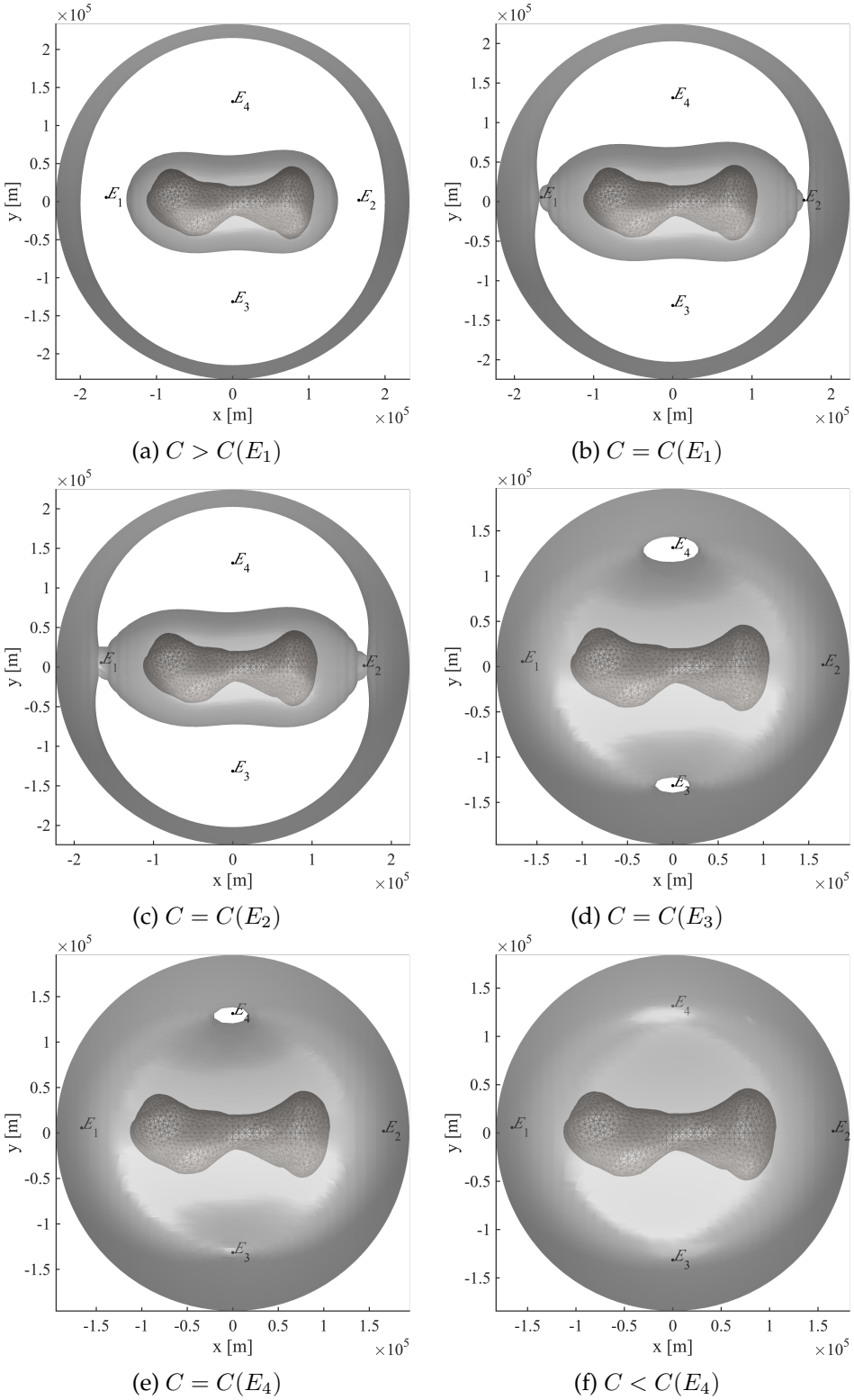

(a) $C > C(E_1)$ (b) $C = C(E_1)$

(c) $C = C(E_2)$ (d) $C = C(E_3)$

(e) $C = C(E_4)$ (f) $C < C(E_4)$

Figure 5.2: Evolution of the Zero Velocity Surfaces for 216 Kleopatra, 2D view.

Table 5.1: Equilibrium Solutions for 216 Kleopatra.

	x_E [m]	y_E [m]	z_E [m]	C [$\mathrm{m^2\,s^{-2}}$]
E_1	-1.6610×10^5	5.6730×10^3	5.9840×10^2	3619.3866
E_2	1.6560×10^5	1.9480×10^3	3.0230×10^3	3614.6227
E_3	-8.8240×10^{-11}	-1.3140×10^5	9.2760×10^{-10}	3052.9487
E_4	-4.7190×10^{-10}	1.3140×10^5	1.3630×10^{-10}	3037.4288

should be noted that this values could be dissimilar if another gravitational model or different data are employed.

The data in the table show that the equilibrium points are almost symmetric with respect to the x and y axes and they practically lay on the $xy-$plane. This can be explained considering the quasi-symmetry of the asteroid Kleopatra and the assumed direction of the spinning axis: the balance between the forces in the rotating frame is in the plane orthogonal to the spinning direction. Moreover, in this case, the first two equilibrium points have a remarkably similar energy level.

Influence of the Shape of the Body The results that have presented in the previous section obviously depend on the particular dynamical environment that is considered; in fact, any other non-spherical object has different Zero Velocity Surfaces and equilibrium points, considering that they are derived from the pseudo-potential function, which depends on the geometry of the body.

In figure 5.3, the equilibrium points and the Zero Velocity Surfaces, projected on the plane orthogonal to the spinning direction, are shown for all the remaining bodies. The analysed rotational states are the real ones, described in section 2.4.7.

First of all it should be noted that for Toutatis the spinning axis is inclined 21° with respect to the $x-$axis, and thus, the plane that is shown in figure 5.3d is not a reference plane. Then, from this point of view, the shape of the object is fairly symmetric, and as a consequence, the Zero Velocity Curves are nearly circular. The equilibrium points in this case have particularly similar energy level. So, instead of actually distinct equilibrium points, this dynamical environment has an *equilibrium ring*. Basically, this is about the same equilibrium area that is present around a centrobaric body like the Earth, which has the *geostationary* ring. In fact, each geostationary satellite lies is on an equilibrium point if observed in an Earth-fixed reference frame. The six equilibrium points of this body are far from the central attractor, if compared with the other objects in the same figure, and this is due to the slow spinning rate of the

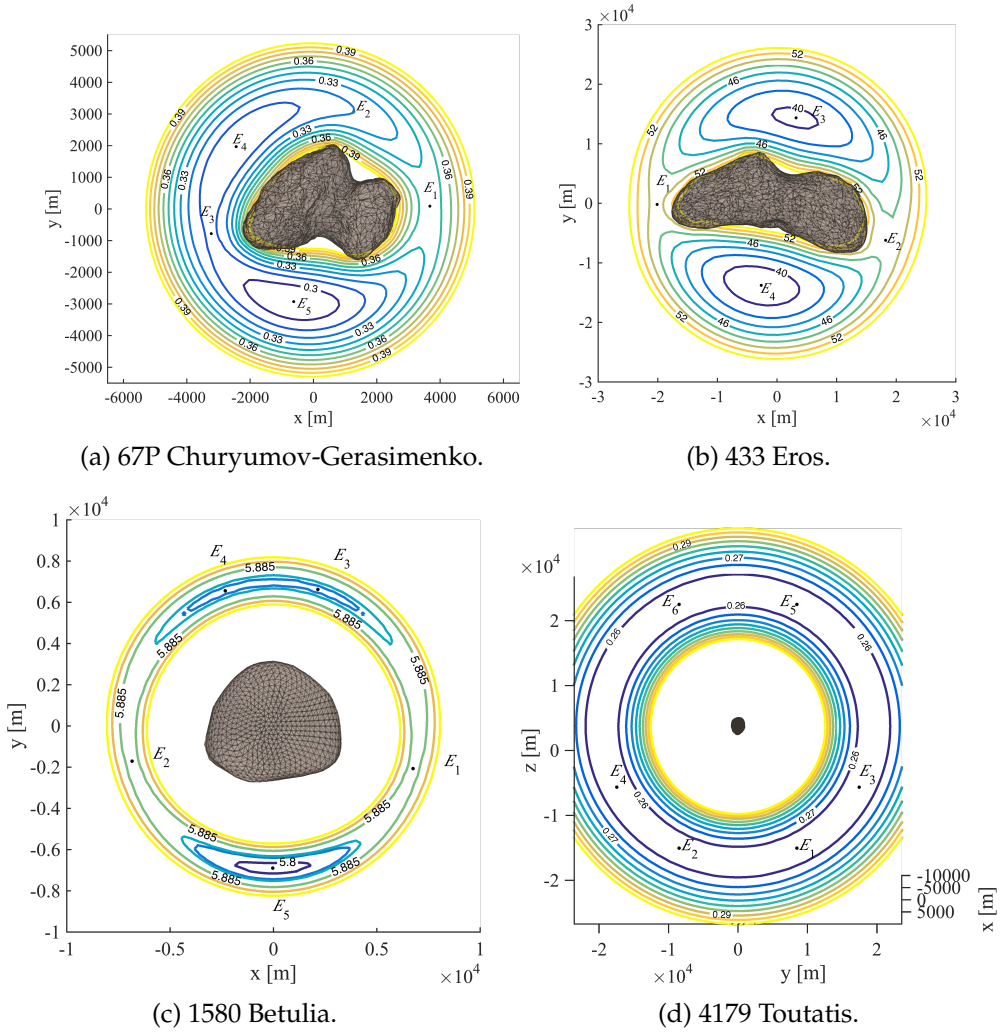

(a) 67P Churyumov-Gerasimenko.

(b) 433 Eros.

(c) 1580 Betulia.

(d) 4179 Toutatis.

Figure 5.3: Zero Velocity Curves on the plane orthogonal to the spinning direction and Equilibrium Points. (The labels on the curves indicate the relative C value in $\left[\mathrm{m}^2\,\mathrm{s}^{-2}\right]$. The black dots are the equilibrium points.)

body. Moreover, 4179 Toutatis is in a complex rotational state and the computed results refer only to an instantaneous condition, with $\|\boldsymbol{\omega}\| \simeq 2.10 \times 10^{-5}\,\mathrm{rad/s}$ around the already mentioned non-principal inertia axis.

In spite of the existence of an equilibrium ring, the algorithm converges to six distinct equilibrium points, because the field is not perfectly circular, and the irregularities in the shape guarantee the presence of discrete equilibrium locations. In figure 5.3c, the results show a similar behaviour to the one that has been described for Toutatis. In fact, 1580

Betulia can be assumed as a quasi-spherical object. However, in this case the smaller distance of the equilibrium ring to the surface of the body produces a more irregular shape of the Zero Velocity Curves. Furthermore, the location of the five equilibrium points can be directly related to the visible features of the shape of this asteroid.

The comet 67P and the asteroid 433 Eros, in figures 5.3a and 5.3b, are characterized by a considerably irregular field. They have, respectively, five and four equilibrium solutions, which are identified by different energy levels. In the case of 433 Eros the evolution of the Zero Velocity Curves is similar to the one of 216 Kleopatra, presented in figure 5.2. The main difference between these two objects is the distant energy level, $C \sim 50$ for Eros and $C \sim 3000$ for Kleopatra, due to the two dissimilar mass values. Instead, the comet 67P has a slightly different dynamical environment with an additional equilibrium location. In this case the main bulge, on the left in figure 5.3a, modifies the shape of the Zero Velocity Surfaces and generates a region of similar energy level around itself. This area embraces E_3, E_4 and E_5, and it is a rough approximation of an equilibrium ring, due to the presence of the larger lobe of the comet.

In table 5.2, the coordinates of the equilibrium points, with their values of Jacobi constant, are listed for all the bodies represented in figure 5.3. These values are evaluated under the current set of assumptions, employing the data that are presented in this thesis. They agree with the preceding discussion and support the previous analysis on the evolution of the Zero Velocity Surfaces.

The Zero Velocity Surfaces establish boundaries for the motion in the vicinity of an irregularly-shaped body. They depend on the shape of the object, but also on its rotational state.

Influence of the Spinning Rate The spinning rate of a body influences the dynamical environment around itself; in fact, in the body-fixed frame the fictitious forces are dependent also on the magnitude of the angular velocity. The centrifugal acceleration, in the non-inertial reference frame, is the only contribution that influences the shape of the Zero Velocity Curves, and accordingly, the position of the equilibrium points: for $\dot{\mathbf{p}} = 0$ the Coriolis acceleration is null. This effect has been already mentioned with the asteroid 4179 Toutatis in figure 5.3d, whose equilibrium points are at a great distance because of its slow rotation. This is completely reasonable since, for a fast spinning attractor, the centrifugal acceleration in B is larger, and it is balanced only if a particle is close enough to the

Table 5.2: Equilibrium Solutions for the other reference bodies.

(a) 67P Churyumov-Gerasimenko.

	x_E [m]	y_E [m]	z_E [m]	C [$\mathrm{m^2\,s^{-2}}$]
E_1	3.6740×10^3	8.5860×10^1	9.6310×10^1	0.3456
E_2	1.2800×10^3	3.0840×10^3	3.3320×10^1	0.3198
E_3	-3.2260×10^3	-7.7850×10^2	9.4090×10^1	0.3085
E_4	-2.4390×10^3	1.9670×10^3	2.0570×10^2	0.3022
E_5	-6.2380×10^2	-2.9270×10^3	-5.4990×10^1	0.2926

(b) 433 Eros.

	x_E [m]	y_E [m]	z_E [m]	C [$\mathrm{m^2\,s^{-2}}$]
E_1	-2.0100×10^4	-1.9950×10^2	-5.5190×10^2	49.5066
E_2	1.8200×10^4	-6.2030×10^3	3.8910×10^1	48.3153
E_3	3.1890×10^3	1.4350×10^4	1.9020×10^1	39.6254
E_4	-2.6560×10^3	-1.3780×10^4	-2.5590×10^2	38.6950

(c) 1580 Betulia.

	x_E [m]	y_E [m]	z_E [m]	C [$\mathrm{m^2\,s^{-2}}$]
E_1	6.7510×10^3	-2.0700×10^3	-6.0880×10^1	5.8723
E_2	-6.8420×10^3	-1.7140×10^3	-1.0790×10^2	5.8701
E_3	2.1520×10^3	6.6290×10^3	7.4180×10^1	5.8210
E_4	-2.3330×10^3	6.5620×10^3	1.8590×10^1	5.8201
E_5	-3.7240×10^1	-6.9010×10^3	4.5210	5.7901

(d) 4179 Toutatis.

	x_E [m]	y_E [m]	z_E [m]	C [$\mathrm{m^2\,s^{-2}}$]
E_1	6.1560×10^3	8.4870×10^3	-1.6460×10^4	0.2566
E_2	6.1560×10^3	-8.4870×10^3	-1.6460×10^4	0.2566
E_3	3.0780×10^3	1.7450×10^4	-8.2320×10^3	0.2564
E_4	3.0780×10^3	-1.7450×10^4	-8.2320×10^3	0.2564
E_5	-6.1560×10^3	8.4870×10^3	1.6460×10^4	0.2562
E_6	-6.1560×10^3	-8.4870×10^3	1.6460×10^4	0.2561

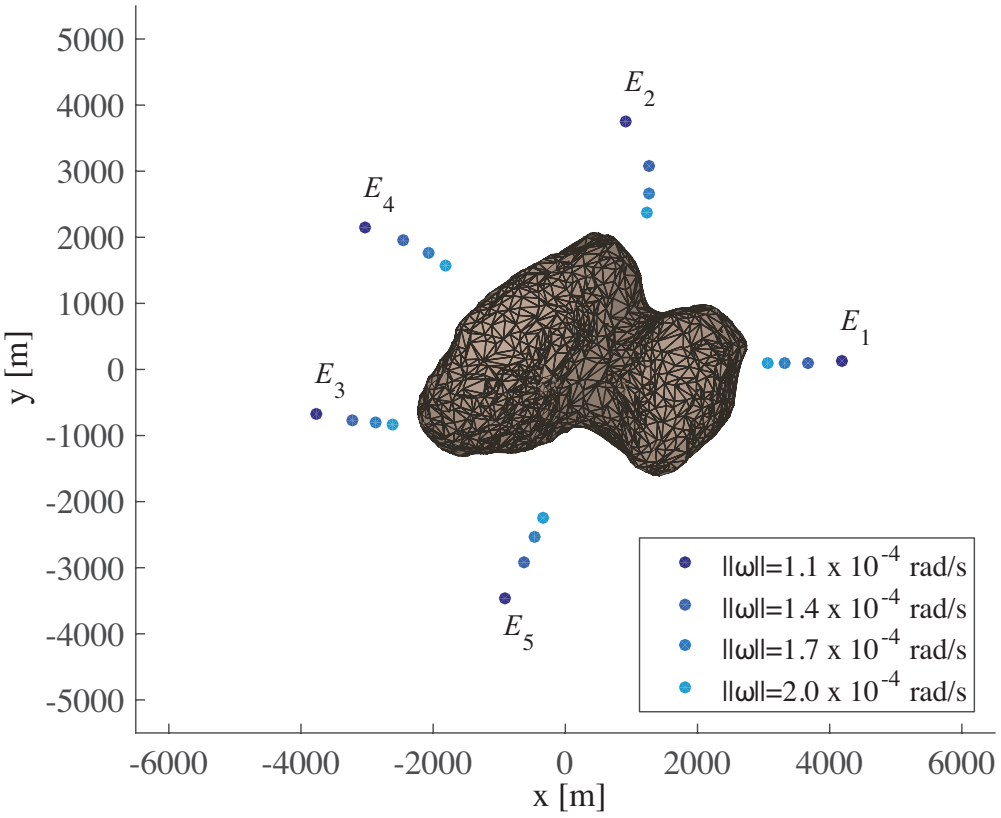

Figure 5.4: Equilibrium points and spinning rate, for 67P Churyumov-Gerasimenko.

surface, where the gravitational attraction is stronger. This concept has been verified, and the results obtained for the comet 67P are shown in figure 5.4.

Here, the positions of the equilibrium points agree with the expected trend, and obviously, there is a change in the energy levels associated with these locations. In fact, in the real motion $\|\boldsymbol{\omega}\| \simeq 1.40 \times 10^{-4}\,\mathrm{rad/s}$, the equilibrium points have an average C of $0.31\,\mathrm{m^2\,s^{-2}}$, while, for $\|\boldsymbol{\omega}\| \simeq 1.10 \times 10^{-4}\,\mathrm{rad/s}$, $C \sim 0.27\,\mathrm{m^2\,s^{-2}}$, and for $\|\boldsymbol{\omega}\| \simeq 2.00 \times 10^{-4}\,\mathrm{rad/s}$, $C \sim 0.40\,\mathrm{m^2\,s^{-2}}$. This is reasonable because, for a given position, the Jacobi constant increases with the magnitude of the angular velocity. Moreover, closer to the surface the gravitational potential is larger, and according to equation (2.69), C increases.

Influence of the Spinning Direction The direction of the rotation axis is another feature that influences the shape of the Zero Velocity Surfaces

and the position of the equilibrium points. As already noted with the example of 4179 Toutatis, the balance between the forces in the rotating frame is in the plane orthogonal to the spinning direction.

In the real world, the spinning direction of irregular celestial bodies can undergo large oscillations, and it is reasonable to wonder how the dynamical environment of a single object is modified for different orientations of the rotation axis. In figure 5.5, three different spin directions are simulated for the comet 67P; in all the case the magnitude of the angular velocity is the real one. The spin directions coincide with the three principal inertial direction, and when $\hat{\mathbf{z}}$ is considered, the conditions are the same of figure 5.3a. The plotted Zero Velocity Surfaces correspond to $C = 0.35\,\mathrm{m}^2\,\mathrm{s}^{-2}$ and the direction of the rotation axis is parallel to the axis of the external cylindrical surface.

From this figure, it is evident that the dynamical environment is dramatically modified by the direction of the rotation axis. In the extreme case of the three orthogonal principal inertia axes, the number of equilibrium points is different between the different simulation on 67P. Each case can be analysed, as the one in figure 5.5c in the previous paragraph. The number and the position of the equilibrium solutions depend on the shape that the body has orthogonally to the spin direction. It can be noted that in figure 5.5a the three equilibrium positions are approximately distributed on an equilibrium ring, since, if 67P is observed along $\hat{\mathbf{x}}$, its shape is approximately circular.

5.3 Applications to Selected Environments

The previous analyses are extremely useful to have some preliminary insights on the dynamical environment of an irregularly-shaped body. They provide dynamical information in simple situations, which can be exploited to obtain the initial conditions to run some useful simulations. In this work, the complete dynamical model is used; thus, there is no integral of motion and the solutions are dependent from several parameters and assumptions. The fidelity and accuracy of the model are continuously tested and the results are considered to be exact under the current set of hypotheses. However, the high fidelity of the simulations does not allow drawing general conclusions, and all the obtained simulations are only representative for the particular dynamical environment that is considered.

Many approximated and linearized techniques are available in the literature to study the general features of the dynamics around irregular

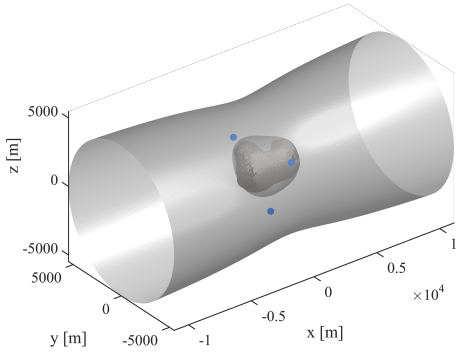

(a) $\hat{\mathbf{x}}$ spinning direction.

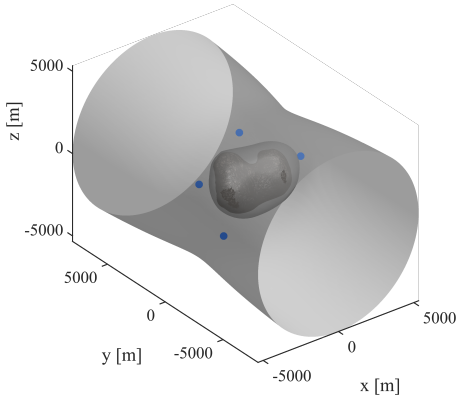

(b) $\hat{\mathbf{y}}$ spinning direction.

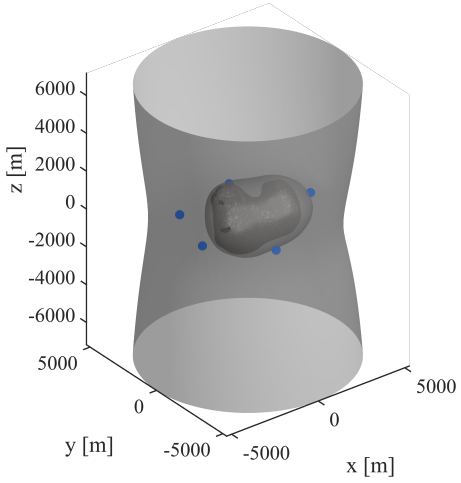

(c) $\hat{\mathbf{z}}$ spinning direction.

Figure 5.5: Equilibrium points and spinning direction, for 67P Churyumov-Gerasimenko. The blue dots are the equilibrium points.

celestial objects or binary systems. They allow obtaining general conclusion on the global phenomena, but they lack of the required accuracy for certain applications. Their results have been here exploited as reference solutions for the validation of the model.

Approximated techniques are often able to find periodic solutions close to the surface of an irregular body. Some references use very simple approximations of the shape of the body to compute families of periodic orbits, similarly to what is usually done in the framework of the circular restricted three-body problem. Periodic trajectories exist also when a complex dynamics is considered, but very often, a solution loses its periodic properties if it is simulated with an enhanced model. In real applications this is not a problem, because the real operations of a space mission take always into account the necessity of *station keeping*. In this regard, the outcomes of an accurate dynamical model can be compared with the approximated results of a lower fidelity technique, in order to evaluate the station keeping effort to achieve a particular and well-behaved orbit.

In this work, the trajectories are computed starting with arbitrary initial conditions. These are obtained exploiting the results of the analysis in section 5.2 and the information coming from an equivalent Keplerian motion. They are propagated in time for an arbitrary amount of time and their results are shown to highlight some particular and interesting characteristic of these dynamical environments. As already said, single simulations have no general validity, yet diverse features can be highlighted to have a deeper understanding of this problem.

Typical Orbits An infinite number of orbits exist around an irregularly-shaped object; each of them is identified by certain characteristics, such as stability level or geometry. In the following four typologies of orbits are reported. They are not representative of all the possible orbital geometries, but they provide a wide overview of possible stable orbits around irregular objects. In these simulations, the rotation axis of the main attractor is initially aligned with one of the principal inertia axes. The perturbative effects act on the coupled dynamics, and despite the rotational dynamics remains very close to the uniform one, the asteroids or the comet are in a non-principal rotation state.

In figures 5.6 and 5.7, two *transversal* spatial orbits are shown. They are called transversal because the orbit in the inertial frame is perpendicular to the equatorial plane. In the first kind, figure 5.6, the orbital period is comparable with the rotation period of the main attractor and

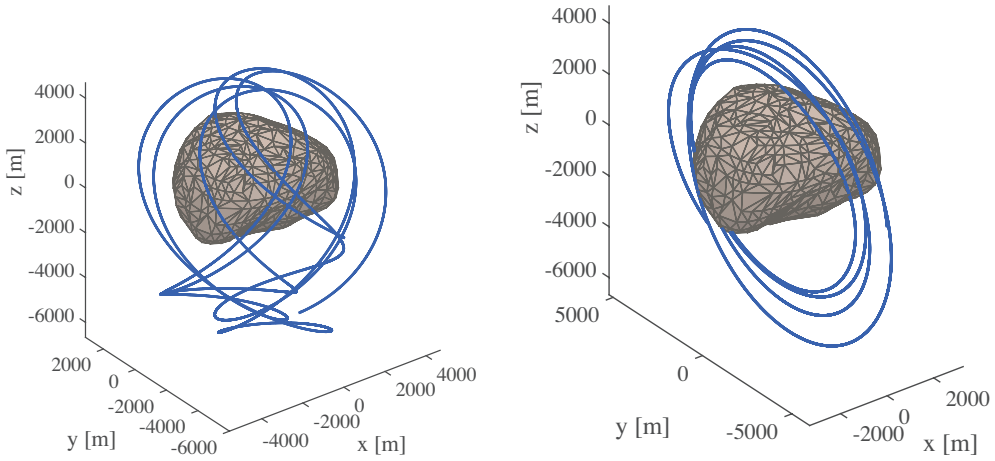

(a) Body-fixed reference frame. (b) Inertial reference frame.

Figure 5.6: Transversal orbit of first kind around 1580 Betulia. Spinning direction at $t = 0$ aligned with $\hat{\mathbf{z}}$.

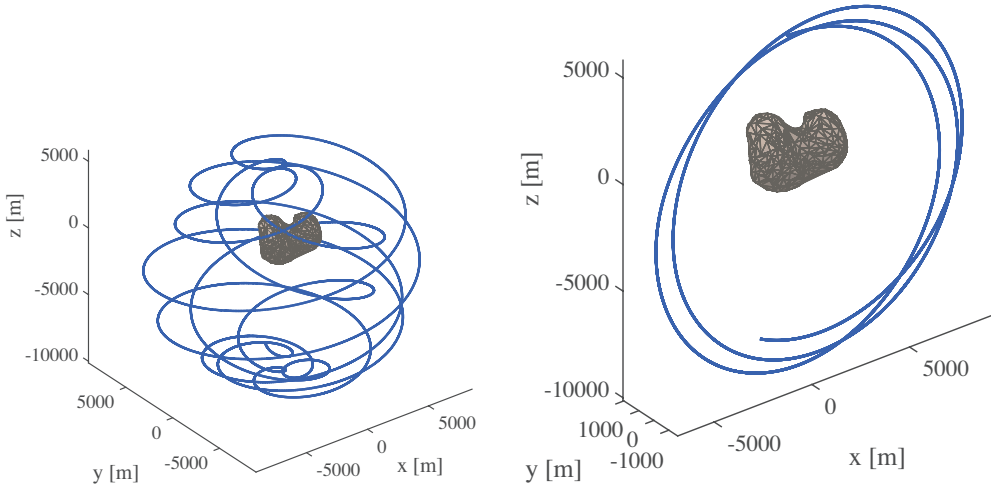

(a) Body-fixed reference frame. (b) Inertial reference frame.

Figure 5.7: Transversal orbit of second kind around 67P Churyumov-Gerasimenko. Spinning direction at $t = 0$ aligned with $\hat{\mathbf{z}}$.

the orbit in the rotating body-fixed frame stays on one side of the main body. This type of orbit can be exploited if the particle has to be always on one side of the irregular object. In the other simulation, figure 5.7,

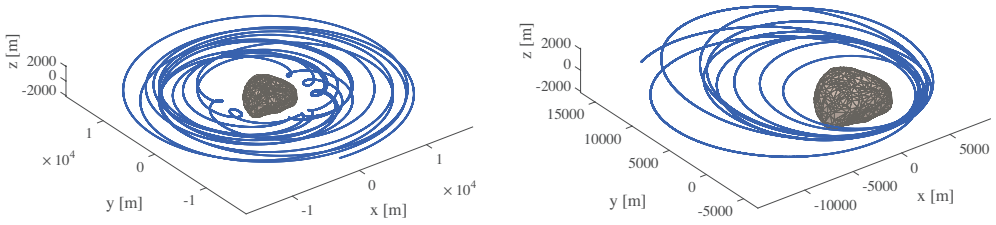

(a) Body-fixed reference frame.

(b) Inertial reference frame.

Figure 5.8: Planar equatorial orbit around 1580 Betulia. Spinning direction at $t = 0$ aligned with $\hat{\mathbf{z}}$.

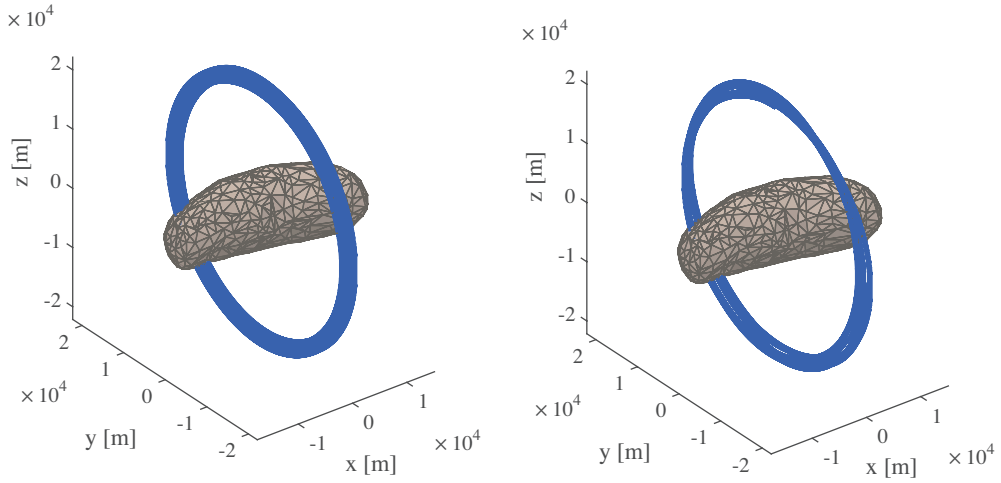

(a) Body-fixed reference frame.

(b) Inertial reference frame.

Figure 5.9: Planar equatorial orbit, axial, around 433 Eros. Spinning direction at $t = 0$ aligned with $\hat{\mathbf{x}}$.

the orbital period is different from the rotation period of the primary and the trajectory evolves all around the comet. If the period of the orbit is commensurable with the rotational period of the main body, the spatial trajectory can be periodic and it is called *resonant*; this typology of orbits has good stability properties. They are interesting for practical applications since all the surface of the main object is covered from this trajectory. Transversal orbits are a particular case of spatial orbit, whose motion is the whole three-dimensional space.

In figures 5.8 and 5.9, two *planar* orbits are shown. These are trajectories evolving in the equatorial plane of the main attractor, and can be denoted as *retrograde* or *prograde* orbits, as defined by the direction of the motion of a particle with respect to the direction of the rotation of the

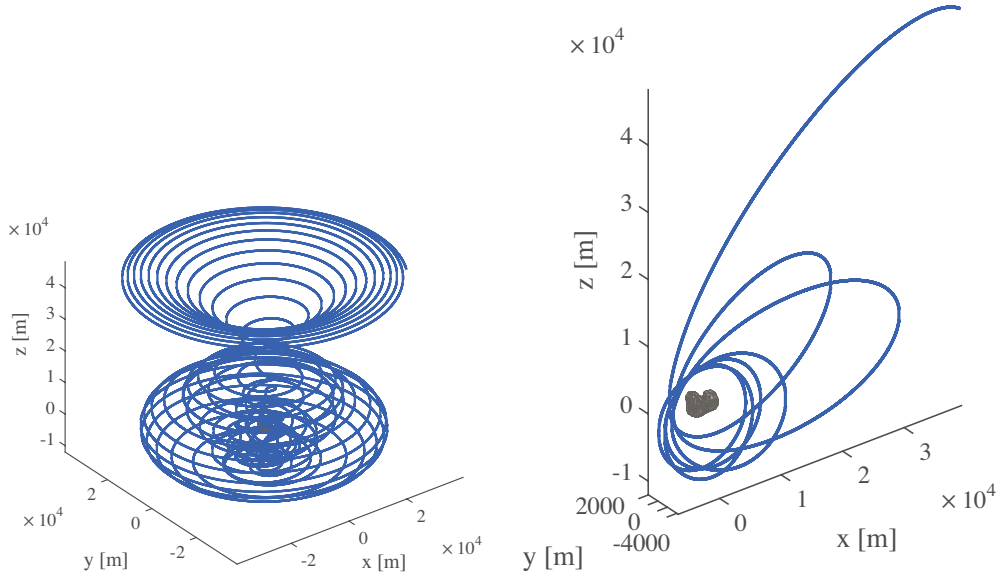

(a) Body-fixed reference frame.

(b) Inertial reference frame.

Figure 5.10: Transversal orbit around 67P Churyumov-Gerasimenko, $t_{Sim} = 30\,\mathrm{d}$. Spinning direction at $t = 0$ aligned with $\hat{\mathbf{z}}$. Real rotation dynamics of the comet.

body in inertial space. In this paragraph, both orbits are retrograde. The planar orbits have a good stability level and they could be interesting for practical applications because of their two-dimensional evolution. The orbit in figure 5.9 is defined as *axial* since the body is elongated in the direction orthogonal to the plane of motion. In this example, the real spinning direction of the asteroid 433 Eros is not considered.

If these orbits are simulated for a longer period, the evolution is obviously diverging, because of the complex perturbed dynamics that is propagated. However, the good stability properties of these typical orbits maintain the motion in proximity of the main body for an acceptable period, and according to the requirements of the mission, the station keeping could be avoided. In the case of the transversal orbit around the comet 67P Churyumov-Gerasimenko, the simulations for a period of $30\,\mathrm{d}$ is shown in figure 5.10. The initial conditions are the same of figure 5.7.

Prograde and Retrograde Motion The analysis of the difference between the planar direct and retrograde motion is performed around the asteroid Toutatis, which is in non-principal rotation state. In this case,

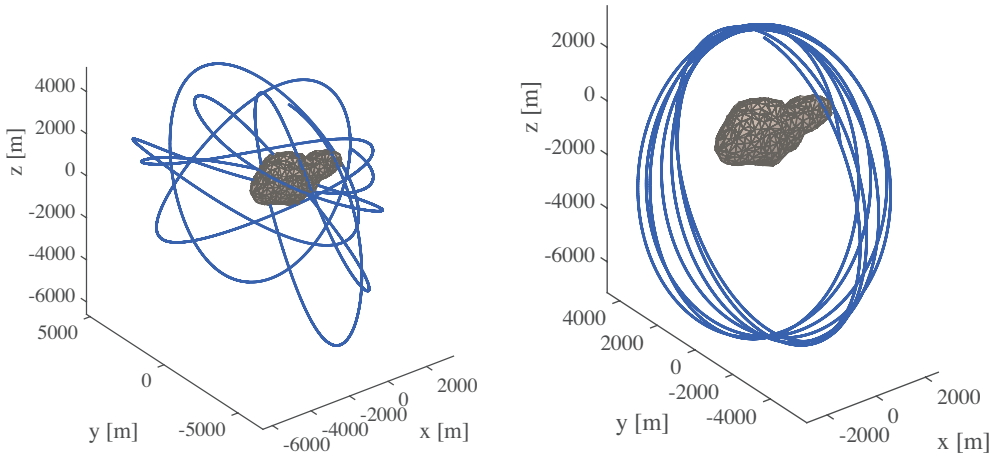

(a) Body-fixed reference frame.

(b) Inertial reference frame.

Figure 5.11: Prograde quasi-axial orbit around 4179 Toutatis, $t_{Sim} \sim 5\,\mathrm{d}$. Real rotation dynamics of the asteroid.

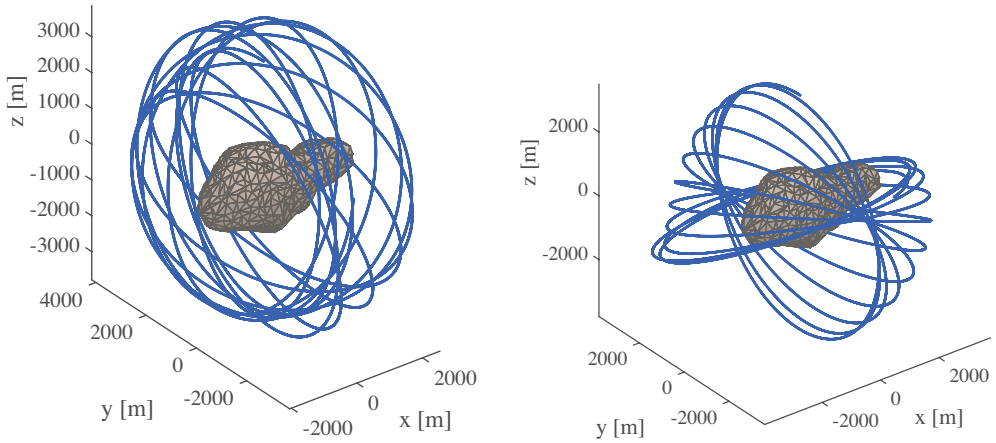

(a) Body-fixed reference frame.

(b) Inertial reference frame.

Figure 5.12: Retrograde quasi-axial orbit around 4179 Toutatis, $t_{Sim} \sim 5\,\mathrm{d}$. Real rotation dynamics of the asteroid.

the orbit is started with the initial conditions to generate a quasi-axial trajectory and two simulations are run, reversing the direction of rotation between the two different cases. In this way, a prograde and a retrograde motions are obtained. The simulation time is $t_{Sim} \sim 5\,\mathrm{d}$.

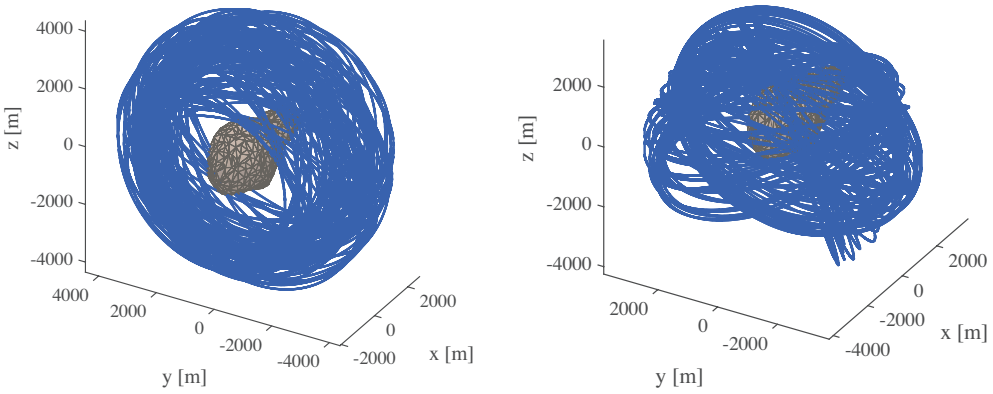

(a) Body-fixed reference frame.

(b) Inertial reference frame.

Figure 5.13: Retrograde quasi-axial orbit around 4179 Toutatis, $t_{Sim} = 30\,\mathrm{d}$. Real rotation dynamics of the asteroid.

The results are shown in figures 5.11 and 5.12 and it is immediately evident how the stability of the retrograde motion is higher with respect to the prograde one. This is a general conclusion for a planar motion around an irregular object; hence, the axial orbits in these complex environments are more interesting if retrograde with respect to the rotation of the main attractor. In figure 5.13, the same motion is propagated for $30\,\mathrm{d}$; the stability of the retrograde orbit is impressive. This is a perfect solution for applications around this particular object in non-principal rotation state. Obviously, this is not the only existing stable orbit around Toutatis, and many more can be found with different initial conditions. Exploiting a continuation algorithm, a family of orbits of the same kind can be discovered; this is valid in general for any stable orbit around a particular attractor.

The effect of the non-principal rotation state is evident looking at the differences between the inertial and the rotating representations for principal and non-principal rotators. To have a more clear view of this concept, a transversal orbit around 4179 Toutatis is shown in figure 5.14.

Comparing the results for the tumbling asteroid with the ones for the principal rotators, the effects of a complex rotational dynamics are evident. Both the motions, in the rotating frame and in the inertial system, show large out of plane variations of the orbit, which are due to the complex interaction between the dynamics of the particle and the rotational motion of the primary. In general, the non-principal rotation

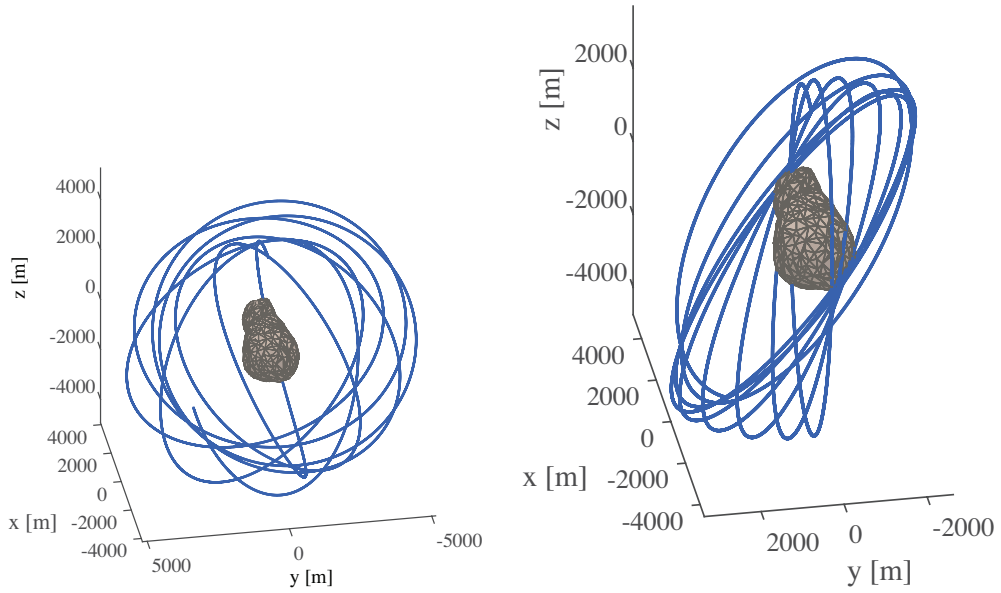

(a) Body-fixed reference frame.

(b) Inertial reference frame.

Figure 5.14: Transversal orbit around 4179 Toutatis, $t_{Sim} \sim 5\,\mathrm{d}$. Real rotation dynamics of the asteroid.

of the main attractor increases the complexity of the whole coupled dynamics; thus, in these situations, the trajectories must be carefully designed. For 4179 Toutatis this problem is reduced thanks to its elongated and quasi-axisymmetric shape; furthermore, the large bulge on one side of the body enhances the stability of orbits around that region of the asteroid.

Influence of the Rotational State The influence of the rotational state of the main attractor on the surrounding dynamics deserves additional attention. Especially if the mission design process has to be performed around a body, whose rotational state is not accurately known. In this analysis, the motion of a particle is simulated around 433 Eros; the initial orbit is of the axial type around the object that is rotating around its minimum inertia axis. Then other simulations are run with the rotation axis direction inclined with respect to the principal inertia axis; the step in the inclination of the initial axis is of $5°$. The results are shown in figure 5.15, and they are labelled with the angle between the initial rotation axis of the simulation and the minimum inertia axis of the

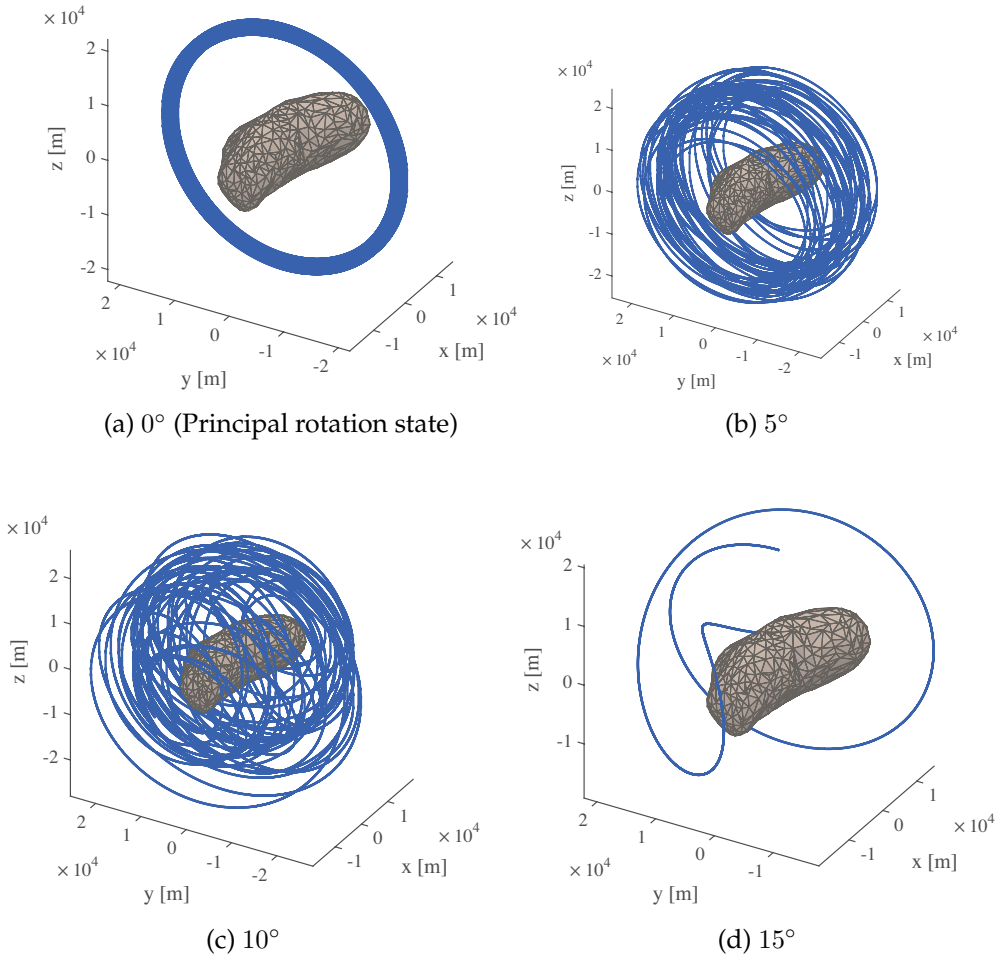

(a) 0° (Principal rotation state)

(b) 5°

(c) 10°

(d) 15°

Figure 5.15: Influence of the rotational state on particle dynamics around 433 Eros, $t_{Sim} \sim 5\,\mathrm{d}$. Arbitrary rotation dynamics of the asteroid.

asteroid. The perurbative effects are acting on the dynamics of the system, which is propagated for $t_{Sim} \sim 5\,\mathrm{d}$.

From this test, it can be argued that the accuracy in the determination of the rotation axis of a celestial body is extremely important to propagate the coupled dynamics in its vicinity. In this particular case, an error of $15°$ on the spin direction could determine a catastrophic epilogue for a hypothetical space mission around Eros. In fact, in figure 5.15d the particle crashes on the surface of the body in a short time. In general, a small error on the rotational state of the main attractor determines large uncertainties in the orbital dynamics, and if a mission design process

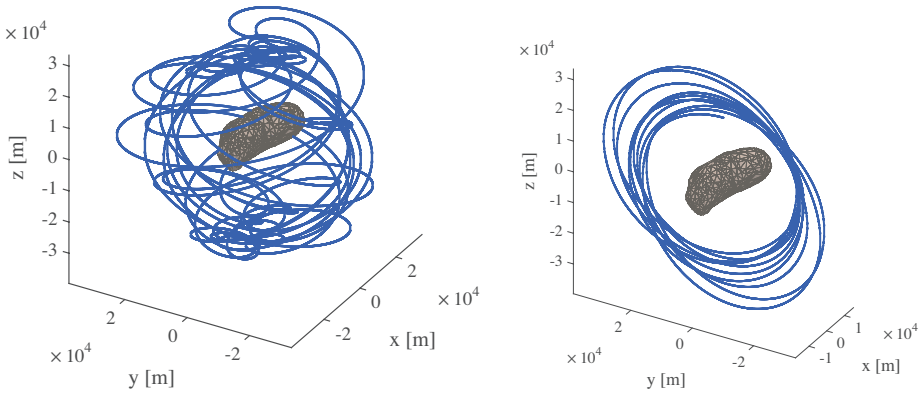

(a) Body-fixed reference frame.

(b) Inertial reference frame.

Figure 5.16: Transversal orbit around 433 Eros, $t_{Sim} = 30\,\mathrm{d}$. Spinning direction at $t = 0$ aligned with $\hat{\mathbf{z}}$. Real rotation dynamics of the asteroid.

has to be carried out, a large station keeping action must be included in the budgets of the system.

In the limits that the body is rotating around a different inertial axis, the same initial conditions evolve in a completely different orbit of another family. In figure 5.16, the real dynamics of the asteroid is propagated with the same initial condition of figure 5.15. The resulting orbit is a transversal spatial orbit with good stability properties; it is a quasi-resonant orbit for this system and allows a full coverage of the surface of the asteroid.

5.4 Effect of Perturbing Torques

At this point of the analysis, it is reasonable to wonder which is the practical effect of the perturbations included in the rotational dynamics of the primary. The goal is to estimate the accuracy of the unperturbed model, together with the length of the timespan where the dynamics without perturbation is reliable, and in a first approximation, can be used in place of the full dynamical model. The best way to accomplish this analysis is through the use of the orbital elements introduced in section 5.1.1. In particular, the evolution of the osculating orbital parameters is computed, starting with the same initial conditions, both for the perturbed and for the unperturbed model. Then, the difference between the two simulations is evaluated and analysed.

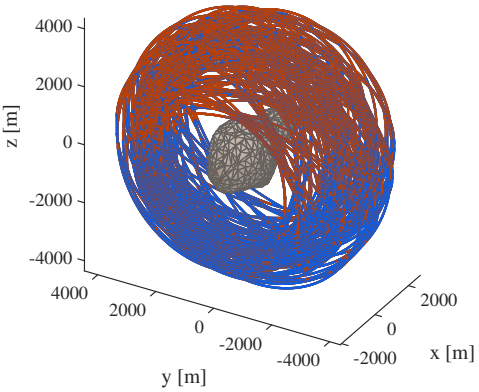

(a) Body-fixed reference frame trajectories. (Blue line with perturbations, red line without.)

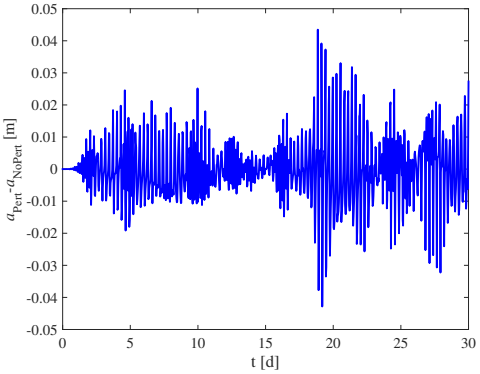

(b) Semi-major axis difference.

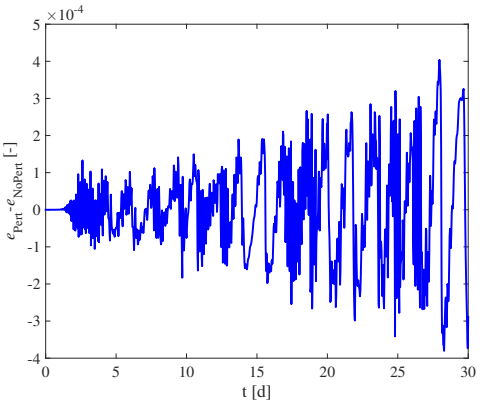

(c) Eccentricity difference.

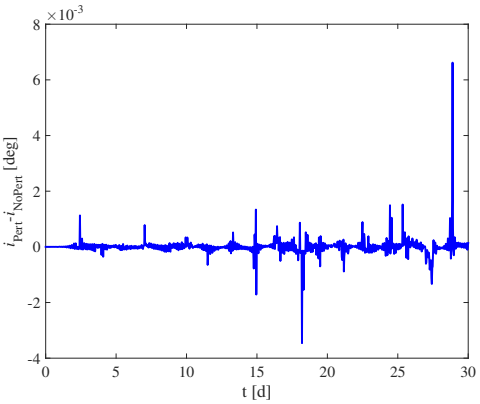

(d) Inclination difference.

Figure 5.17: Influence of the perturbations on particle dynamics around 4179 Toutatis, $t_{Sim} \sim 30\,\mathrm{d}$. Real rotation dynamics of the asteroid.

Here, the results obtained on 4179 Toutatis and 67P Churyumov-Gerasimenko are shown and compared in figures 5.17 and 5.18. The dynamics is propagated for a period of $30\,\mathrm{d}$ and the study is carried out on the differences in the osculating semi-major axis, eccentricity and inclination.

It must be noted that the irregular trend in figures 5.17b to 5.17d and figures 5.18b to 5.18d is due to the extremely erratic evolution of the osculating parameters. The complex dynamics of a particle around an irregular celestial body is remarkably different from the classical two-body problem and the osculating elements have large fluctuations

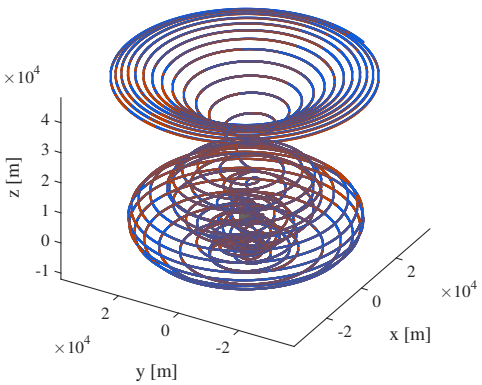

(a) Body-fixed reference frame trajectories. (Blue line with perturbations, red line without.)

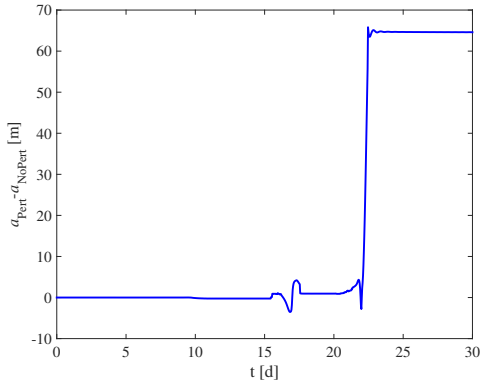

(b) Semi-major axis difference.

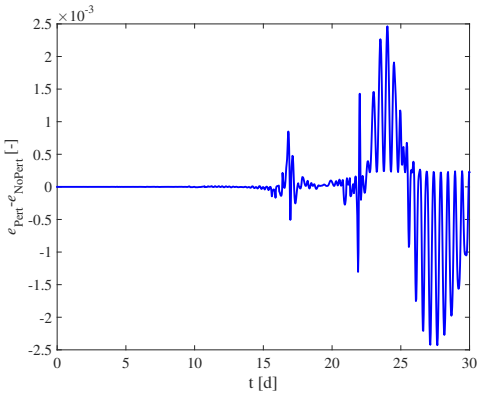

(c) Eccentricity difference.

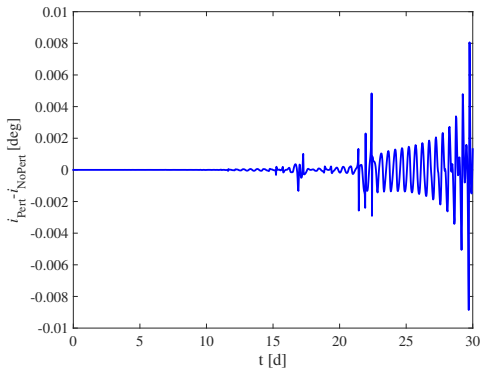

(d) Inclination difference.

Figure 5.18: Influence of the perturbations on particle dynamics around 67P Churyumov-Gerasimenko, $t_{Sim} \sim 30\,\mathrm{d}$. Real rotation dynamics of the comet.

in time, which are also reflected in the differences between the two different simulations. However, the general progression is important for the current analysis and it can be clearly outlined in the aforementioned plots.

From the previous figures, it is evident that the perturbing torques on the rotational dynamics of the main attractor have a small influence on the dynamics of the particle P. However, their effect is not completely negligible, especially if a long simulation time is taken into account. In fact, the difference between the full model and the unperturbed one is increasing in time; this particular trend has been detected in all the investigations that have been carried out for all the available environments.

A tolerable level of accuracy depends on the particular application, but in general, after $30 - 50\mathrm{d}$ the difference is noticeable and the perturbing torques must be included in the model for such a long timespan. In addition, the real perturbations act also directly on the orbital dynamics of the particle and the actual error of the completely unperturbed simulation is even larger.

The effect of the perturbations depends also on the particular environment that is considered. For instance, the simulation around the comet 67P is more affected by the perturbations if compared with the one about Toutatis. This can be explained considering the substantial influence of the perturbing torques on the comet, because of its low density with respect to the one of the asteroid. In this case, the extension of the surfaces of the two objects is comparable, but they have dissimilar inertia properties. Thus, they experience similar perturbing torque, but they undergo different angular accelerations. Moreover, the simulated orbital motion around the comet is less stable and evolves quite far from the central attractor; therefore, the importance of the coupling terms between the rotational dynamics and the orbital one is greater, and the influence of the perturbations is more relevant.

Globally, the perturbations on the rotational dynamics of the main attractor can be neglected for short mission with $t < 10\,\mathrm{d}$. Considering also the disturbances that act directly on P the validity of the unperturbed model is probably limited to some hours. Obviously, if the spacecraft is supposed to fly far from the irregular object the tolerance on the admissible accuracy can be a bit more relaxed, since the risk of collision is lower. So, the higher error in neglecting the perturbations far from the primary is compensated by the reduced level of accuracy that is required.

The additional computational time that is needed to evaluate the contribution of the perturbations is $\sim 75\%$ of the time required to run the simulation without perturbations. This greater computational effort is mainly due to the surface torques that are computed on each face of the polyhedron model, taking also into account the self-shadowing effect. In this work, the same number of faces that is used to evaluate the gravitational field is then used to compute the perturbing torques. The speed performances of the algorithm can be increased if the gravitational field and the perturbing contributions are evaluated at the same time in a single loop, though in this case, the code is less flexible and the accuracy levels cannot be singularly tuned.

In this chapter, some particular results have been shown and discussed. They depend on the specific dynamical environment and initial

conditions; hence, they have no general validity. But, they also highlight several insightful features of the dynamics of a particle in the vicinity of an irregularly-shaped body. These can be used to have some preliminary understanding about this class of problems, and to have some reference results that can be always exploited as benchmarks for future applications.

Chapter 6

Conclusions

This thesis deals with the coupled dynamics of a particle around an irregularly-shaped body. To describe the motion of this particle the evaluation of the gravity field generated by the main body is essential, and in this research work, two different enhanced modelling techniques have been exploited for this purpose: the mascons and polyhedral approach. Moreover, a complete and accurate representation of the dynamical environment in the vicinity of an asteroid or a comet is only possible when their rotational dynamics is taken into account. Thus, a model to understand the evolution of the rotation state of the irregular body has been implemented, including the effect of the most influencing natural perturbations. Both the gravitational and the rotational contributions have been considered together to develop a model able to accurately describe the orbital dynamics around a non-centrobaric body.

The resulting dynamical environment has been characterized by means of simple particular solutions, such as the Zero Velocity Surfaces or the equilibrium points. In addition, several specific initial conditions have been propagated, and despite their circumscribed validity, they spotlight some insightful and important traits of the dynamics of a particle around one of these singular bodies. In fact, the existence of planar and spatial orbits has been shown. The former have been classified retrograde or planar, according to the direction of motion of the particle with respect to the rotation axis of the primary; while, the latter, generically resonant, if the ratio of their period with the rotational period of the main body is a rational number. Furthermore, the stability of these trajectories, the influence of the rotational state and the effect of perturbing torques have been assessed, in a way to have a complete overview of the problem and to test the accuracy of the model.

In general, the description of these environments should be carried out with a continuous balance between fidelity of results and required computational time; there is not a unique possibility to solve this trade-off, and the final decision depends on the particular application. For instance, the advanced mission design process is greatly demanding in terms of accuracy, but the real time operations to be managed by the on-board computer of a space probe require fast and reliable algorithms. Hence, in several practical circumstances, the optimum Lo-Fi model, which has been defined and employed in this research work, is extremely helpful. The developed algorithms make extensive use of parallel computing techniques; however, the code can be optimized further and a huge boost to the computational speed is possible exploiting simple and light programming language, such as C or Fortran. In this thesis, the entire structure of the different tools has been implemented with MATLAB®. The validity of each result has been continuously verified through direct visualization techniques and comparisons of simple physical quantities.

6.1 Gravity Models

The employed enhanced modelling techniques to describe the gravitational field of an irregular celestial object have their own advantages and drawbacks. They do not have convergence problems, thus, they allow having a decent representation of the gravitational field in all the surrounding space, including the surface of the body. The level of achievable precision can be easily tuned adjusting the number of discretizing elements, and consequently, they are extremely flexible.

The polyhedron approach, especially if the representation of the body is particularly accurate, produces superlative results, but it is computationally expensive. The fidelity of the field is only limited by the precision of the shape representation; moreover, the Laplacian of the potential is immediately available to determine if a field point is outside or inside the body. The required time to evaluate the field is linearly increasing with the number of polyhedron's faces, while the errors of the model decrease with the square root of the same quantity. Having this information, an acceptable level of accuracy and computational effort can be established according to the current needs.

The mascons approach is markedly faster and produces good results if the field point is far enough from the surface of the body. In general, it produces poor results if it is applied to elongated bodies. The optimized

version of this technique improves the performances of the standard version up to its theoretical limit: the error decreases by one order of magnitude for an increase of three orders of magnitude in the number of mascons. However, over a certain number of point masses, the optimization process is not effective anymore and the gridded mascons approach is sufficient to have an acceptable result.

With the analysis, which has been conducted in this research work, the most efficient and effective gravity model is a combination of both approaches. The resulting optimum Lo-Fi technique uses a polyhedron with a moderate number of faces to compute the field close to the surface of the body, and the optimized mascons with a reasonable number of masses when the distance from the centre of mass is large enough. The switch between the two models happens at a distance where the gap between the two techniques is extremely limited, in a way to maintain the continuity of the field.

6.2 Rotational Dynamics

The understanding of the rotational dynamics of irregular celestial bodies is essential to describe the dynamical environment in their vicinity. Not only, the knowledge about the evolution of their rotation state can be used to investigate the formation and the evolution of the Solar System, or to accurately determine the risk of impact from potentially hazardous objects with the Earth.

Obviously, the motion is extremely affected by the presence of the perturbations. Their effect is different for each single case, but in general, radiative torques and third body gravitation are the most disturbing terms. However, only the radiation that acts in the direction normal to the surface has a relevant secular contribution. Hence, the long-term evolution of the rotational dynamics of an irregular celestial body is mainly influenced by the YORP effect. Yet, since the non-periodic influence of the perturbations is particularly small, the time scale of these secular effects is exceptionally long and they can be neglected for preliminary short-term simulations.

Nevertheless, all the perturbing torques determine fluctuations in the rotation state of the analysed object. These short period variations are connected with the orbital dynamics in the vicinity of these object and their study contribute to increase the accuracy of the developed coupled dynamical model.

The perturbations have been meticulously modelled, exploiting the polyhedron shape to evaluate the rotational inertia properties and to accurately describe the interaction of radiations with the surface of the body, taking into account shadows and self-shadowing phenomenon.

Per contra, the precision of the available data is not always guaranteed; therefore, a sensitivity analysis has been performed to ensure the validity of the conclusions regardless of the fidelity to which the properties of the body are determined. The results show that the dynamical model is robust enough, and within the typical range of uncertainty, the simulations are sufficiently correct. The global evolution of the motion is preserved, and it is reasonable to use the accurate dynamical model, even though the physical and dynamical characteristics of the celestial object are just a preliminary estimate.

6.3 Coupled Dynamics

The investigation about the motion of a particle near irregularly-shaped bodies has been supported by the results gathered analysing the already mentioned topics. Indeed, the study of the techniques to model the gravitational field and the inspection of the rotational dynamics of a minor celestial object are crucial to implement an accurate model to simulate this peculiar dynamical environment.

The characteristics of these surroundings are subordinate to the rotational state of the main attractor. If this body is in uniform rotation state, an integral of the motion exists and the equations of motion, in the body-fixed frame, are time invariant. Notwithstanding, this is not true in all the situations, and in particular, it is not verified when the dynamics is perturbed by external torques. In these conditions, the equilibrium solutions and the Zero Velocity Surfaces are time-varying and they can be used only for a preliminary understanding of the evolution of the motion. The number of equilibrium solutions and the shape of the bounding surfaces are determined by the geometry and the rotational state of the primary, and each condition must be singularly analysed.

The stability of the motion has to be assessed for each set of initial conditions; even though, in general, the retrograde planar and the resonant orbits are notably stable. In addition, the trajectories of the particle are highly shaped by the rotation state of the main attractor, and as a consequence, the uncertainty in the determination of the direction of the spinning axis must be as small as possible. An error of few degrees can

determine a catastrophic epilogue for a space mission in the vicinity of an asteroid or a comet.

Despite the perturbing torques have a limited effect on the dynamics of the orbiting particle, their effect cannot be neglected, and in a long simulation, the difference between the ideal and the perturbed motion is not completely insignificant.

Finally, considering the inevitable uncertainties and approximations in simulating the dynamics in these unique environments, the station keeping must be carefully planned along the mission design process. For this purpose, additional sensitivity analyses can be carried out with the developed model, which can also be exploited to run accurate simulations when the description of the mission scenarios is detailed enough.

6.4 Future Works

This research work deals with several ongoing problems in the field of orbital dynamics, planetary sciences and space engineering. The available literature is surprisingly wide, and this thesis is just a single step further towards the study of this complex and broad, but fascinating, topic. However, all the existing studies on this matter are quite recent, and a lot of research work has yet to be done. The future works can evolve in two different directions.

A part of the research can be directed towards the increase in the accuracy of the model. In fact, the perturbative effects can be directly added to the dynamics of the particle, and not only to the rotational motion of the main attractor. Furthermore, the real orbital path of the asteroid or the comet can be easily included in the whole dynamical model, and even in this case, the perturbations can be considered. As a possible last improvement in the fidelity of the model, the irregular gravity field can be evaluated including the possible density variations within the volume of the main attractor. Yet, this information must be accessible, and therefore, this last point is subjected to the availability of an accurate description of the mass distribution of the real body.

A different direction for future research works is related to the reduction of the fidelity of the model. As example, the gravity field can be computed with a simple harmonic series expansion, including only the first terms of the series, or with the exact field for a triaxial ellipsoid [40]. In this way, the accuracy of the results is lower, close to the surface of the body in particular, but some general conclusions can be delineated. Thus, the analysis is independent from the particular environment and

some additional investigations can be performed, thanks to the reduced computational burden. For instance, families of periodic orbits can be computed and their stability evolution can be studied, or the dynamical environment can be analysed by means of Poincarè maps. This dynamical tool is extremely useful to understand the evolution of the region of stability around the body and to perform useful bifurcation analyses, but it is computationally expensive; so, a very low fidelity model allows a reasonable elaboration time and do not restrict the analysis to a single specific situation.

An additional application of this dynamical model is the one related to the study of binary systems of asteroid. In this problem two non-spherical objects are taken into account and their relative motion can be studied, as well as the dynamics of a particle in the binary environment. This argument is of great interest, either for future missions to binary objects, or to anticipate the circumstance of encountering an undetected secondary body during a mission initially planned around a single body.

A completely different problem, which is present in the context of mission design, is the capability to compute transfers to get in the vicinity of irregularly-shaped bodies. Here, it is important to note that the gravitational field might be unknown before the close encounter; hence, different sensitivity analyses are necessary in order to be ready to adjust the planned trajectory when a precise model of the gravitational field is available.

Finally, it must be remembered that the propagation of trajectories around a rotating irregular celestial objects is computationally expensive. Fortunately, the developed algorithm can be improved in several aspects. The global structure is still prone to be boosted, using a lighter and simpler programming language and removing some cumbersome sections that were necessary to assess the validity of the code. Additionally, the meshing algorithm can be enhanced including the possibility of a non-uniform resolution of the polyhedron, in order to have a finer discretization only where it is needed. In this way, it is possible to decrease the required computational time, while maintaining the same fidelity of the model. The efficiency of the code can be further increased exploiting not only the parallel computing techniques, but also the Graphic Processing Unit (GPU) computation, in a way to use thousands of processors to complete numerical operations.

This research area is extremely active, and the space community is eager to increase the scientific understanding of these topics. Thanks to

the recent progresses of the space mission objectives, the spacecraft of today are performing incredible and engaging tasks across all the Solar System, but the missions of tomorrow will be even more challenging and intriguing. This should not be seen as a limitation, since the human being cannot remain confined to his comfort zone, but he has to continually challenge himself, exploring and discovering new worlds, which also include asteroids, comets, planets orbiting around the Sun, the outer space and beyond.

Symbols and Notations

Symbol	Description
G	Gravitational constant
U	Gravitational potential
V	Pseudo-potential function
r	Distance from a point mass
m	Mass of a point mass
M	Mass of the body
V	Volume of the body
σ	Density of the body
$\boldsymbol{\omega}$	Angular velocity of the body
$\boldsymbol{\Omega}$	Constant angular velocity of the body
$\mathbf{I}$	Inertia tensor
I_x	Minimum inertia moment
I_y	Intermediate inertia moment
I_z	Maximum inertia moment
I_D	Dynamic inertia
δ	Obliquity
$\mathbf{r}_f$	Vector from the field point to any point in the polyhedron's face plane
$\mathbf{r}_e$	Vector from the field point to any point on a polyhedron's edge
ω_f	Solid angle subtended by a polyhedron's face as viewed from the field point
L_e	Potential of a polyhedron's edge
$\mathbb{F}_f$	Dyad associated with a polyhedron's face
$\mathbb{E}_e$	Dyad associated with an polyhedron's edge
N_v	Number of polyhedron's vertices
N	Number of polyhedron's faces
N_m	Number of mascons

Continued on next page.

Continued from previous page.

Symbol	Description
B	Rotating body-fixed reference frame
I	Inertial reference frame
$\mathbb{I}^{3\times3}$	3×3 identity matrix
ϕ	First Euler angle
θ	Second Euler angle
ψ	Third Euler angle
$\boldsymbol{V}$	State Vector of the dynamical model
$\mathbf{A}$	Direction cosine matrix from I to B
P	Field point
$\hat{\mathbf{x}}$	Minimum inertia direction
$\hat{\mathbf{y}}$	Intermediate inertia direction
$\hat{\mathbf{z}}$	Maximum inertia direction
$\hat{\mathbf{s}}$	Body-Sun direction
$\hat{\mathbf{n}}$	Surface normal direction
$\mathbf{p}$	Position vector in B
$\mathbf{p}_I$	Position vector in I
$\boldsymbol{\rho}$	Distance from the centre of mass of the body
$\mathbf{h}$	Angular momentum vector in B
$\mathbf{m}$	External torque in B
$\mathbf{m}_{GG}$	Third body gravitation torque
$\mathbf{m}_{SRP}$	Solar radiation pressure torque
$\mathbf{m}_{YORP}$	YORP torque
$\mathbf{m}_D$	Dissipation of internal energy torque
$\mathbf{m}_z$	Torque to change the spin rate
$\mathbf{m}_\delta$	Torque to change the obliquity
J	Jacobi integral
C	Jacobi constant
T	Kinetic energy
E_i	i-th equilibrium point
c_i	i-th direction cosine
c	Speed of light
c_a	Absorption coefficient
c_d	Diffuse reflection coefficient
c_s	Specular reflection coefficient
c_r	Albedo of the body
P_S	Pressure due to solar radiation

Continued on next page.

Continued from previous page.

Symbol	Description
F_S	Flux density of solar radiation
A	Area of a polyhedron's face
D_E	Diameter of the body along $\hat{\mathbf{x}}$
D_P	Diameter of the body along $\hat{\mathbf{z}}$
a_{eq}	Averaged equatorial radius
υ	Geometric flattening of the spheroid
α	Angle between $\hat{\mathbf{s}}$ and $\hat{\mathbf{n}}$
k	Rigidity of the material
Q	Quality factor
γ	Angle between $\mathbf{h}$ and $\hat{\mathbf{x}}$ or $\hat{\mathbf{z}}$
μ	Gravitational parameter
a	Semi-major axis
e	Eccentricity
i	Inclination
ε	Keplerian specific mechanical energy
R_S	Radius of the orbit of the body
$\mathrm{T}_{2\pi}$	Rotation period of the body
T_P	Orbital period of the particle
T_S	Orbital period of the body
t_{Sim}	Simulation time
$\mathrm{t_C}$	Computational time

Bibliography

[1] Barucci, M., Bockelee-Morvan, D., Lecacheux, J., Brahic, A., and Clairemidi, S., "Asteroid spin axes-two additional pole determinations and theoretical implications", *Astronomy and Astrophysics*, vol. 163, pp. 261–268, 1986.

[2] Bate, R. R., Mueller, D. D., and White, J. E., *Fundamentals of Astrodynamics*. Dover Publications, 1971.

[3] Bellerose, J. and Scheeres, D. J., "Restricted full three-body problem: Application to binary system 1999KW4", *Journal of guidance, control, and dynamics*, vol. 31, no. 1, pp. 162–171, 2008.

[4] Bottke Jr, W. F., Vokrouhlicky, D., Rubincam, D. P., and Broz, M., "The effect of Yarkovsky thermal forces on the dynamical evolution of asteroids and meteoroids", *Asteroids III*, vol. 395, 2002.

[5] Breiter, S. and Michalska, H., "YORP torque as the function of shape harmonics", *Monthly Notices of the Royal Astronomical Society*, vol. 388, no. 2, pp. 927–944, 2008.

[6] Britt, D., Yeomans, D., Housen, K., and Consolmagno, G., "Asteroid density, porosity, and structure", *Asteroids III*, vol. 1, pp. 485–500, 2002.

[7] Chappaz, L. P. R., *The Dynamical Environment in the Vicinity of Small Irregularly-Shaped Bodies with Application to Asteroids*. Master of Science Thesis, Purdue University, 2011.

[8] Cicalò, S. and Scheeres, D., "Averaged rotational dynamics of an asteroid in tumbling rotation under the YORP torque", *Celestial Mechanics and Dynamical Astronomy*, vol. 106, no. 4, pp. 301–337, 2010.

[9] Colagrossi, A., *Missioni verso il punto lagrangiano L1 nel sistema Terra-Luna*. Bachelor of Science Thesis, Politecnico di Torino, 2012.

[10] Curtis, H., *Orbital Mechanics for Engineering Students*. Elsevier, 2009.

[11] Descamps, P., Marchis, F., Berthier, J., Emery, J. P., Duchêne, G., De Pater, I., Wong, M. H., Lim, L., Hammel, H. B., and Vachier, F., "Triplicity and physical characteristics of asteroid 216 Kleopatra", *Icarus*, vol. 211, no. 2, pp. 1022–1033, 2011.

[12] ESA, *Rosetta's target: Comet 67P Churyumov-Gerasimenko*, Nov. 2014. [Online]. Available: `http://sci.esa.int/rosetta/14615-comet-67p/`.

[13] ——, *Shape model of comet 67P Churyumov-Gerasimenko*, Oct. 2014. [Online]. Available: `http://sci.esa.int/rosetta/54728-shape-model-of-comet-67p/`.

[14] Ferrari, F., *Formation Flying Dynamics in Circular Restricted Three-Body Problem and Applications to Binary Asteroid Systems*. Master of Science Thesis, Politecnico di Milano, 2013.

[15] Ferrari, F., Lavagna, M., and Howell, K. C., "Trajectory design about binary asteroids through coupled three-body problems", *2nd IAA Conference on Dynamics and Control of Space Systems*, 2014.

[16] Geissler, P., Petit, J. M., Durda, D. D., Greenberg, R., Bottke, W., Nolan, M., and Moore, J., "Erosion and ejecta reaccretion on 243 Ida and its moon", *Icarus*, vol. 120, no. 1, pp. 140–157, 1996.

[17] Goldstein, H., *Classical Mechanics*. Pearson Education, 1962.

[18] Greenberg, M. D., *Foundations of applied mathematics*. Englewood Cliffs, New Jersey: Prentice-Hall, 1978.

[19] Guzzetti, D., *Large Space Structures Dynamics in a Multi-Body Gravitational Environment*. Master of Science Thesis, Politecnico di Milano, 2012.

[20] Hilton, J. L., "Asteroid masses and densities", *Asteroids III*, vol. 1, pp. 103–112, 2002.

[21] Hudson, R. S. and Ostro, S. J., "Shape and non-principal axis spin state of asteroid 4179 Toutatis", *Science*, vol. 270, no. 5233, pp. 84–86, 1995.

[22] Kaasalainen, M., Pravec, P., Krugly, Y. N., Sarounová, L., Torppa, J., Virtanen, J., Kaasalainen, S., Erikson, A., Nathues, A., Durech, J., *et al.*, "Photometry and models of eight near-Earth asteroids", *Icarus*, vol. 167, no. 1, pp. 178–196, 2004.

[23] Kaula, W. M., *Theory of Satellite Geodesy: Applications of Satellites to Geodesy*. Blaisdell Publishing Company, 1966.

[24] Khushalani, B., "Asteroid tetrahedron shape models from spud data", *Current Science Bangalore*, vol. 79, no. 11, pp. 1578–1580, 2000.

[25] Lupishko, D. and Tielieusova, I., "Influence of the YORP effect on rotation rates of near-Earth asteroids", *Meteoritics and Planetary Science*, vol. 49, no. 1, pp. 80–85, 2014.

[26] MacMillan, W. D., *The theory of the potential*. Dover, 1958.

[27] Magri, C., Ostro, S. J., Scheeres, D. J., Nolan, M. C., Giorgini, J. D., Benner, L. A., and Margot, J., "Radar observations and a physical model of asteroid 1580 Betulia", *Icarus*, vol. 186, no. 1, pp. 152–177, 2007.

[28] Markley, F. L. and Crassidis, J. L., *Fundamentals of Spacecraft Attitude Determination and Control*. Springer, Space Technology Library, 2014.

[29] MathWorks, *Genetic algorithm: Matlab R2014b documentation*, Feb. 2015. [Online]. Available: `http://www.mathworks.com/help/gads/genetic-algorithm.html`.

[30] Miller, J. K., Konopliv, A. S., Antreasian, P. G., Bordi, J. J., Chesley, S., Helfrich, C. E., Owen, W. M., Wang, T. C., Williams, B. G., and Yeomans, D. K., "Determination of shape, gravity, and rotational state of asteroid 433 Eros", *Icarus*, vol. 155, no. 1, pp. 3–17, 2002.

[31] Morbidelli, A. and Vokrouhlicky, D., "The Yarkovsky-driven origin of near-earth asteroids", *Icarus*, vol. 163, no. 1, pp. 120–134, 2003.

[32] Mottola, S., Lowry, S., Snodgrass, C., Lamy, P., Toth, I., Rozek, A., Sierks, H., A'Hearn, M., Angrilli, F., Barbieri, C., *et al.*, "The rotation state of 67P Churyumov-Gerasimenko from approach observations with the OSIRIS cameras on Rosetta", *Astronomy and Astrophysics*, vol. 569, p. L2, 2014.

[33] Mysen, E., "An analytical model for YORP and Yarkovsky effects with a physical thermal lag", *Astronomy and Astrophysics*, vol. 484, no. 2, pp. 563–573, 2008.

[34] Nesvorny, D. and Vokrouhlicky, D., "Analytic theory for the Yarkovsky-O'Keefe-Radzievski-Paddack effect on obliquity", *The Astronomical Journal*, vol. 136, no. 1, p. 291, 2008.

[35] Newton, I., *Philosophiae Naturalis Principia Mathematica*. 1686.

[36] Nolan, M. C., Magri, C., Howell, E. S., Benner, L. A., Giorgini, J. D., Hergenrother, C. W., Hudson, R. S., Lauretta, D. S., Margot, J.-L., Ostro, S. J., *et al.*, "Shape model and surface properties of the OSIRIS-REx target asteroid (101955) Bennu from radar and light curve observations", *Icarus*, vol. 226, no. 1, pp. 629–640, 2013.

[37] Ostro, S. J., Hudson, R. S., Nolan, M. C., Margot, J., Scheeres, D. J., Campbell, D. B., Magri, C., Giorgini, J. D., and Yeomans, D. K., "Asteroid radar shape models, 216 Kleopatra", *NASA Planetary Data System*, vol. 16, p. 7, 2004.

[38] Rossi, A., Marzari, F., and Farinella, P., "Orbital evolution around irregular bodies", *Earth Planets and Space*, vol. 51, no. 11, pp. 1173–1180, 1999.

[39] Rubincam, D. P., "Radiative spin-up and spin-down of small asteroids", *Icarus*, vol. 148, no. 1, pp. 2–11, 2000.

[40] Scheeres, D., "Dynamics about uniformly rotating triaxial ellipsoids: Applications to asteroids", *Icarus*, vol. 110, no. 2, pp. 225–238, 1994.

[41] Scheeres, D. J., Ostro, S. J., Hudson, R., DeJong, E. M., and Suzuki, S., "Dynamics of orbits close to asteroid 4179 Toutatis", *Icarus*, vol. 132, no. 1, pp. 53–79, 1998.

[42] Scheeres, D. J., Ostro, S. J., Hudson, R., and Werner, R. A., "Orbits close to asteroid 4769 Castalia", *Icarus*, vol. 121, no. 1, pp. 67–87, 1996.

[43] Scheeres, D. J. and Bellerose, J., "The restricted Hill full 4-body problem: Application to spacecraft motion about binary asteroids", *Dynamical Systems: An International Journal*, vol. 20, no. 1, pp. 23–44, 2005.

[44] Scheeres, D., "Satellite dynamics about asteroids", *Advances in the Astronautical Sciences.*, no. 292, 1994.

[45] ——, "The dynamical evolution of uniformly rotating asteroids subject to YORP", *Icarus*, vol. 188, no. 2, pp. 430–450, 2007.

[46] Scheeres, D., Marzari, F., Tomasella, L., and Vanzani, V., "Rosetta mission: Satellite orbits around a cometary nucleus", *Planetary and Space Science*, vol. 46, no. 6, pp. 649–671, 1998.

[47] Scheeres, D., Williams, B., and Miller, J., "Evaluation of the dynamic environment of an asteroid: Applications to 433 Eros", *Journal of Guidance, Control, and Dynamics*, vol. 23, no. 3, pp. 466–475, 2000.

[48] Sharma, I., Burns, J. A., and Hui, C.-Y., "Nutational damping times in solids of revolution", *Monthly Notices of the Royal Astronomical Society*, vol. 359, no. 1, pp. 79–92, 2005.

[49] Tardivel, S., Michel, P., and Scheeres, D. J., "Deployment of a lander on the binary asteroid (175706) 1996 FG3, potential target of the european Marcopolo-R sample return mission", *Acta Astronautica*, vol. 89, pp. 60–70, 2013.

[50] Telford, W. M. and Sheriff, R. E., *Applied Geophysics*. Cambridge University press, 1990.

[51] Turconi, A., Palmer, P., and Roberts, M., "Autonomous guidance and control in the proximity of asteroids using a simple model of the gravitational potential", *2nd IAA Conference on Dynamics and Control of Space Systems*, 2014.

[52] Turner, R. J., "A model of Phobos", *Icarus*, vol. 33, no. 1, pp. 116–140, 1978.

[53] Vokrouhlicky, D., Breiter, S., Nesvorny, D., and Bottke, W., "Generalized YORP evolution: Onset of tumbling and new asymptotic states", *Icarus*, vol. 191, no. 2, pp. 636–650, 2007.

[54] Werner, R. A., "The gravitational potential of a homogeneous polyhedron or don't cut corners", *Celestial Mechanics and Dynamical Astronomy*, vol. 59, no. 3, pp. 253–278, 1994.

[55] Werner, R. A. and Scheeres, D. J., "Exterior gravitation of a polyhedron derived and compared with harmonic and mascon gravitation representations of asteroid 4769 castalia", *Celestial Mechanics and Dynamical Astronomy*, vol. 65, no. 3, pp. 313–344, 1996.

[56] Wertz, J. R., *Spacecraft attitude determination and control*. Springer, Space Technology Library, 1978.

[57] Williams, D. R., *Asteroid fact sheet*, Dec. 2014. [Online]. Available: `http://nssdc.gsfc.nasa.gov/planetary/factsheet/asteroidfact.html`.

[58] Yu, Y. and Baoyin, H., "Orbital dynamics in the vicinity of asteroid 216 Kleopatra", *The Astronomical Journal*, vol. 143, no. 3, p. 62, 2012.